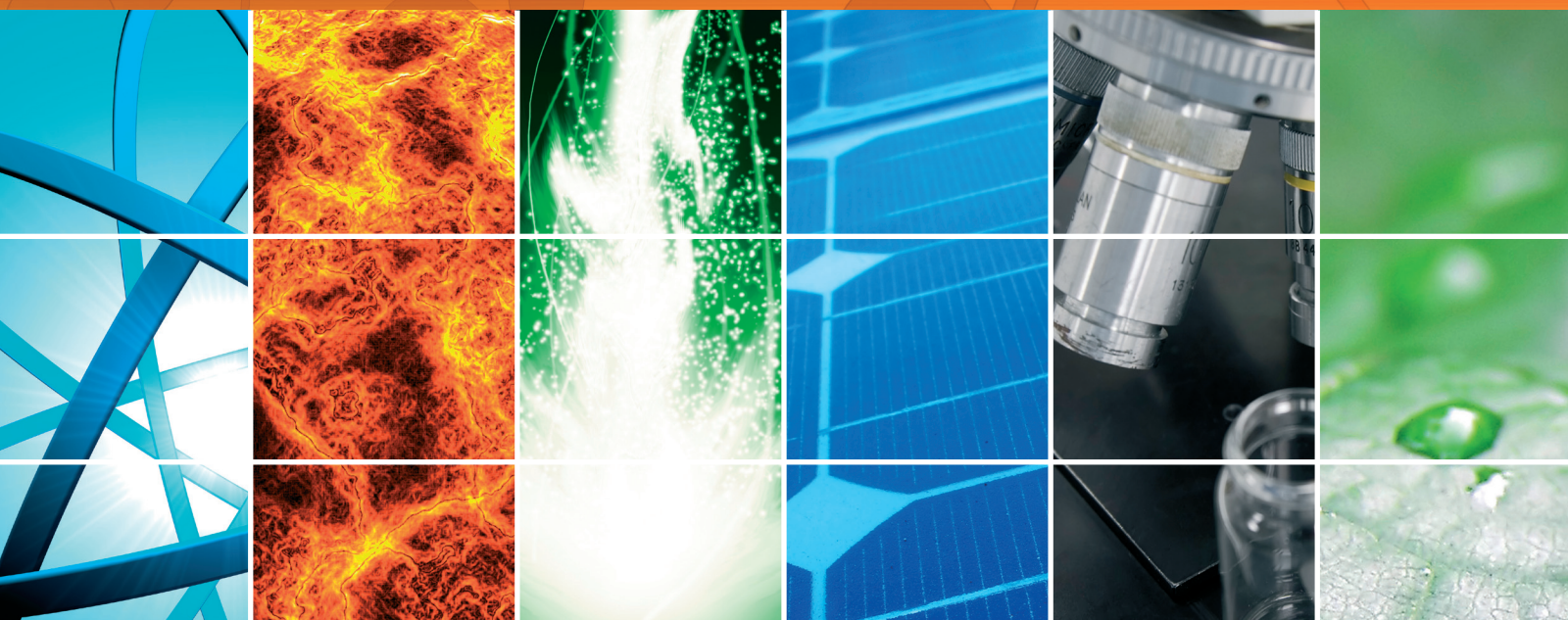


Multiscale Modeling of Photovoltaic Devices

Lead Guest Editor: Matthias Auf der Maur

Guest Editors: Urs Aeberhard, Christin David, and Alessio Gagliardi





Multiscale Modeling of Photovoltaic Devices

International Journal of Photoenergy

Multiscale Modeling of Photovoltaic Devices

Lead Guest Editor: Matthias Auf der Maur

Guest Editors: Urs Aeberhard, Christin David,
and Alessio Gagliardi



Copyright © 2018 Hindawi. All rights reserved.

This is a special issue published in "International Journal of Photoenergy." All articles are open access articles distributed under the Creative Commons Attribution License, which permits unrestricted use, distribution, and reproduction in any medium, provided the original work is properly cited.

Editorial Board

M. S.A. Abdel-Mottaleb, Egypt
Angelo Albini, Italy
Alberto Álvarez-Gallegos, Mexico
Vincenzo Augugliaro, Italy
Detlef W. Bahnemann, Germany
Simona Binetti, Italy
Fabio Bisegna, Italy
Thomas M. Brown, Italy
Joaquim Carneiro, Portugal
Yatendra S. Chaudhary, India
Věra Cimrová, Czech Republic
Juan M. Coronado, Spain
P. Davide Cozzoli, Italy
Dionysios D. Dionysiou, USA
Abderrazek Douhal, Spain
Mahmoud M. El-Nahass, Egypt
Polycarpos Falaras, Greece
Chris Ferekides, USA
Paolo Fornasiero, Italy
Manuel Fuentes Conde, Spain

Germà Garcia-Belmonte, Spain
Elisa Isabel Garcia-Lopez, Italy
M. Ashraf Gondal, Saudi Arabia
Giulia Grancini, Switzerland
Pierluigi Guerriero, Italy
Michael D. Heagy, USA
Wing-Kei Ho, Hong Kong
Jürgen Hüpkens, Germany
Tariq Iqbal, Canada
Adel A. Ismail, Kuwait
Chun-Sheng Jiang, USA
Cooper H. Langford, Canada
Manuel Ignacio Maldonado, Spain
Dionissios Mantzavinos, Greece
Santolo Meo, Italy
Claudio Minero, Italy
Antoni Morawski, Poland
Fabrice Morlet-Savary, France
Mohammad Muneer, India
Maria da Graça P. Neves, Portugal

Tsuyoshi Ochiai, Japan
Kei Ohkubo, Japan
Leonardo Palmisano, Italy
Thierry Pauporté, France
Philippe Poggi, France
Francesco Riganti-Fulginei, Italy
Leonardo Sandrolini, Italy
Jinn Kong Sheu, Taiwan
Zofia Stasicka, Poland
Elias Stathatos, Greece
Jegadesan Subbiah, Australia
K. R. Justin Thomas, India
Nikolai V. Tkachenko, Finland
Ahmad Umar, Saudi Arabia
Thomas Unold, Germany
Mark van Der Auweraer, Belgium
Wilfried G.J.H.M. Van Sark, Netherlands
Xuxu Wang, China
Yanfa Yan, USA
Jiangbo Yu, USA

Contents

Multiscale Modeling of Photovoltaic Devices

Matthias Auf der Maur , Urs Aeberhard, Christin David, and Alessio Gagliardi
Editorial (1 page), Article ID 3065252, Volume 2018 (2018)

Physics-Based Modeling and Experimental Study of Si-Doped InAs/GaAs Quantum Dot Solar Cells

A. P. Cédola, D. Kim, A. Tibaldi , M. Tang, A. Khalili, J. Wu, H. Liu, and F. Cappelluti 
Research Article (10 pages), Article ID 7215843, Volume 2018 (2018)

Effect of Annealing Process on $\text{CH}_3\text{NH}_3\text{PbI}_{3-x}\text{Cl}_x$ Film Morphology of Planar Heterojunction Perovskite Solar Cells with Optimal Compact TiO_2 Layer

Dan Chen, Xiaoping Zou, Hong Yang, Ningning Zhang, Wenbin Jin, Xiao Bai, and Ying Yang
Research Article (9 pages), Article ID 7190801, Volume 2017 (2018)

Accurate Maximum Power Point Tracking Algorithm Based on a Photovoltaic Device Model

Lhoussain El Bahir and Touria Hassboun
Research Article (10 pages), Article ID 5693941, Volume 2017 (2018)

Tandem Solar Cells Based on Cu_2O and c-Si Subcells in Parallel Configuration: Numerical Simulation

Mihai Răzvan Mitroi, Valerică Ninulescu, and Laurențiu Fara
Research Article (6 pages), Article ID 7284367, Volume 2017 (2018)

Modeling and Modulation of NNPC Four-Level Inverter for Solar Photovoltaic Power Plant

Xiaoqiang Guo, Xuehui Wang, Ran He, and Mehdi Narimani
Research Article (8 pages), Article ID 2383872, Volume 2017 (2018)

Modulation above Pump Beam Energy in Photorefectance

D. Fuertes Marrón
Research Article (4 pages), Article ID 4894127, Volume 2017 (2018)

Editorial

Multiscale Modeling of Photovoltaic Devices

Matthias Auf der Maur ¹, **Urs Aeberhard**,² **Christin David**,³ and **Alessio Gagliardi**⁴

¹*Department Electronics Engineering, University of Rome Tor Vergata, 00133 Rome, Italy*

²*IEK-5 Photovoltaik, Forschungszentrum Juelich, 52425 Jülich, Germany*

³*Madrid Institute for Advanced Studies in Nanoscience (IMDEA Nanoscience), 28049 Madrid, Spain*

⁴*Technische Universität München, Karlstrasse 45, 80333 Munich, Germany*

Correspondence should be addressed to Matthias Auf der Maur; auf.der.maur@ing.uniroma2.it

Received 18 December 2017; Accepted 19 December 2017; Published 10 June 2018

Copyright © 2018 Matthias Auf der Maur et al. This is an open access article distributed under the Creative Commons Attribution License, which permits unrestricted use, distribution, and reproduction in any medium, provided the original work is properly cited.

Renewable energy sources are among the most important ingredients for the development of a human society with sustainable environmental footprint. Among these, photovoltaics (PV) plays a key role and is therefore a field of intense research. The key parameters of a solar cell technology includes not only the energy conversion efficiency but also the operating lifetime and the overall cost of the energy produced. The latter must also be compared with other energy sources. The optimization of all these different aspects involves research across the whole photovoltaics value chain, starting from material science up to system optimization. Development of new solar cell device concepts is as important as search for new materials with more suitable optoelectronic properties or improved approaches for PV module design and integration in power distribution systems. This requires a comprehensive view on PV technology across all scales, from the atomic to the macroscopic and industrial scale.

An important aspect of PV research and of development of new devices and systems, is theoretical modeling as an indispensable tool for both basic understanding and device optimization. This involves modeling also on all scales, from the microscopic properties of materials and nanostructures up to the behavior of PV modules.

During the last decade, multiscale approaches have seen increasing interest for application in numerical simulation of electronic devices. In particular, modeling and understanding of advanced photovoltaic devices are expected to benefit from multiscale modeling, which allows describing consistently both macroscopic device behavior and local microscopic processes governing light absorption, loss

mechanisms, carrier transport, and extraction. In fact, many advanced PV concepts rely on effects or contain structural features that are insufficiently described by standard numerical simulation approaches or semianalytic models, both regarding electronic and optical properties. The different length scales of the electronic and optical degrees of freedoms specifically lead to an intrinsic need for multiscale simulation, which is accentuated in many advanced photovoltaics concepts including nanostructured regions. Moreover, the active layers in solar cells generally require to have a certain thickness and a large overall device area, in order to absorb a sufficient amount of light.

This special issue is an attempt to collect articles on modeling of PV devices and systems on all scales. It includes two experimental articles, one shedding some light on photoreflectance measurements when probing above the pump beam energy and the other discussing morphology in hybrid lead halide perovskite solar cells. One article describes numerical modeling of Cu_2O on Si tandem cells based on a semiempirical approach. A further contribution shows a physics-based model of a quantum dot solar cell, including a comparison with experimental data. The remaining two papers deal with system relevant aspects, namely, power point tracking and electrical inverters for connecting PV modules or power plants with appliances.

*Matthias Auf der Maur
Urs Aeberhard
Christin David
Alessio Gagliardi*

Research Article

Physics-Based Modeling and Experimental Study of Si-Doped InAs/GaAs Quantum Dot Solar Cells

A. P. Cédola,¹ D. Kim,² A. Tibaldi ,³ M. Tang,² A. Khalili,¹ J. Wu,² H. Liu,²
and F. Cappelluti ¹

¹Department of Electronics and Telecommunications, Corso Duca degli Abruzzi 24, 10129 Torino, Italy

²Department of Electronic and Electrical Engineering, University College London, Torrington Place, London WC1E 7JE, UK

³Istituto di Elettronica e di Ingegneria dell'Informazione e delle Telecomunicazioni (IEIIT), Consiglio Nazionale delle Ricerche (CNR), Corso Duca degli Abruzzi 24, 10129 Torino, Italy

Correspondence should be addressed to F. Cappelluti; federica.cappelluti@polito.it

Received 9 June 2017; Accepted 23 November 2017; Published 18 February 2018

Academic Editor: Urs Aeberhard

Copyright © 2018 A. P. Cédola et al. This is an open access article distributed under the Creative Commons Attribution License, which permits unrestricted use, distribution, and reproduction in any medium, provided the original work is properly cited.

This paper presents an experimental and theoretical study on the impact of doping and recombination mechanisms on quantum dot solar cells based on the InAs/GaAs system. Numerical simulations are built on a hybrid approach that includes the quantum features of the charge transfer processes between the nanostructured material and the bulk host material in a classical transport model of the macroscopic continuum. This allows gaining a detailed understanding of the several physical mechanisms affecting the photovoltaic conversion efficiency and provides a quantitatively accurate picture of real devices at a reasonable computational cost. Experimental results demonstrate that QD doping provides a remarkable increase of the solar cell open-circuit voltage, which is explained by the numerical simulations as the result of reduced recombination loss through quantum dots and defects.

1. Introduction

Quantum dots (QDs) are being widely investigated since several years as a promising material for advanced concepts such as multiple junction [1], intermediate band [2, 3], and hot carrier [4] solar cells. The basic building block of such devices is typically made by an almost standard diode structure embedding a region with QDs. Electronic effects and charge transfer mechanisms in the QDs and between the QD localized states and the continuum states of the host semiconductor present quantum mechanical features, while a large part of the device is made by bulk regions working in the semiclassical transport regime. Thus, device level simulation models of QD solar cells inherently require multiscale approaches which shall be able to combine the micro- and macroscale description at an affordable computational cost [5].

In the hierarchy of multiscale models for the simulation of QD solar cells (QDSCs), one of the simplest approaches

is provided by spatially resolved rate equation-based models, which couple microscopic calculated quantities such as the QD electronic structure, optical properties, and scattering rates to macroscopic equations for transport in the extended states. Several of the QD model parameters can also be extracted from routinary experimental data, making such approach suitable for both design and interpretation purposes. Modelling approaches able to reproduce the behavior of realistic devices and analyze the interplay of the involved physical mechanisms allow gaining insight into experimental results and provide useful feedback to the technology development. In this respect, while detailed balance theory of QDSCs has received a lot of attention and is useful to indicate the long-term target efficiency [6–8], less effort has been devoted to models based on semiconductor transport equations [9–13] and to the implications of QD carrier dynamics on the photovoltaic performances [14]. On the other hand, previous work by some of the present authors has shown

that introducing a proper description of interband and intersubband QD dynamics is a crucial asset to address some of the most critical issues encountered in QDSCs, such as poor carrier collection efficiency and degradation of the open-circuit voltage [15, 16].

In this work, we apply the QD-aware physics-based model firstly proposed in [15] to the study of InAs/GaAs QDSC exploiting selective Si doping. QD doping is extensively investigated as an attractive means to control photocarrier dynamics and improve QDSC performance (see, e.g., the recent review in [17] and the references therein). The present work extends the analysis already proposed in [18] on the interplay between doping and recombination processes in QDSCs and provides an experimental-based validation to the conclusions in [18]. To ensure an accurate description of the cell behavior, the model in [15, 18] has been complemented by an accurate electromagnetic model for carrier photogeneration. In the following, we present the basic ideas of the model, highlighting its thermodynamic consistency and discussing the identification of microscopic parameters from quantum models and experimental characterization, and we show with a real case study the valuable insight into device behavior that can be gained with this simulation approach.

2. Model

QD-based solar cells usually exploit a $p-n$ or $p-i-n$ structure with a region including a periodic stack of QD layers. Figure 1 schematically shows the energy band diagram of an In(Ga)As QD surrounded by GaAs barriers and the carrier transfer processes that are included in the model, as discussed in the following. From the electronic standpoint, the 3D confinement gives rise to a deeply confined energy level, the ground state (GS), one or more excited states (ES), both of them with 0D density of states, and a quasi-two-dimensional (2D) energy state associated with the wetting layer (WL) [19]. At device level, the WL subband is described as a 0D level with high degeneracy factor, accounting for the 2D density of states of the WL and the weakly confined excited states.

We assume negligible coupling between the QD layers; thus, the exchange of carriers between localized states in different layers is always mediated by the barrier extended states. Under such hypothesis, the QDSC operation is as follows: electrons and holes are photogenerated in the barrier and QD states by above- and below-gap photons, respectively. Charge transfer between continuum and bound states is characterized by capture and escape processes through the WL level. In the barrier, carriers move by drift-diffusion, and when they arrive within the interaction range of the QD region (a few nanometers), they can be either emitted through the QD layer or captured in the QD states. Dually, confined carriers may escape from the QD states through thermal emission to the WL and from the WL to the barrier. Only thermal escape is considered in this work, because in the QDs under study, at room temperature, photon-assisted escape is negligible [20]; moreover, due to the shallow confinement, thermal emission is so efficient that the inclusion of an electric field-assisted mechanism does not provide

any significant change to the overall picture. In [15], a good correlation between simulated and measured open-circuit voltage of cells with QD ground state emission between 1000 nm and 1300 nm has been demonstrated. On the other hand, deeper QDs may be significantly affected by field-assisted tunneling. Thus, the model formulation described in the following shall be applied only to the study of relatively shallow QDs at room temperature, hereinafter referred as thermally limited operation.

The electrical problem is formulated in terms of electrostatics and free carrier continuity equations, accounting for charge localization due to the QDs and charge transfer mechanisms between barrier and bound states. At the QD layer, Poisson's equation and electron continuity equation (for the sake of brevity, we omit hole equations) read as

$$\begin{aligned} \frac{\partial}{\partial x} \left(\epsilon \frac{\partial \phi}{\partial x} \right) &= -q \left[p - n + \sum_{\gamma} (p_{\gamma} - n_{\gamma}) + N_D^+ - N_A^- \right], \\ \frac{\partial n}{\partial t} &= \frac{1}{q} \frac{\partial J_n}{\partial x} - U_B + G_B - U_{n,CAP}, \end{aligned} \quad (1)$$

where ϕ is the electrostatic potential, n and p are the electron and hole densities, respectively, in the barrier, n_{γ} and p_{γ} are the electron and hole densities, respectively, in the QD state γ , and N_D^+ and N_A^- are the ionized donor and acceptor density, respectively. In the continuity equation, J_n is the electron drift-diffusion current density, U_B the net recombination rate, G_B the band-to-band photogeneration rate, and $U_{n,CAP}$ the WL-mediated net capture rate from the barrier into the QD states, that is, the difference between the capture rate from barrier to WL and the escape rate from WL to barrier. U_B includes both radiative and nonradiative processes. Radiative recombination is modeled as

$$U_{B,r} = B_{op} (pn - n_i^2), \quad (2)$$

B_{op} being the GaAs spontaneous emission coefficient and n_i the thermal equilibrium carrier density. Nonradiative recombination follows the Shockley-Read-Hall theory

$$U_{B,nr} = \frac{pn - n_i^2}{\tau_p(n + n_1) + \tau_n(p + p_1)}, \quad (3)$$

where $\tau_{n(p)}$ is the SRH recombination lifetime and n_1 and p_1 are the electron and hole densities, respectively, when Fermi level corresponds to the trap energy level, here assumed at midgap.

Capture and cascaded relaxation processes are described by a set of rate equations establishing a detailed balance, for each QD level, among all the interband and intersubband charge transfer mechanisms. At each QD layer, the rate equation describing the electron population in the subband γ reads as

$$\frac{\partial n_{\gamma}}{\partial t} = U_{n,CAP}^{\gamma+1 \rightarrow \gamma} - U_{n,CAP}^{\gamma \rightarrow \gamma-1} - U_{\gamma} + G_{\gamma}, \quad (4)$$

where $U_{\gamma} \approx f_{n,\gamma} f_{p,\gamma} / \tau_{r,\gamma}$ and G_{γ} are the net interband radiative recombination and photogeneration rates of the γ subband

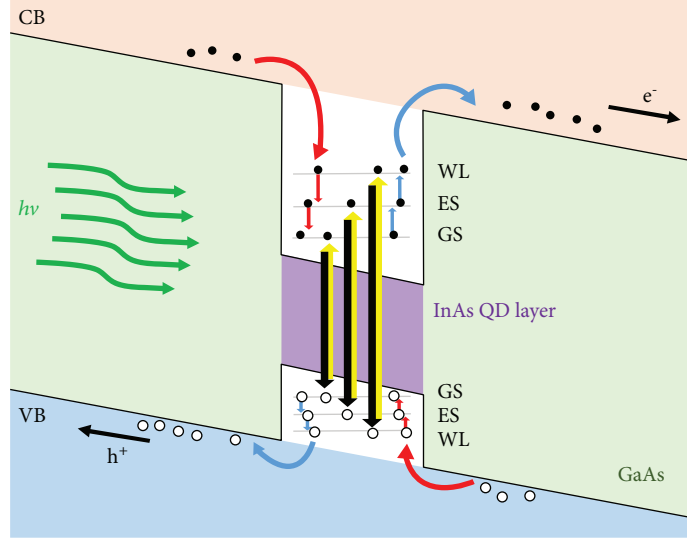


FIGURE 1: Energy band diagram of one InAs QD layer embedded in GaAs including all the carrier processes considered in the model: capture/relaxation (red), escape (blue), photogeneration (yellow), and recombination (black). WL is treated as a 0D state.

state ($\gamma = \text{WL, ES, GS}$), respectively. For the sake of simplicity, we consider only the radiative transitions associated to electron and hole states in the same subband. A radiative lifetime of 1 ns is assumed for all the QD states. The term $U_{n,\text{CAP}}^{\gamma \rightarrow l}$ is the net capture rate from the intersubband state k to the l one. Note that capture and relaxation processes are allowed to exist only between adjacent energy levels; thus, for $\gamma = \text{WL}$, $\gamma + 1$ state indicates the barrier, whereas for $\gamma = \text{GS}$ the terms involving $\gamma - 1$ must be ignored. To make the formulation treatable, we assume in the following Maxwell-Boltzmann statistics for the continuum states and Fermi-Dirac statistics for the QD states. Moreover, we neglect QD inhomogeneous broadening; thus, the QD density of states is a Dirac delta function.

The capture or relaxation process of an electron from state γ to state $\gamma - 1$ can be formulated as

$$R_{\text{CAP}} = c' N_{\gamma} f_{\gamma} N_{\gamma-1} (1 - f_{\gamma-1}), \quad (5)$$

where c' is the scattering rate ($\text{cm}^3 \cdot \text{s}^{-1}$) of the transition and N_k is the effective density of states in the k band, with distribution function f_k . The reverse escape process reads as

$$\begin{aligned} R_{\text{ESC}} &= e' N_{\gamma-1} f_{\gamma-1} N_{\gamma} (1 - f_{\gamma}) \\ &= e' N_{\gamma-1} N_{\gamma} f_{\gamma} (1 - f_{\gamma-1}) e^{(E_{Fn}^{\gamma-1} - E_{Fn}^{\gamma})/k_B T} e^{(E_{\gamma} - E_{\gamma-1})/k_B T}, \end{aligned} \quad (6)$$

where the last term is derived taking advantage of the following identity, which holds regardless of the specific statistics, Boltzmann or Fermi [21],

$$f_{\gamma} (1 - f_{\gamma-1}) e^{(E_{Fn}^{\gamma-1} - E_{Fn}^{\gamma})/k_B T} = f_{\gamma-1} (1 - f_{\gamma}) e^{(E_{\gamma-1} - E_{\gamma})/k_B T}. \quad (7)$$

In (6), E_k and E_{Fn}^k are the energy of the k state and the quasi-Fermi level of the corresponding electron population,

respectively. For barrier electrons, obviously, E_k coincides with the minimum of the conduction band. The detailed balance at thermal equilibrium imposes

$$c' = e' e^{(E_{\gamma} - E_{\gamma-1})/k_B T}, \quad (8)$$

yielding the net capture rate $U_{n,\text{CAP}} = R_{\text{CAP}} - R_{\text{ESC}}$

$$U_{n,\text{CAP}}^{\gamma \rightarrow \gamma-1} = \frac{1}{\tau_{\text{cap}}^{\gamma}} n_{\gamma} \left(1 - \frac{n_{\gamma-1}}{N_{\gamma-1}} \right) \left(1 - e^{(E_{Fn}^{\gamma-1} - E_{Fn}^{\gamma})/k_B T} \right), \quad (9)$$

$n_k = N_k f_k$ being the free electron density in the k state and $\tau_{\text{cap}}^{\gamma} = 1/c' N_{\gamma-1}$. Equation 9 highlights the correlation between the onsets of capture ($U_{n,\text{CAP}} > 0$) or escape ($U_{n,\text{CAP}} < 0$) and the nonequilibrium condition between electron populations in the states E_{γ} and $E_{\gamma-1}$.

The above formulation can be generalized so as to include the detailed energy dependence of the density of states of the different subbands (e.g., to include a more physical description of the QD states and WL states), Fermi-Dirac statistics in the continuum bands, as well as the energy dependence of the microscopic scattering matrix element $M^{\gamma, \gamma-1}$ describing the interaction between the two states [21]:

$$\begin{aligned} R_{\text{CAP}} &= \int_{E_{\gamma}} dE'_{\gamma} \int_{E_{\gamma-1}} g_{\gamma}(E'_{\gamma}) f_{\gamma}(E'_{\gamma}) M^{\gamma, \gamma-1} g_{\gamma-1}(E'_{\gamma-1}) \\ &\quad \cdot (1 - f_{\gamma-1}(E'_{\gamma-1})) dE'_{\gamma-1}, \\ R_{\text{ESC}} &= \int_{E_{\gamma}} dE'_{\gamma} \int_{E_{\gamma-1}} g_{\gamma}(E'_{\gamma}) (1 - f_{\gamma}(E'_{\gamma})) M^{\gamma-1, \gamma} g_{\gamma-1} \\ &\quad \cdot (E'_{\gamma-1}) f_{\gamma-1}(E'_{\gamma-1}) dE'_{\gamma-1}. \end{aligned} \quad (10)$$

Introducing the energy averaged scattering element $\langle M^{\gamma, \gamma-1} \rangle$, averaged over the entire ensemble of possible

initial and final states, and after some analytical manipulation, one derives an expression of $U_{n,CAP}$ completely analogous to 8, with $\tau_{cap}^{-1} = 1/\langle M^{\nu,\nu-1} \rangle N_{\nu-1}$, $n_{\nu} = \int_E g_{\nu} f_{\nu} dE$, $N_{\nu-1} = \int_E g_{\nu-1} dE$.

Capture and relaxation in self-assembled In(Ga)As/GaAs QDs happen through complicated dynamics involving emission of longitudinal optical (LO) phonon emission, polaron (electron-phonon coupling) decay, defect-mediated relaxation, carrier-carrier scattering, and so forth (see, e.g., [22–24] and the references therein). The scattering time τ_{cap} derived from quantum models is typically a function of the carrier density in the WL and QD states, which in turn depends on injection/photogeneration of carriers according to the cell operating conditions and on design parameters such as doping. At low carrier density, electron-LO-phonon interaction and Auger electron-hole scattering act as very efficient relaxation channels, providing relaxation times on the scale of tenths of ps to tens of ps [22, 23, 25]. At high carrier density, carrier-carrier scattering may become significant, yielding again relaxation times on the ps scale [24]. In particular, for n -doped (p -doped) QD hole (electron), the population is extremely low; thus, electron-hole scattering is negligible and relaxation occurs through a combination of electron-electron (hole-hole) scattering and carrier-LO-phonon relaxation. These predictions are confirmed by several experimental data on undoped and doped samples: in [26], relaxation times from WL to QD ground state were found to be 2, 3, and 6 ps for p -doped, n -doped, and undoped samples, respectively. Further experimental data of similar sign are summarized in [23]. Overall, theoretical and experimental results on In(Ga)As/GaAs QDs show that net capture/relaxation rates—on a ps scale—are extremely fast with respect to the characteristic QD band-to-band and intraband radiative lifetimes (about 1 ns and 100 ns, resp. [25]), making the QD carrier lifetime largely dominated by the QD radiative lifetime. Moreover, the open-circuit voltage (V_{oc}) penalty in thermally limited QDSCs is dominated by the ratio between carrier lifetime in the barrier and carrier lifetime in QDs [27], the last one being the net result of the competing processes of capture/relaxation/recombination through the QDs—from the one hand—and escape from the QD bound states and electric-field-driven sweep out through the extended states—from the other hand. Thus, at least in In(Ga)As/GaAs QDs and under nonconcentration operation, capture/relaxation times can be reasonably treated as constant parameters, neglecting their carrier density dependence and the possible electric-field dependence due to tunneling mechanisms. In this respect, it may be remarked that the electrical field across the interdot layers plays however an important role in the resulting net capture rate in QDs: at high field, free-carrier transit time is high and the probability of capture from the barrier into the QDs remains low (such situation is representative of the short-circuit condition, where QD recombination turns to be negligible). In [28], carrier capture from the GaAs barrier was found to be fully quenched in fields of only 15 kV/cm. When the electrical field is significantly screened (e.g., as forward bias approaches the maximum power point and open-circuit voltage), the transit time decreases and the net capture rate in the

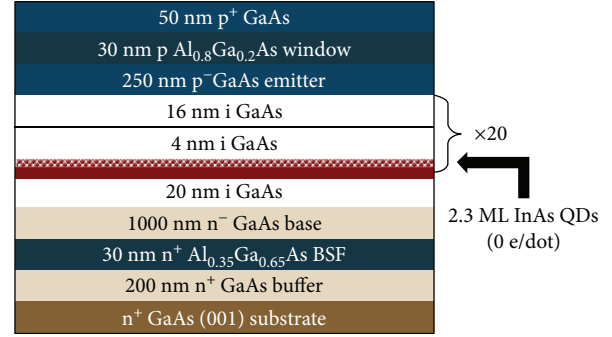


FIGURE 2: Sketch of the epilayer structure of the $20 \times$ QD solar cell (R3 and R4 samples).

QDs increases; that is, QDs turn into radiative trap centers (see [15, 16] for a detailed discussion).

In the following simulations, we use empirical data extracted in [15] from the interband-pump-intraband-probe spectroscopy experiments reported in [29]. To this aim, we assume very fast capture into the WL, which occurs through one-LO-phonon interaction on a 0.1 ps time scale, followed by cascaded relaxation of carriers into the ES and GS states. Fitting the time-resolved IR absorption of QDs similar to those in the present work, we estimated electron time constants of about 1 ps [15] for WL-ES and ES-GS relaxation. Due to their large effective mass, holes form closely spaced energy levels, characterized by fast phonon-mediated capture and relaxation mechanisms, whose time constants are set to 100 fs.

Concerning the photogeneration rates, the simulation calculates the (optical) electric field profile across the multilayer structure, with each material characterized by the complex refractive index $\hat{n} = n + i\kappa = n + i\alpha\lambda/(4\pi)$ (α being the absorption coefficient), exploiting a scattering matrix formalism for coherent multilayers [30]. From the optical electric field profile $E_{op}(x)$, the absorbed photon density (at each wavelength) and the photogeneration rate (assuming unitary quantum yield) are then calculated through the divergence of the Poynting vector, yielding

$$G = \frac{\sigma}{2h\nu} |E_{op}|^2, \quad (11)$$

where $h\nu$ is the photon energy and $\sigma = n\alpha/\mu_0 c$ the electrical conductivity (μ_0 and c being the vacuum magnetic permeability and light velocity, resp.).

The model numerical implementation is based on the discretization of the electrical equations through the Scharfetter-Gummel scheme and the self-consistent solution of the resulting system of nonlinear equations through Newton-based methods [31].

3. Experimental

All the epitaxial structures were grown using a solid-source molecular beam epitaxy (MBE) on n^+ GaAs (100) substrates. InAs/GaAs QDSC structures based on those previously demonstrated by Kim et al. [32] were used, as shown in Figure 2. The structures consist of a 200 nm GaAs buffer layer with Si

doping density of $1 \times 10^{18} \text{ cm}^{-3}$, 30 nm $\text{Al}_{0.35}\text{Ga}_{0.65}\text{As}$ back surface field (BSF) with Si doping density of $1 \times 10^{18} \text{ cm}^{-3}$, 1000 nm GaAs base with Si doping density of $1 \times 10^{17} \text{ cm}^{-3}$, 250 nm GaAs emitter with Be doping density of $2 \times 10^{18} \text{ cm}^{-3}$, 100 nm GaAs emitter with Be doping density of $5 \times 10^{18} \text{ cm}^{-3}$, 30 nm $\text{Al}_{0.75}\text{Ga}_{0.25}\text{As}$ window layer with Be doping density of $2 \times 10^{18} \text{ cm}^{-3}$, and 50 nm GaAs contact layer with Be doping density of $1 \times 10^{19} \text{ cm}^{-3}$. 20 layers of InAs QDs were grown in the intrinsic region of the SCs. The QDs were grown by the Stranski-Krastanov mode with the InAs coverage of 2.1 monolayers (ML) at a substrate temperature of $\sim 500^\circ\text{C}$. A high growth temperature was used during the growth of the GaAs spacer layers to suppress the formation of dislocations [33–35]. No cap layer was applied between the InAs QDs and the GaAs space layers. Direct Si doping with doping densities of 14 e/dot was applied to the QDs in the Si-doped QDSCs [32]. Whereas the InAs QD layers in all other samples were separated by 20 nm GaAs spacer, the spacer layers in the QDSC with additional spacer layers (R5) were 25 nm each, which gave additional 100 nm in total. For the post-growth sample cleaning, the SCs were ultrasonicated in acetone and isopropanol for 10 min each at room temperature. To remove the oxide on the surface of the samples, the SCs were immersed in diluted ammonia solution (1:19) for 30 s. A Au-Zn alloy (95% Au, 5% Zn) was deposited in grid patterns to form 200 nm thick *p*-type electrodes using a metal shadow mask and a thermal evaporator.

The morphology of the QD layers was studied using a Veeco Nanoscope V atomic force microscope (AFM). 532 nm excitation from a diode-pumped solid-state laser was used for photoluminescence (PL) measurements. The sample temperature during the PL measurements was controlled using a He-cooled cryostat. Current density versus voltage ($J-V$) measurements was performed using an LOT-calibrated solar simulator with a xenon lamp under one-sun air mass (AM) 1.5 G illumination at 25°C . The devices were connected to a Keithly 2400 sourcemeter via a 4-point probe station, and ReRa Tracer 3 software was used to collect the data. Photocurrent measurements were obtained using a Halogen lamp chopped to 188 Hz through a Newport monochromator. A 4-point probe connected with a lock-in amplifier was used to collect data. The monochromatic beam was then calibrated using a Si photodiode, and the data was analysed with Photor QE 3.1 software to produce the external quantum efficiency (EQE).

4. Results and Discussion

An overview of the photovoltaic characteristics of the undoped and Si-doped QD solar cells and of an undoped reference cell (same geometry and doping but without the inclusion of QDs) is presented in Figure 3 and Table 1. The target performances for the REF cell were $V_{oc} = 1.04 \text{ V}$, short circuit current density (J_{sc}) of 14.2 mA/cm^2 , and fill factor (FF) of 86.5%. All the cells, included in the REF one, show quite low FF and unusual rounded shape of the $J-V$ characteristic, whose origin is attributed to issues in the realization of the metal grid. The observed behavior cannot be fitted by a

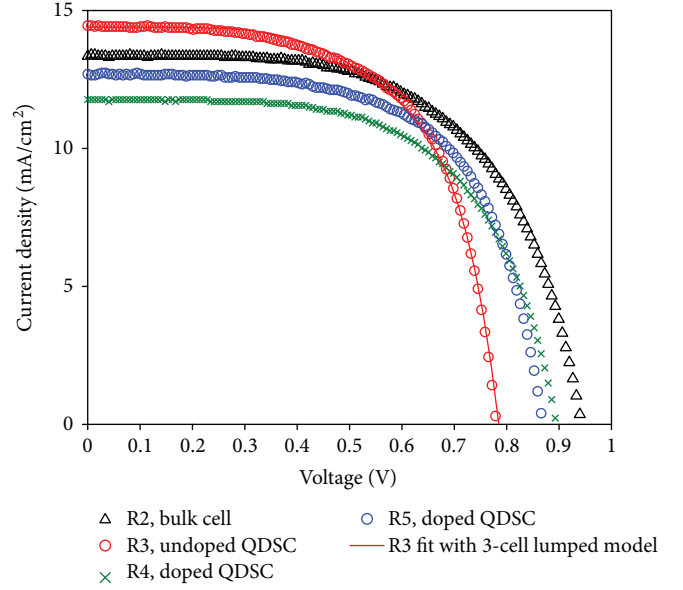


FIGURE 3: Current density versus voltage characteristics measured under one-sun illumination (AM 1.5 G) for the reference GaAs bulk cell (R2), undoped QDSC (R3), and two-doped (14 e/dot) QDSC with interdot spacing of about 20 nm (R4) and 25 nm (R5).

TABLE 1: Photovoltaic parameters extracted from the measured $J-V$ characteristics in Figure 3.

Device	J_{sc} , mA/cm^2	V_{oc} , V	FF, %
R2, REF GaAs cell	13.37	0.942	59.7
R3, undoped QD	14.42	0.778	62.7
R4, doped QD	11.74	0.894	61.1
R5, doped QD	12.70	0.868	63.1

simple lumped model with series and shunt resistances: a nonuniform three-section model of the cell [36] provides a good fitting of the measured characteristics, as shown in Figure 3, with extracted series resistances of about 50, 1, and $1 \Omega\text{cm}^2$ for each subcell. The undoped QDSC shows a marked penalty of V_{oc} with respect to the REF cell, which is partially recovered in the samples with directly doped QDs. On the other side, the doped QDSCs have lower J_{sc} that can be in part attributed to the shrinking of the space charge region and subsequent reduction of carrier collection and in part to lower minority carrier lifetime in the base and emitter regions as demonstrated later (see Figure 4) based on measured EQE and simulations. It may be worth noticing that under the assumption of similar material quality, the slightly larger thickness of the undoped region of the R5 sample (520 nm) with respect to the R4 one (420 nm) would produce an absolutely marginal difference in terms of device level behavior. Finally, the higher J_{sc} of the undoped QDSC with respect to the REF cell is not related to QD photogeneration but rather to a worse carrier collection efficiency in the emitter causing a decreased EQE in the GaAs absorption range.

The electronic structure of QDs is estimated based on room temperature steady-state PL. The measured PL spectra at low and room temperature are shown in Figures 5(a) and

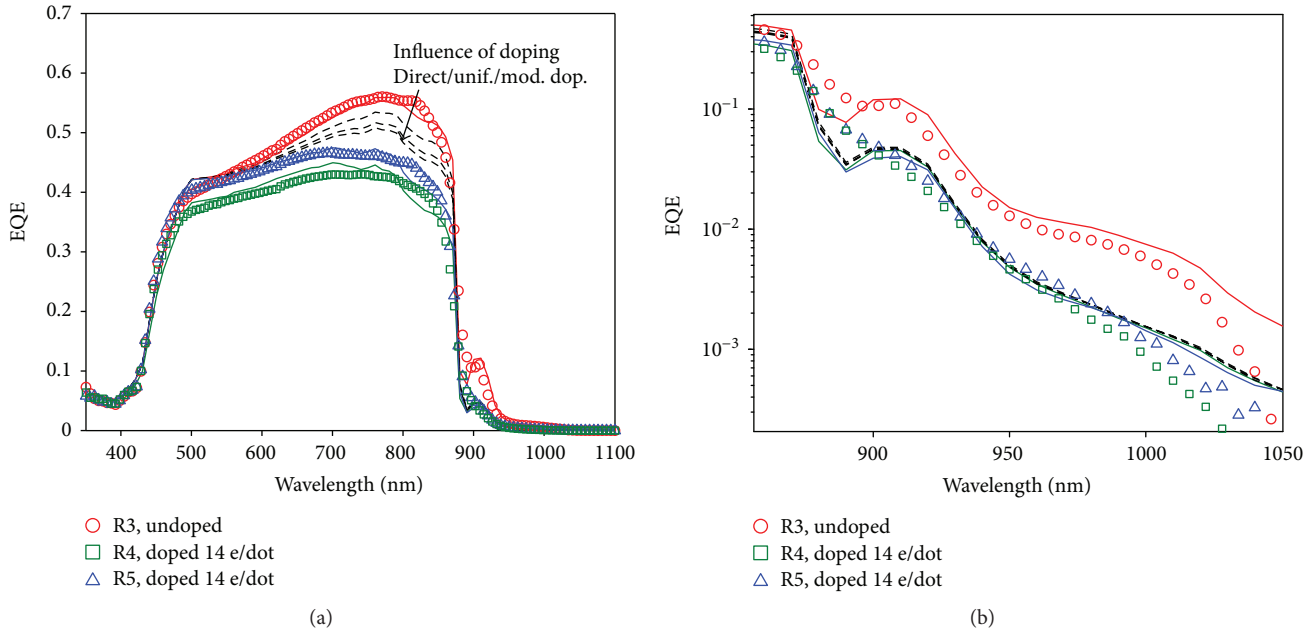


FIGURE 4: (a) Comparison between measured and simulated EQE. (b) Zoom in the QD wavelength region. The black dashed lines show the predicted decrease of EQE according in the doped (14 e/dot) QD solar cell assuming the same minority carrier lifetime as in the undoped sample and under different hypotheses of dopant impurity distribution: well confined in the QD region (direct), uniformly distributed across the QD stack, and located at the center of the GaAs interdot layers. Symbols show experimental data. Solid lines indicate simulation and best fit.

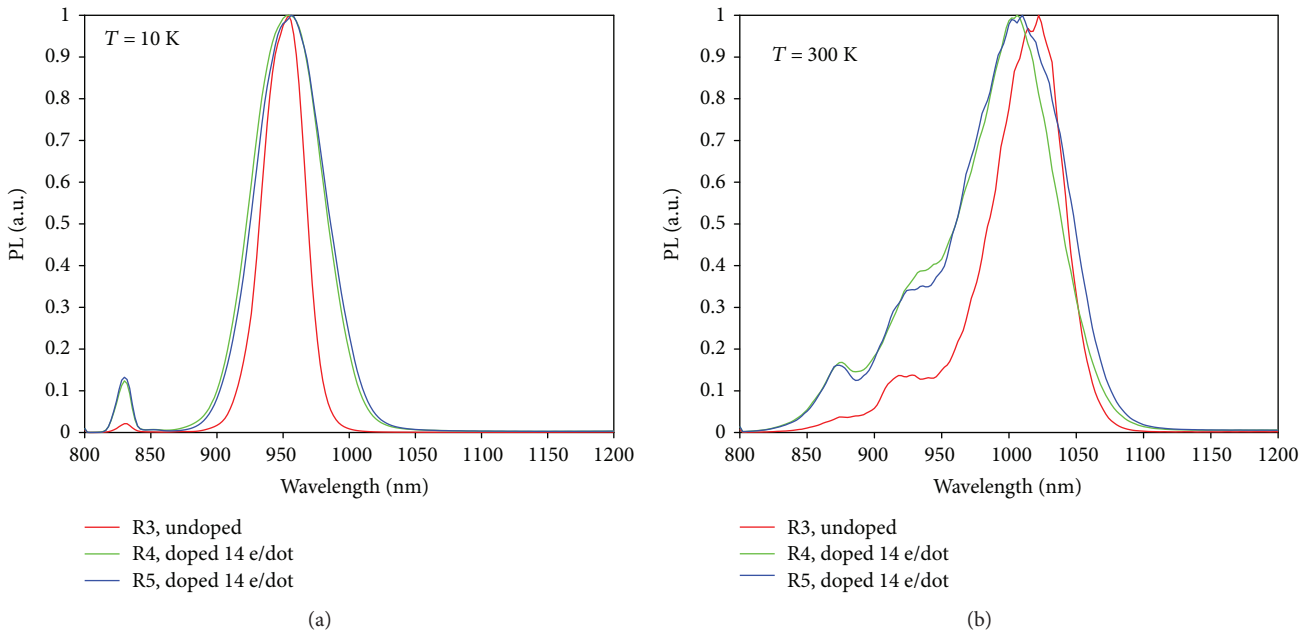


FIGURE 5: Normalized PL spectra measured at $T = 10$ K (a) and $T = 300$ K (b).

5(b), respectively. At low temperature, only the GS state is visible, with a slight redshift of the PL peak and an increase of the full width at half maximum (FWHM) for the doped samples with respect to the undoped one especially in the longer wavelength region. The observed behavior suggests that in the doped samples the distribution of the dot size is less homogeneous, with an increased density of larger (i.e.,

more confined) QDs which emit at lower energies [37]. At 300 K, the slight blue shift of the GS emission of the doped samples may be indicative of a higher interband transition energy and of a weaker quantum confinement of electrons in the GS. More importantly, the PL spectrum makes well visible the increase of the WL emission with respect to the GS one with doping. This indicates less efficient ES and GS

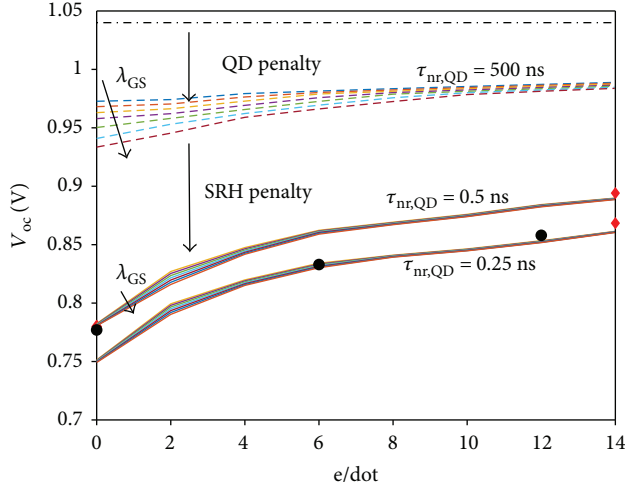


FIGURE 6: Analysis of V_{oc} penalty in QDSC as a function of the per dot doping density, for different GS energy confinement (λ_{GS} ranges from 990 nm to 1050 nm) and different minority carrier lifetime in the interdot layers ($\tau_{nr,QD}$). The black dash-dot line indicates the V_{oc} of the reference bulk GaAs cell. The red bullet indicates experimental data in this work. The black bullet indicates experimental data from Lam et al. [43].

relaxation pathways for the WL state of doped QDSCs that can be understood as a consequence of blocking of electron relaxation in the ES and GS due to state filling effects [18]. From the PL measurements, we identified energy gaps of 1.24 eV, 1.28 eV, and 1.37 eV for GS, ES, and WL, respectively, as representative values for all the samples under study. The impact of slight variations in the QD electronic structure and GS energy is analyzed in detail later (see Figure 6), based on the analysis of V_{oc} data. Based on literature data [38], the confinement energy for electron and holes in each state is set to 80% and 20% of the difference between barrier and QD level energy gap [38] (e.g., $\Delta E_{GS}^e = 0.8(E_g - E_{g,GS})$, E_g and $E_{g,GS}$ being the barrier energy gap and GS energy gap, resp.).

The analysis of the experimental results through the device level model in Section 2 provides also an estimation of the Shockley-Read-Hall lifetimes in (3) characterizing nonradiative recombination across the barrier states. Even though the strong interaction between continuum and localized states makes not obvious to single out the impact of such parameters on the cell photovoltaic behavior, some basic knowledge of device operation (as routinely observed in bulk cells) allows identifying a suitable strategy for their extraction. In fact, it is worth reminding that short-circuit SRH recombination is more detrimental in the doped regions, whereas it marginally affects carrier collection efficiency in the undoped one. In contrast, at open-circuit condition, the most detrimental loss arises from SRH recombination in the undoped region. Thus, once a reasonably accurate optical model of the cell is established, the analysis of EQE spectra—in particular in the GaAs wavelength range—allows identifying lower bounds for the SRH lifetimes in the base and emitter, whereas the analysis of the open-circuit voltage provides an estimation of SRH lifetimes in the undoped region.

The measured EQE spectra are shown in Figure 4. Fitting the EQE of the undoped cell in the GaAs wavelength region, we estimated a lower bound for the SRH lifetimes in the p -doped emitter and n -doped base of about 8 ns and 10 ns, respectively. For reference, the expected lifetimes, accounting for doping dependence, are about 20 ns and 300 ns, respectively [39]. Based on the model identified for the undoped cell, we have verified the impact of QD doping on J_{sc} . Since the actual distribution of dopant impurities is not known, we compare in Figure 4 different hypotheses of dopant distribution: dopant atoms at the QD site (direct doping), a thin layer of dopant atoms located in the middle of the interdot layer (mod. dop), and a uniform distribution across the whole QD stack. A detailed analysis of the impact of the different doping profiles on the energy band diagram and potential distribution may be found in [18]. Simulations in Figure 4 show that doping induces a clear penalty in the GaAs-range EQE, but such penalty is not sufficient to explain the reduced EQE of the direct doped samples with respect to the undoped ones. The EQE degradation is in fact reproduced by accounting for a reduction of minority carrier lifetime in the doped regions, with fitted SRH lifetimes of 500 ps in the emitter of the R5 sample and 50 ps (emitter)/200 ps (base) for the R4 sample.

Finally, the optical properties of the QD layer are estimated from the analysis of the subband gap EQE of the undoped cell reported in Figure 4(b). To this aim, the InAs/GaAs QD layer is described as a homogeneous equivalent medium with optical absorption $\alpha_{GaAs} + \Delta\alpha$ and real refractive index $n_{GaAs} + \Delta n$, where $\Delta\alpha$ and Δn are the absorption coefficient and refractive index of the QD material, weighted by the QD areal density. For the GS and ES states, a Gaussian distribution is used, with a peak absorption of 500 cm^{-1} and 1000 cm^{-1} and FWHM of 50 nm, respectively. The WL absorption profile is modeled by convolution of a Heaviside step function with a Lorentzian broadening function, with an absorption peak of about $2 \times 10^4 \text{ cm}^{-1}$ and FWHM of 40 nm. Representative examples of the spectral behavior of the extracted $\Delta\alpha$ and Δn can be found in [40]. The complex refractive index of bulk materials was taken from [41].

Figure 4(b) also highlights the suppression of QD photo-generation in the doped samples, with good agreement between measurements and simulations.

At open-circuit condition, based on the QD electronic model, we first analyze the predicted V_{oc} penalty of the QDSCs with respect to the bulk cell. To this aim, we take into account possible fluctuations of the QD confinement as seen from the PL spectra. Figure 6 reports the V_{oc} of the QD solar cell as a function of doping for different QD families with GS transition energy between 1.18 and 1.25 eV. SRH lifetimes in the doped regions are those extracted from the short-circuit analysis; in the undoped region, a SRH lifetime of 500 ns is assumed. For the sake of comparison, the V_{oc} (design value) of the REF cell is also reported. The analysis shows that the *inherent* (i.e., for negligible defectivity of the QD material) penalty due to the inclusion of the QDs is about 120 mV for the largest GS confinement, in agreement with previous theoretical works [20] and experimental data of QDSC with record V_{oc} [42]. Such penalty can be fully attributed

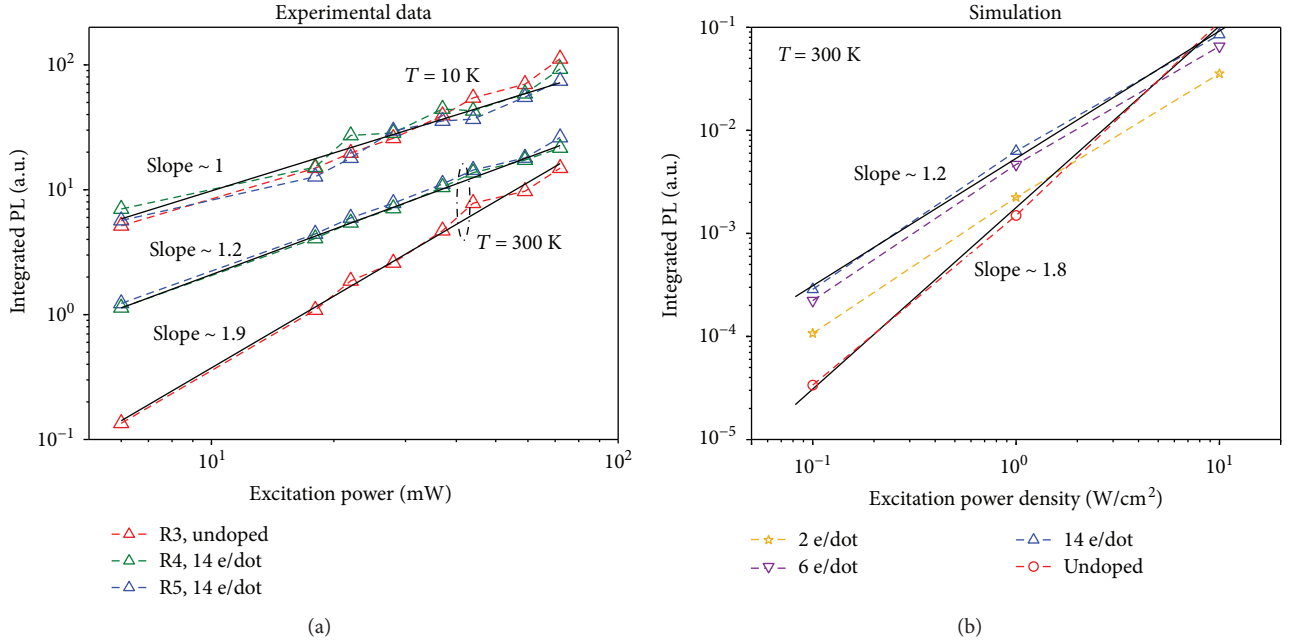


FIGURE 7: (a) Measured IPL intensity versus excitation power. (b) Simulated IPL intensity versus excitation power density. In the experiments, the equivalent excitation power density was about $1 W/cm^2$ at power of $16 mW/cm^2$.

to radiative recombination through the QD states [15, 18]. On the other hand, the comparison with the experimental data suggests that some other loss mechanism is in play in the devices under study, causing an added penalty of about 180 mV for the undoped case. Besides the measured data of the samples described in Section 3, we included also experimental data of very similar QDSCs, reported by the same research group in [43]. A very good agreement between simulated and measured data is obtained by assuming a significant defectivity of the interdot spacer layers, causing SRH lifetime (labeled as $\tau_{nr,QD}$ in Figure 6) on the order of fractions of ns, that is, lower than the QD radiative lifetime. The calculated trend of V_{oc} as a function of the doping density closely follows the measured one, suggesting that dopant atoms are well incorporated in the QDs and provide electrons per dot in line with the nominal doping value. Overall, the results highlight that doping is always beneficial in terms of V_{oc} , since it mitigates both QD radiative recombination and nonradiative recombination. QD radiative recombination is in fact suppressed by QD state filling; SRH recombination is suppressed because doping shifts the electron quasi-Fermi level far away from the intrinsic Fermi level reducing the capture/emission probability of electrons and holes by the midgap defect. Further analysis of doped-induced SRH suppression and examples of calculated SRH recombination rates in QDSCs may be found in [18, 44].

Finally, further supporting the interpretation that the QDSCs under study are limited by SRH recombination, Figure 7 compares the measured and simulated behavior of the integrated PL (IPL) versus the excitation power (P_{exc}): at $T = 10$ K, all the cells present a linear dependence of IPL with P_{exc} (slope ~ 1 in the log-log plot) regardless of doping, since they are dominated by the radiative recombination through the QDs. On the other hand, at $T = 300$ K, the

undoped cell shows a superlinear dependence of IPL with P_{exc} (slope ~ 1.8 in the log-log plot), while the doped ones have again almost linear behavior. Our comprehension of the mechanism is that at $T = 300$ K nonradiative recombination through the barrier is an effective loss mechanism for photogenerated carriers that tends to be suppressed (or saturated) as the excitation power increases: thus, at low excitation power, IPL scales almost quadratically with P_{exc} [18, 45, 46]. The introduction of doping changes the electrostatic potential and electrical field profiles of the cell in such a way that SRH recombination results minimized. As a result, the doped QD cells have again a radiative limited behavior and their IPL scales linearly with P_{exc} .

5. Conclusion

We have applied physics-based numerical simulations to investigate the photovoltaic behavior of quantum dot solar cells which demonstrate a large increase of the open-circuit voltage with doping. The analysis of the experimental results points out that doping has profound effects on the cell behavior, which are difficult to disentangle without the support of device level simulations, since they involve the microscale, in terms of QD carrier dynamics, and the macroscale, since doping affects the electric field distribution across the photoactive region. The analysis allows also assessing the margin of improvement for the open-circuit voltage, taking into account that the cells under study operate under thermally limited regime; that is, two-step photon absorption is negligible. The presented device level simulations are developed within a multiscale modeling framework which combines in a self-consistent fashion transport equations in the bulk, rate equations for carrier dynamics in the QD states, and an accurate electromagnetic model of the optical field

across the cell. Further physical mechanisms relevant to QD-based solar cells, such as two-photon absorption, Auger processes, and hot carrier relaxation can be incorporated in this simulation framework allowing us to gain a deeper understanding of the physics of real devices and directions for their development.

Conflicts of Interest

The authors declare that they have no conflicts of interest.

Acknowledgments

This project has received funding from the European Union's Horizon 2020 Research and Innovation Programme under Grant Agreement no. 687253. F. Cappelluti acknowledges useful meetings and discussions supported by COST Action MP1406 "MultiscaleSolar".

References

- [1] S. Hubbard and R. Raffaele, "Boosting solar-cell efficiency with quantum-dot-based nanotechnology," *SPIE Newsroom*, 2010.
- [2] A. Luque and A. Martí, "Increasing the efficiency of ideal solar cells by photon induced transitions at intermediate levels," *Physical Review Letters*, vol. 78, no. 26, pp. 5014–5017, 1997.
- [3] S. Asahi, H. Teranishi, K. Kusaki, T. Kaizu, and T. Kita, "Two-step photon up-conversion solar cells," *Nature Communications*, vol. 8, p. 14962, 2017.
- [4] D. M. Tex, I. Kamiya, and Y. Kanemitsu, "Control of hot-carrier relaxation for realizing ideal quantum-dot intermediate-band solar cells," *Scientific Reports*, vol. 4, p. 4125, 2014.
- [5] U. Aeberhard, "Simulation of nanostructure-based high-efficiency solar cells: challenges, existing approaches, and future directions," *IEEE Journal of Selected Topics in Quantum Electronics*, vol. 19, no. 5, pp. 1–11, 2013.
- [6] M. Y. Levy and C. Honsberg, "Solar cell with an intermediate band of finite width," *Physical Review B*, vol. 78, no. 16, article 165122, 2008.
- [7] L. Cuadra, A. Martí, and A. Luque, "Influence of the overlap between the absorption coefficients on the efficiency of the intermediate band solar cell," *IEEE Transactions on Electron Devices*, vol. 51, no. 6, pp. 1002–1007, 2004.
- [8] R. Strandberg and T. Reenaas, "Optimal filling of the intermediate band in idealized intermediate-band solar cells," *IEEE Transactions on Electron Devices*, vol. 58, no. 8, pp. 2559–2565, 2011.
- [9] V. Aroutiounian, S. Petrosyan, A. Khachatryan, and K. Touryan, "Quantum dot solar cells," *Journal of Applied Physics*, vol. 89, no. 4, pp. 2268–2271, 2001.
- [10] A. S. Lin and J. D. Phillips, "Drift-diffusion modeling for impurity photovoltaic devices," *IEEE Transactions on Electron Devices*, vol. 56, no. 12, pp. 3168–3174, 2009.
- [11] K. Yoshida, Y. Okada, and N. Sano, "Self-consistent simulation of intermediate band solar cells: effect of occupation rates on device characteristics," *Applied Physics Letters*, vol. 97, no. 13, p. 133503, 2010.
- [12] I. Tobias, A. Luque, and A. Martí, "Numerical modeling of intermediate band solar cells," *Semiconductor Science and Technology*, vol. 26, no. 1, article 014031, 2011.
- [13] R. Strandberg and T. Reenaas, "Drift-diffusion model for intermediate band solar cells including photofilling effects," *Progress in Photovoltaics*, vol. 19, no. 1, pp. 21–32, 2012.
- [14] V. Aroutiounian, S. Petrosyan, and A. Khachatryan, "Studies of the photocurrent in quantum dot solar cells by the application of a new theoretical model," *Solar Energy Materials and Solar Cells*, vol. 89, no. 2, pp. 165–173, 2005.
- [15] M. Gioannini, A. P. Cedola, N. Di Santo, F. Bertazzi, and F. Cappelluti, "Simulation of quantum dot solar cells including carrier intersubband dynamics and transport," *IEEE Journal of Photovoltaics*, vol. 3, no. 4, pp. 1271–1278, 2013.
- [16] M. Gioannini, A. P. Cedola, and F. Cappelluti, "Impact of carrier dynamics on the photovoltaic performance of quantum dot solar cells," *IET Optoelectronics*, vol. 9, no. 2, pp. 69–74, 2015.
- [17] T. Sogabe, Q. Shen, and K. Yamaguchi, "Recent progress on quantum dot solar cells: a review," *Journal of Photonics for Energy*, vol. 6, no. 4, article 040901, 2016.
- [18] F. Cappelluti, M. Gioannini, and A. Khalili, "Impact of doping on InAs/GaAs quantum-dot solar cells: a numerical study on photovoltaic and photoluminescence behavior," *Solar Energy Materials and Solar Cells*, vol. 157, pp. 209–220, 2016.
- [19] D. Bimberg, M. Grundmann, and N. N. Ledentsov, *Quantum Dot Heterostructures*, John Wiley & Sons, 1999.
- [20] G. Jolley, L. Fu, H. F. Lu, H. H. Tan, and C. Jagadish, "The role of intersubband optical transitions on the electrical properties of InGaAs/GaAs quantum dot solar cells," *Progress in Photovoltaics*, 2012.
- [21] G. A. Kosinovsky, "Threshold current and modulation response of semiconductor lasers," PhD Thesis, 1995.
- [22] T. R. Nielsen, P. Gartner, and F. Jahnke, "Many-body theory of carrier capture and relaxation in semiconductor quantum-dot lasers," *Physical Review B*, vol. 69, no. 23, article 235314, 2004.
- [23] G. A. Narvaez, G. Bester, and A. Zunger, "Carrier relaxation mechanisms in self-assembled (In, Ga) As/Ga As quantum dots: efficient $P \rightarrow S$ Auger relaxation of electrons," *Physical Review B*, vol. 74, no. 7, article 075403, 2006.
- [24] K. Schuh, P. Gartner, and F. Jahnke, "Combined influence of carrier-phonon and coulomb scattering on the quantum-dot population dynamics," *Physical Review B*, vol. 87, no. 3, article 035301, 2013.
- [25] S. Tomić, "Intermediate-band solar cells: influence of band formation on dynamical processes in InAs/GaAs quantum dot arrays," *Physical Review B*, vol. 82, no. 19, article 195321, 2010.
- [26] J. Siegert, S. Marcinkevičius, and Q. X. Zhao, "Carrier dynamics in modulation-doped InAs/GaAs quantum dots," *Physical Review B*, vol. 72, no. 8, 2005.
- [27] F. Cappelluti, A. Khalili, and M. Gioannini, "Open circuit voltage recovery in quantum dot solar cells: a numerical study on the impact of wetting layer and doping," *IET Optoelectronics*, vol. 11, no. 2, pp. 44–48, 2017.
- [28] P. W. Fry, J. J. Finley, L. R. Wilson et al., "Electric-field-dependent carrier capture and escape in self-assembled InAs/GaAs quantum dots," *Applied Physics Letters*, vol. 77, no. 26, pp. 4344–4346, 2000.

- [29] T. Müller, F. Schrey, G. Strasser, and K. Unterrainer, "Ultrafast intraband spectroscopy of electron capture and relaxation in InAs/GaAs quantum dots," *Applied Physics Letters*, vol. 18, no. 17, pp. 3572–3574, 2003.
- [30] L. A. Pettersson, L. S. Roman, and O. Inganäs, "Modeling photocurrent action spectra of photovoltaic devices based on organic thin films," *Journal of Applied Physics*, vol. 86, no. 1, pp. 487–496, 1999.
- [31] F. Bertazzi, F. Cappelluti, S. D. Guerrieri, F. Bonani, and G. Ghione, "Self-consistent coupled carrier transport full-wave EM analysis of semiconductor traveling-wave devices," *IEEE Transactions on Microwave Theory and Techniques*, vol. 54, no. 4, pp. 1611–1618, 2006.
- [32] D. Kim, M. Tang, J. Wu et al., "Si-doped InAs/GaAs quantum-dot solar cell with AlAs cap layers," *IEEE Journal of Photovoltaics*, vol. 6, no. 4, pp. 906–911, 2016.
- [33] H. Y. Liu, I. R. Sellers, T. J. Badcock et al., "Improved performance of 1.3 μm multilayer InAs quantum-dot lasers using a high-growth-temperature GaAs spacer layer," *Applied Physics Letters*, vol. 85, no. 5, pp. 704–706, 2004.
- [34] H. Y. Liu, S. L. Liew, T. Badcock et al., "p-doped 1.3 μm InAs/GaAs quantum-dot laser with a low threshold current density and high differential efficiency," *Applied Physics Letters*, vol. 89, no. 7, article 073113, 2006.
- [35] F. K. Tutu, I. R. Sellers, M. G. Peinado et al., "Improved performance of multilayer InAs/GaAs quantum-dot solar cells using a high-growth-temperature GaAs spacer layer," *Journal of Applied Physics*, vol. 111, no. 4, article 046101, 2012.
- [36] M. Wolf and H. Rauschenbach, "Series resistance effects on solar cell measurements," *Advanced Energy Conversion*, vol. 3, no. 2, pp. 455–479, 1963.
- [37] H. L. Wang, F. H. Yang, and S. L. Feng, "Photoluminescence in Si and Be directly doped self-organized InAs/GaAs quantum dots," *Journal of Crystal Growth*, vol. 212, no. 1-2, pp. 35–38, 2000.
- [38] A. Markus, M. Rossetti, V. Calligari, J. Chen, and A. Fiore, "Role of thermal hopping and homogeneous broadening on the spectral characteristics of quantum dot lasers," *Journal of Applied Physics*, vol. 98, no. 10, article 104506, 2005.
- [39] M. P. Lumb, M. A. Steiner, J. F. Geisz, and R. J. Walters, "Incorporating photon recycling into the analytical drift-diffusion model of high efficiency solar cells," *Journal of Applied Physics*, vol. 116, no. 19, article 194504, 2014.
- [40] A. Musu, F. Cappelluti, T. Aho, V. Polojärvi, T. K. Niemi, and M. Guina, "Nanostructures for light management in thin-film GaAs quantum dot solar cells," in *Solid-State Lighting*, no. article JW4A.45, 2016Optical Society of America, 2016.
- [41] Sopra database. 1995-2016 Software Spectra, Inc.<http://sspectra.com/sopra.html>.
- [42] C. G. Bailey, D. V. Forbes, R. P. Raffaele, and S. M. Hubbard, "Near 1 V open circuit voltage InAs/GaAs quantum dot solar cells," *Applied Physics Letters*, vol. 98, no. 16, article 163105, 2011.
- [43] P. Lam, S. Hatch, J. Wu et al., "Voltage recovery in charged InAs/GaAs quantum dot solar cells," *Nano Energy*, vol. 6, pp. 159–166, 2014.
- [44] S. J. Polly, D. V. Forbes, K. Driscoll, S. Hellstrom, and S. M. Hubbard, "Delta-doping effects on quantum-dot solar cells," *IEEE Journal of Photovoltaics*, vol. 4, no. 4, pp. 1079–1085, 2014.
- [45] S. Sanguinetti, D. Colombo, M. Guzzi et al., "Carrier thermodynamics in InAs/In_xGa_{1-x}As quantum dots," *Physical Review B*, vol. 74, no. 20, article 205302, 2006.
- [46] T. Kita, R. Hasagawa, and T. Inoue, "Suppression of nonradiative recombination process in directly Si-doped InAs/GaAs quantum dots," *Journal of Applied Physics*, vol. 110, no. 10, article 103511, 2011.

Research Article

Effect of Annealing Process on $\text{CH}_3\text{NH}_3\text{PbI}_{3-x}\text{Cl}_x$ Film Morphology of Planar Heterojunction Perovskite Solar Cells with Optimal Compact TiO_2 Layer

Dan Chen, Xiaoping Zou, Hong Yang, Ningning Zhang, Wenbin Jin, Xiao Bai, and Ying Yang

Research Center for Sensor Technology, Beijing Key Laboratory for Sensor, Ministry of Education Key Laboratory for Modern Measurement and Control Technology, School of Applied Sciences, Beijing Information Science and Technology University, Jianxiangqiao Campus, Beijing 100101, China

Correspondence should be addressed to Xiaoping Zou; xpzou2014@163.com

Received 23 May 2017; Revised 4 August 2017; Accepted 13 August 2017; Published 8 November 2017

Academic Editor: Matthias Auf der Maur

Copyright © 2017 Dan Chen et al. This is an open access article distributed under the Creative Commons Attribution License, which permits unrestricted use, distribution, and reproduction in any medium, provided the original work is properly cited.

The morphology of compact TiO_2 film used as an electron-selective layer and perovskite film used as a light absorption layer in planar perovskite solar cells has a significant influence on the photovoltaic performance of the devices. In this paper, the spin coating speed of the compact TiO_2 is investigated in order to get a high-quality film and the compact TiO_2 film exhibits pinhole- and crack-free films treated by 2000 rpm for 60 s. Furthermore, the effect of annealing process, including annealing temperature and annealing program, on $\text{CH}_3\text{NH}_3\text{PbI}_{3-x}\text{Cl}_x$ film morphology is studied. At the optimal annealing temperature of 100°C , the $\text{CH}_3\text{NH}_3\text{PbI}_{3-x}\text{Cl}_x$ morphology fabricated by multistep slow annealing method has smaller grain boundaries and holes than that prepared by one-step direct annealing method, which results in the reduction of grain boundary recombination and the increase of V_{oc} . With all optimal procedures, a planar fluorine-doped tin oxide (FTO) substrate/compact TiO_2 / $\text{CH}_3\text{NH}_3\text{PbI}_{3-x}\text{Cl}_x$ /Spiro-MeOTAD/Au cell is prepared for an active area of 0.1 cm^2 . It has achieved a power conversion efficiency (PCE) of 14.64%, which is 80.3% higher than the reference cell (8.12% PCE) without optimal perovskite layer. We anticipate that the annealing process with optimal compact TiO_2 layer would possibly become a promising method for future industrialization of planar perovskite solar cells.

1. Introduction

Perovskite solar cells (PSCs) have developed a variety of device structures, since the first report from Kojima et al. in 2009 [1], such as mesoporous, meso-superstructure, planar heterojunction, and hole-blocking layer-free structure [2–5]. The planar heterojunction is considered to be the most competitive construction on account of their simplified fabricating procedure. Up to date, several materials could be chosen as electron-selective layer (ESL), for instance, ZnO [6, 7], TiO_2 [8], Zn_2SnO_4 [9], SnO_2 [10], fullerene, PCBM [11] and so on. And many different advanced thin-film technologies have been developed for obtaining high-quality perovskite layer, such as one-step spin coating [2], two-step deposition [8, 12, 13], vapor-assisted solution process [14], dual-source thermal evaporation [4], compositional engineering [15],

and interface engineering [16]. Compact TiO_2 (c- TiO_2) film and $\text{CH}_3\text{NH}_3\text{PbI}_{3-x}\text{Cl}_x$ film are the most commonly used materials in planar heterojunction PSCs due to the excellent ability of carrier extraction and long carrier diffusion length [17], respectively. However, no matter what material is chosen or how method is adopted, the morphology of both two layers is regarded as one of the most critical issues.

The ESL acts as the blocking layer to prevent photogenerated holes from reaching the FTO substrate, which would or else short circuit the device. Karthikeyan and Thelakkat demonstrated that an optimum thickness of c- TiO_2 film, which prepared by spray pyrolysis deposition, was 120–150 nm for the high cell performance in 2008 [18]. Excellent layer thickness obtained for c- TiO_2 film employed by spin coating method was 80–180 nm, which was reported by Kim [2]. Lellig reported that the best values of c- TiO_2 film ranged

from 40 to 70 nm by using an amphiphilic diblock copolymer as a functional template [19]. It must be mentioned that spin coating is the most frequently used method owing to exceptional advantages such as easy operation and low cost. Several excellent reviews so far have focused on the optimum thickness of the ESL, nonetheless, no systematic study concerning the effect of spin coating rate on the morphology of ESL.

It is commonly known that $\text{CH}_3\text{NH}_3\text{PbI}_{3-x}\text{Cl}_x$ film has appealing physical properties, for example, broad light absorption range, high extinction coefficients, a small exciton binding energy, and a tunable bandgap. Accompanied by recent developments of improving the quality of the light absorption layer, the PCE of PSCs has risen from 3.8% [1] to 22.1% [20]. For typical annealing program, Huang et al. showed the highest efficiency of ~13.58% in PSCs with Ag electrode and 0.07 cm^2 active area by multistep slow annealing method for the ultimate temperature of 95°C in 2015 [21]. It is worthwhile mentioning that the annealing procedure, including annealing temperature and annealing program, has an essential influence on $\text{CH}_3\text{NH}_3\text{PbI}_{3-x}\text{Cl}_x$ film morphology, in spite of many efforts that have been reported to control the quality of the light harvest layer.

In this article, we show that the most excellent rate for the spin coating ESL is 2000 rpm for 60 s. Moreover, two different programs, one-step (OS) direct annealing method and multistep (MS) slow annealing method, are employed to prepare the high-quality perovskite film. We reveal that the best temperature of OS direct annealing method is 100°C . The average PCE of MS devices is 47.3% higher than that of devices produced by OS method results from the smaller grain boundary recombination and the higher Voc and FF. Our solar cell with the Au electrode, 0.1 cm^2 active area, and optimal compact TiO_2 layer has achieved a best power conversion efficiency (PCE) of 14.64% by MS annealing method for the ultimate temperature of 100°C .

2. Experimental and Methods

2.1. Materials. The zinc powder was purchased from Sinopharm Chemical Reagent Beijing Co. Ltd. and Au from ZhongNuo Advanced Material Technology Co. Ltd. Isopropanol was purchased from Beijing Chemical Works (AR) or Sigma-Aldrich (99.8%). Ethanol, acetone, diethyl ether, and hydrochloric acid were purchased from Beijing Chemical Works, and TiCl_4 , methylamine alcohol (33%), and hydrogen iodide (HI, 55%–58%) were purchased from Aladdin Industrial Corporation. PbCl_2 , N,N-dimethylformamide (99.8%), isopropyl titanate (99.8%), 4-tert-butylpyridine (TBP, 96%), Spiro-MeOTAD (2,2',7,7'-tetrakis-(N,N-dimethoxyphenylamine)-9,9'-spirobifluorene), chlorobenzene, acetonitrile, and Li-bis (trifluoromethanesulfonyl) imide (Li-TFSI) ($\text{C}_2\text{F}_6\text{LiNO}_4\text{S}_2$, 99.95%) were purchased from Sigma-Aldrich. Deionized water was prepared by Research Center for Sensor Technology, Beijing Key Laboratory for Sensor, Beijing Information Science and Technology University.

2.2. The Preparation of Precursor. Hydrochloric (HCl) acid solution (4 mol/L) was prepared by mixing deionized water (667 mL) into hydrochloric acid (333 mL, 12 mol/L). 2 M

HCl (35 mL) was dissolved in 2.53 ml of isopropanol (AR), and the mixture was defined as A solution. Isopropyl titanate solution was fabricated by dissolving $369\text{ }\mu\text{g}$ isopropyl titanate in 2.53 ml of isopropanol (99.8%), to which the A solution was added drop by drop by high rate stirring, and then the final solution was filtered. $\text{CH}_3\text{NH}_3\text{I}$ was synthesized by stirring the mixture solution of methylamine alcohol (24 mL, 33 wt%) and hydrogen iodide (HI, 55–58 wt%) at 0°C for 2 h. The mixture was evaporated in a rotavap, and the remaining solid was washed with diethyl ether and dried three times. The formation of white powder indicated the successful crystallization. $\text{CH}_3\text{NH}_3\text{PbI}_{3-x}\text{Cl}_x$ perovskite precursor solution was prepared as follows. 0.244 g PbCl_2 (0.88 mM) and 0.42 g $\text{CH}_3\text{NH}_3\text{I}$ (2.64 mM) were dissolved in 1 mL N,N-dimethylformamide. The mixture was stirred for 180 min at 90°C . 520 mg of Li-TFSI was dissolved in 1 mL acetonitrile, and the mixture was defined as B solution. 72.3 mg of Spiro-MeOTAD and $28.8\text{ }\mu\text{L}$ of TBP were dissolved in chlorobenzene (1 mL), to which the B solution ($17.5\text{ }\mu\text{L}$) was added and stirred, in order to prepare the hole transport material precursor solution.

2.3. Device Fabrication. The FTO ($1.5 \times 1.5\text{ cm}^2$, $<14\text{ }\Omega/\text{sq}$, 2.2 mm thick, Pilkington, Solar Energy Technology Co. Ltd., Wuhan Jinge, China) substrates were firstly etched using Zn powder and hydrochloric acid solution for 2 min to form the retained area of $1.5 \times 1.0\text{ cm}^2$ as patterned electrode. The etched FTO substrates were cleaned according to the literature procedures [22]. And the following procedures were done in a nitrogen-filled glovebox. The isopropyl titanate solution was spin coated on the pretreated FTO to prepare the c- TiO_2 layer at 1000 rpm, 2000 rpm, and 3000 rpm for 60 s, before drying at 125°C for 10 min and then annealing at 500°C for 30 min. The ESLs were then immersed in 0.04 M of TiCl_4 aqueous solution to improve interface contact with the light harvester [23–25]. The c- TiO_2 layer was immersed in TiCl_4 aqueous solution for 30 min at 70°C . After washed with deionized water, the film was dried with N_2 flow and sintered at 500°C for 30 min. The $\text{CH}_3\text{NH}_3\text{PbI}_{3-x}\text{Cl}_x$ film was deposited on the ESL by spin coating the $\text{CH}_3\text{NH}_3\text{PbI}_{3-x}\text{Cl}_x$ perovskite precursor solution at 2000 rpm for 45 s and then treated by different calcined programs as follow. The annealing temperatures were directly raise to 90°C , 100°C , 110°C , 120°C , or 130°C for OS direct annealing method. The annealing time for every temperature was 90 min, which was chosen according to the literature [26]. For the MS slow annealing method, the annealing temperature was raised from 30°C to 100°C , and the annealing times for 30°C , 40°C , and 50°C were both 5 min, for 60°C , 70°C , 80°C , and 90°C were both 10 min, and the ultimate time was 90 min for 100°C . Once the $\text{CH}_3\text{NH}_3\text{PbI}_{3-x}\text{Cl}_x$ films deposited well, the hole transport material precursor solution was spin coated at 2000 rpm for 45 s. Finally, a metal contact electrode (~60 nm), such as Al or Au, was deposited on the Spiro-MeOTAD using thermal evaporation at a pressure of 1×10^{-6} mbar.

2.4. Material and Device Characterizations. The morphology of all films was observed with a field emission scanning

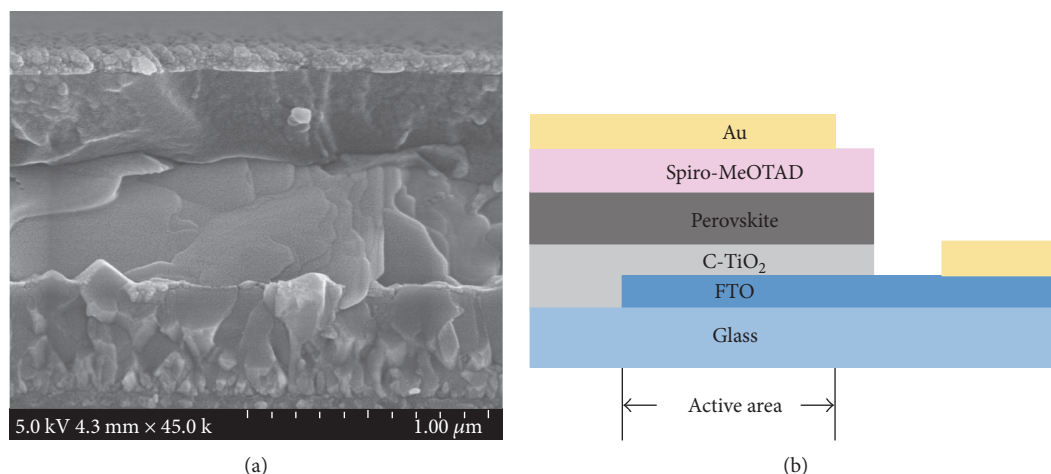


FIGURE 1: Representative cross-sectional SEM image (a) and schematic illustration (b) of the planar heterojunction perovskite solar cell.

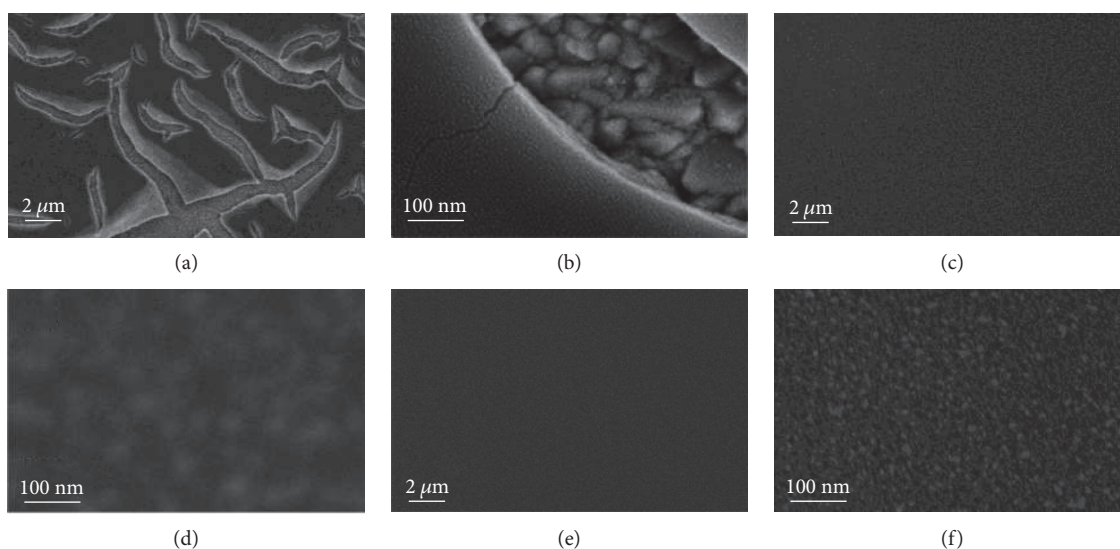


FIGURE 2: Top view SEM images of $c\text{-TiO}_2$ film with different spin coating speeds for 60 s. (a), (c), and (e) the low magnification and (b), (d), and (f) the high magnification images for 1000 rpm, 2000 rpm, and 3000 rpm, respectively.

electron microscope (FESEM, Hitachi S-4800). X-ray diffraction (XRD) patterns were performed with Bruker D8 Focus (Bruker Corporation, Germany) to analyze the crystal structure of the samples. UV-vis absorption spectra were measured by Cary 5000 (Varian, America). The current-voltage curves were characterized using a V3-400 (Princeton Applied Research) under AM 1.5G one sun illumination (100 mW/cm^2) with a scan rate of 0.1 V/s , which was simulated by solar simulator (Newport Oriel Class 3A) equipped with Xenon lamp (L2175). The thickness of TiO_2 ESL was characterized with NanoMap Surface Profiler (AEP Technology, USA).

3. Results and Discussion

3.1. Effect of the Different Spin Coating Speeds on the Morphology of the $c\text{-TiO}_2$ Film. Figure 1 presents a cross-sectional scanning electron microscopy (SEM) image of a

representative planar heterojunction solar cell device. It is generally accepted that the perovskite material harvests light to generate hole-electron pairs and $c\text{-TiO}_2$ film suppresses the electrical contact between FTO and photovoltaic layer [27].

To achieve a better understanding of the effectiveness of the different spin coating speeds on the morphology of the $c\text{-TiO}_2$ film, the SEM images of three different speeds are shown in Figure 2. Figures 2(a), 2(c), and 2(e) are the low magnification, and Figures 2(b), 2(d), and 2(f) are the high magnification images of $c\text{-TiO}_2$ film for 1000 rpm, 2000 rpm, and 3000 rpm, respectively. The SEM images highlight the variation in the film surface morphology of the ELS. The speed of 2000 rpm produces better surface coverage and smaller film defect, as compared with the $c\text{-TiO}_2$ films prepared using other two speeds. The top views of a film prepared with 2000 rpm (Figures 2(c) and 2(d)) reveal that the FTO is fully covered by the more

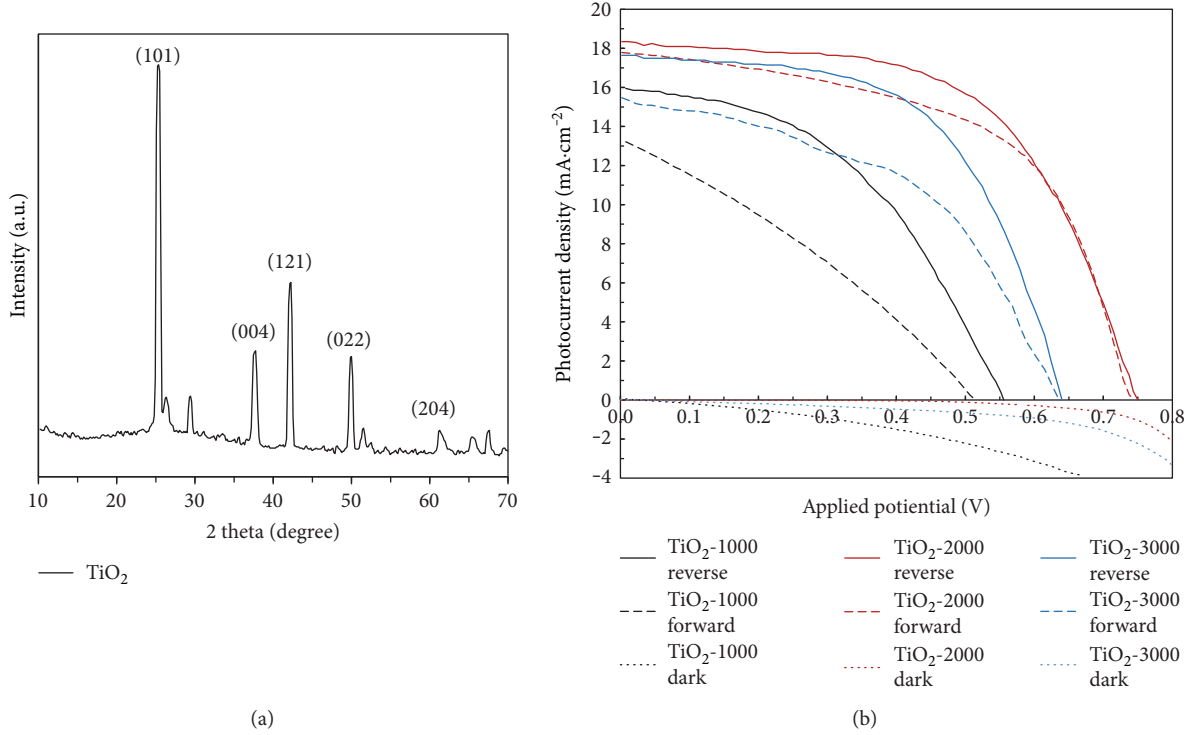


FIGURE 3: (a) XRD pattern of c -TiO₂ film prepared with 2000 rpm. (b) J-V characteristics of devices based on various c -TiO₂ films.

uniform and smooth c -TiO₂ layer. Especially, many cracks can be observed from the film when fabricated with the speed of 1000 rpm (Figures 2(a) and 2(b)), and numerous pinholes can be discovered from the film when obtained with speed of 3000 rpm (Figures 2(e) and 2(f)).

We analyze the phase purity of the c -TiO₂ film prepared with 2000 rpm by XRD (Figure 3(a)). For the c -TiO₂ film, the diffraction peaks are located at $2\theta = 25.3^\circ$ and 38.0° , corresponding to the 101 and 004 planes of the anatase structure of TiO₂ (JCPDS card number 21-1272). The diffraction peak of TiO₂ (101) plane showed a high intensity, indicating that the c -TiO₂ film by spin coating has a well-defined and high-purity anatase phase.

In this study, we prepare PSCs using three kinds of c -TiO₂ films as ELS by different spin coating speeds and measure the J-V curves of the devices with an active area of 0.1 cm^2 to investigate the influence of the rate on the ELS. Figure 3(b) shows the J-V curves of three best cells, and the detailed photovoltaics data extracted from the reversed J-V curves for these devices can be found in Table 1. Samples TiO₂-1000, TiO₂-2000, and TiO₂-3000 are corresponding to the devices manufactured with 1000 rpm, 2000 rpm, and 3000 rpm, respectively. From this data, the 2000 rpm cell gives a PEC of 8.12% corresponding to a J_{SC} of $18.3 \text{ mA}\cdot\text{cm}^{-2}$, a V_{oc} of 0.75 V, and a FF of 0.58 and has the lowest series resistance (R_s) which is $\sim 7.59 \Omega\cdot\text{cm}^2$. The good performance of this device is mainly due to a decrease in the R_s , as is apparent from Table 1. We attribute this lowest R_s to the best morphology of the c -TiO₂ films which has smaller cracks and pinholes, in contrast to the morphology of the 1000 rpm and 3000 rpm films. The

TABLE 1: Photovoltaic performance parameters extracted from reversed J-V curves (Figure 3(b)).

Sample	$J_{sc}/\text{mA}\cdot\text{cm}^{-2}$	V_{oc}/V	FF/%	PCE/%	$R_s/\Omega\cdot\text{cm}^2$
TiO ₂ -1000	15.9	0.55	0.45	4.05	12.98
TiO ₂ -2000	18.3	0.75	0.58	8.12	7.59
TiO ₂ -3000	17.7	0.64	0.58	6.57	9.25

hysteresis observed in TiO₂-2000 cell is weak compared to the hysteresis in other two samples. The previous work investigates that the FTO/ c -TiO₂ interface and c -TiO₂/CH₃NH₃PbI_{3-x}Cl_x interface are the origins of hysteresis [28]. Furthermore, the deeper trap states, ferroelectric polarization, and ion migration may also be responsible for the hysteresis in PSCs. The dark J-V curves indicate that the device with 2000 rpm TiO₂ layer exhibits a better diode behaviour than the samples with other two kinds of TiO₂ layers. The direct contacts between CH₃NH₃PbI_{3-x}Cl_x layer and FTO may be responsible for the poor rectification ability of the TiO₂-1000 and TiO₂-3000 cells [5].

According to Ke et al.'s work [29], the thickness of c -TiO₂ layer has a huge influence on the photovoltaic performance on the PSCs. We characterized the thickness of TiO₂ ESL using the surface profiler. The thicknesses of c -TiO₂ layers prepared by 1000 rpm, 2000 rpm, and 3000 rpm are $\sim 67 \text{ nm}$, $\sim 47 \text{ nm}$, and $\sim 36 \text{ nm}$, respectively. The 67 nm TiO₂ ESL is too thick to transfer the electron from the light absorption layer to the FTO. The too thin c -TiO₂ layer (36 nm) leads to a serious recombination process because the FTO is not fully covered with the c -TiO₂ layers, and the light absorption

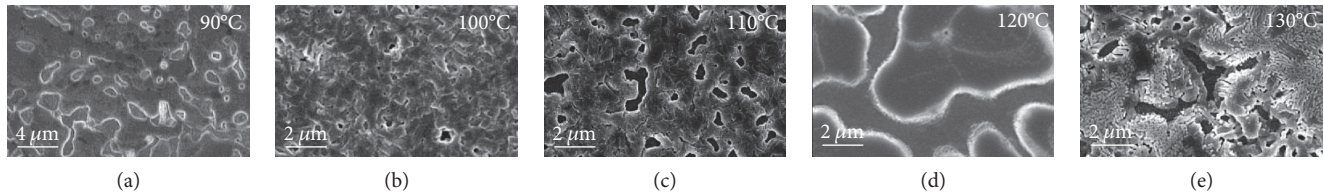


FIGURE 4: Top view SEM images of $\text{CH}_3\text{NH}_3\text{PbI}_{3-x}\text{Cl}_x$ films deposited on the $c\text{-TiO}_2$ layer with diverse OS annealing temperatures. (a) 90°C , (b) 100°C , (c) 110°C , (d) 120°C , and (e) 130°C .

layer contacts with the FTO directly. The optimum thickness of $c\text{-TiO}_2$ layers is ~ 47 nm. In this article, we employ the $c\text{-TiO}_2$ film prepared by 2000 rpm method as the ELS in the following fabrication of PSCs due to its excellent photovoltaic performance.

3.2. Effect of the OS Direct Annealing Temperature on the Morphology of the Perovskite Film. Figure 4 exhibits the top view SEM images of $\text{CH}_3\text{NH}_3\text{PbI}_{3-x}\text{Cl}_x$ films deposited on the $c\text{-TiO}_2$ layer with diverse OS direct annealing temperatures of (a) 90°C , (b) 100°C , (c) 110°C , (d) 120°C , and (d) 130°C . As the annealing temperature increases from 90°C to 100°C , the number of pinholes is significantly decreased. At a temperature of 100°C , the perovskite films show denser packing and the coverage of perovskite film is obviously improved even though some $c\text{-TiO}_2$ still remains uncovered. However, as the annealing temperature increases from 110°C to 130°C , the $c\text{-TiO}_2$ layer uncovered with $\text{CH}_3\text{NH}_3\text{PbI}_{3-x}\text{Cl}_x$ films becomes pronounced due to the size of pinholes and is significantly increased and the perovskite film shows polydisperse perovskite islands. These consequences are in qualitative agreement with previous researches on the thermal annealing precursor of $\text{CH}_3\text{NH}_3\text{I}$ and PbCl_2 , where it was found that high temperatures resulted in the rapid growth from a few nucleation sites leading to the formation of large crystalline islands and the associated large gaps in between [30]. The increase in the uncovered $c\text{-TiO}_2$ with increasing annealing temperature indicates that the lower annealing temperature (100°C) is appropriate for the preparation of maximum coverage $\text{CH}_3\text{NH}_3\text{PbI}_{3-x}\text{Cl}_x$ films, which is consistent with the research in the literature [31].

In Figure 5, we compare the XRD patterns of $\text{CH}_3\text{NH}_3\text{PbI}_{3-x}\text{Cl}_x$ films prepared by different annealing temperatures and observe the appearance of a series of diffraction peaks that are in good agreement with the literature data on the orthorhombic phase of $\text{CH}_3\text{NH}_3\text{PbI}_{3-x}\text{Cl}_x$. The main diffraction peaks, assigned to the (110), (220), and (330) peaks at 13.99° , 28.36° , and 43.10° , respectively, are in identical positions for every temperature films, indicating that all temperatures have manufactured the same mixed-halide perovskite with an orthorhombic crystal structure [4, 32]. At a temperature of 90°C , the diffraction peaks are located at $2\theta = 15.5^\circ$ and 31.3° , corresponding to the 100 and 200 planes of the single-phase of cubic $\text{CH}_3\text{NH}_3\text{PbCl}_3$ [33]. $\text{CH}_3\text{NH}_3\text{PbCl}_3$ is not suitable for the absorber layer of efficient PSCs due to its significantly higher energy bandgap than that required to achieve the Shockley-Queisser limit [34]. At the temperature of 100°C , 110°C ,

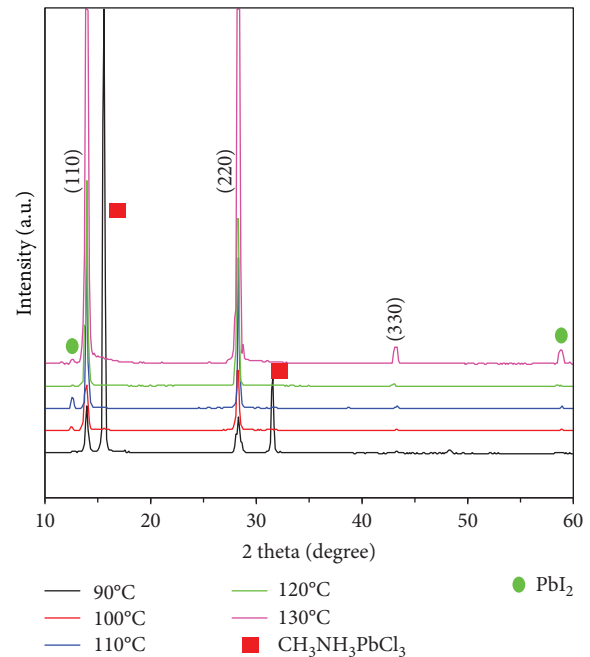


FIGURE 5: XRD patterns of $\text{CH}_3\text{NH}_3\text{PbI}_{3-x}\text{Cl}_x$ films annealing at different OS direct annealing temperatures on TiO_2 layers. The red squares and green circles indicate the peaks associated with the $\text{CH}_3\text{NH}_3\text{PbCl}_3$ and PbI_2 , respectively.

and 130°C , the diffraction peak that appears at 12.53° can be indexed to the (001) planes of PbI_2 . Notably, looking closely at the region of the (110) diffraction peak at 13.99° , there is a small signal of a diffraction peak at 12.53° (the (001) peak for PbI_2) and no measurable diffraction peak at 15.5° (the (100) peak for $\text{CH}_3\text{NH}_3\text{PbCl}_3$), manifesting a high level of phase purity of $\text{CH}_3\text{NH}_3\text{PbI}_{3-x}\text{Cl}_x$ films by the annealing temperature of 120°C . Taking into account the SEM images and XRD patterns, we employed 100°C in our investigations.

3.3. Effect of Different Annealing Programs on the Morphology of the Perovskite Film. To further address the effect of the annealing program on the morphology of the perovskite film, two different annealing programs for the ultimate temperature of 100°C , OS, and MS, were adopted for $\text{CH}_3\text{NH}_3\text{PbI}_{3-x}\text{Cl}_x$ perovskite film treatment. Samples $\text{CH}_3\text{NH}_3\text{PbI}_{3-x}\text{Cl}_x$ (MS) and $\text{CH}_3\text{NH}_3\text{PbI}_{3-x}\text{Cl}_x$ (OS) are corresponding to the films manufactured with MS slow and OS direct annealing method, respectively. The XRD patterns and the UV-vis absorption spectra of $\text{CH}_3\text{NH}_3\text{PbI}_{3-x}\text{Cl}_x$

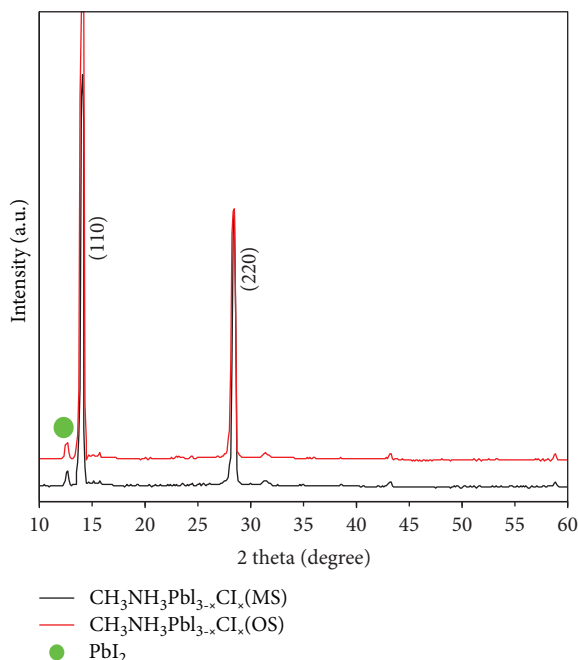


FIGURE 6: XRD patterns of $\text{CH}_3\text{NH}_3\text{PbI}_{3-x}\text{Cl}_x$ films deposited on $c\text{-TiO}_2$ layers with two different annealing programs for the ultimate temperature of 100°C . The green circles indicate the peaks of PbI_2 .

films deposited on $c\text{-TiO}_2$ layers with two different annealing programs are shown in Figures 6 and 7, respectively. The peaks at 13.99° and 28.36° are assigned to the $\text{CH}_3\text{NH}_3\text{PbI}_{3-x}\text{Cl}_x$ phase, revealing that both two anneal methods have fabricated the same orthorhombic perovskite structured $\text{CH}_3\text{NH}_3\text{PbI}_{3-x}\text{Cl}_x$ crystals, and the narrow diffraction peaks represent that the films have long-range crystalline domains [3]. No new diffraction peaks or peak shifts are observed, indicating that the crystal structure of the two sintered $\text{CH}_3\text{NH}_3\text{PbI}_{3-x}\text{Cl}_x$ films is the same, which is consistent with the previous report [21]. The weak peak centered at 12.53° is attributed to PbI_2 , and the $\text{CH}_3\text{NH}_3\text{PbCl}_3$ phase (with a peak at 15.5°) does not appear.

The absorption spectra (Figure 7) manifest the similar light-harvesting capabilities over the visible to near-IR spectrum regardless of the different annealing programs adopted. Both two films exhibit the roughly same absorption edge at about 780 nm (corresponding to $\sim 1.55\text{ eV}$ optical bandgap of $\text{CH}_3\text{NH}_3\text{PbI}_{3-x}\text{Cl}_x$), which is consistent with the previous studies [35]. However, the absorption edge of MS film shows a slightly red shift, which should be due to the improved crystallinity with this method [36]. And this result is consistent with the conclusion from Figure 8.

However, the SEM pictures presented for two magnifications (Figure 8) reveal stark differences in perovskite film morphology prepared by two different annealing programs. Compared to the OS film, the film MS shows more homogeneous and dense surface morphology, which has a smaller number of pinholes and grain boundaries. According to the different surface morphologies of the perovskite films treated by the two programs, we can expect different photovoltaic

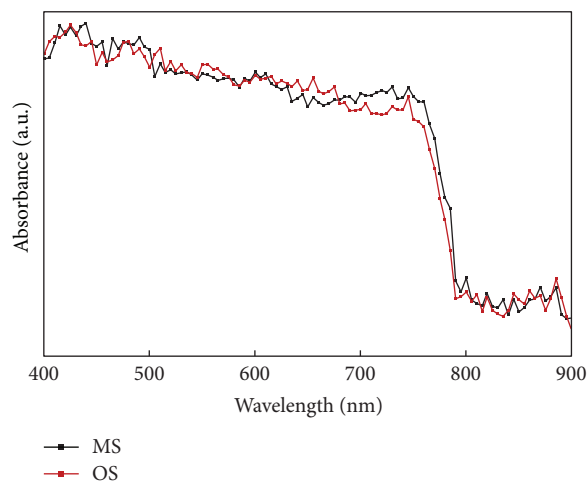


FIGURE 7: UV-vis absorption spectra of $\text{CH}_3\text{NH}_3\text{PbI}_{3-x}\text{Cl}_x$ films deposited on TiO_2 layers with two different annealing programs for the ultimate temperature of 100°C .

performance of devices. The complete cells, which are named MS-1 and MS-2, are fabricated by MS slow annealing method, and the OS-1 and OS-2 cells are corresponding to the control devices. In the OS devices, J_{sc} , V_{oc} , and fill factor are lower than the MS cells, as shown in the J-V curves presented in Figure 9. Since the main difference among these cells lies in $\text{CH}_3\text{NH}_3\text{PbI}_{3-x}\text{Cl}_x$, the variation of device parameters should be attributed to perovskite films. The significant decrease in these parameters (Table 2) may be a consequence of inferior perovskite film coverage [37]. The bare $c\text{-TiO}_2$ regions (corresponding to the blue circle areas of Figure 8(c)) with no perovskite coverage result in a drop of photocurrent attributing to no light absorption. Furthermore, the larger level of grain boundaries leads to the increase of nonradiative charge carrier recombination, which caused a drop in V_{oc} and FF. The higher parameters of devices by MS method account for a high average PCE (11.43%) values in this paper. The MS slow annealing method is obviously suitable for the preparation of highly efficient PSCs [21], due to the highly homogeneous perovskite structure which enables more uniform charge generation and collection as well as decreases the leakage with fewer shunt paths [37].

3.4. Device Performance with All Optimal Processes. We fabricate two cells by MS slow annealing method for the ultimate temperature of 100°C with optimal $c\text{-TiO}_2$ layer. Detailed photovoltaics data for these two devices extracted from J-V curves (Figure 10) can be found in Table 3. We derive values of $22.33\text{ mA}\cdot\text{cm}^{-2}$, 0.985 V , and 0.652 for J_{sc} , V_{oc} , and the fill factor, respectively, yielding a PCE of 14.64% for the best-performance cell measured at a light intensity of $P_{in} = 100\text{ mW}\cdot\text{cm}^{-2}$.

4. Conclusions

Our work represents a development of $c\text{-TiO}_2$ film depending on spin coating speed and an improvement of $\text{CH}_3\text{NH}_3\text{PbI}_{3-x}\text{Cl}_x$ perovskite film relying on the annealing

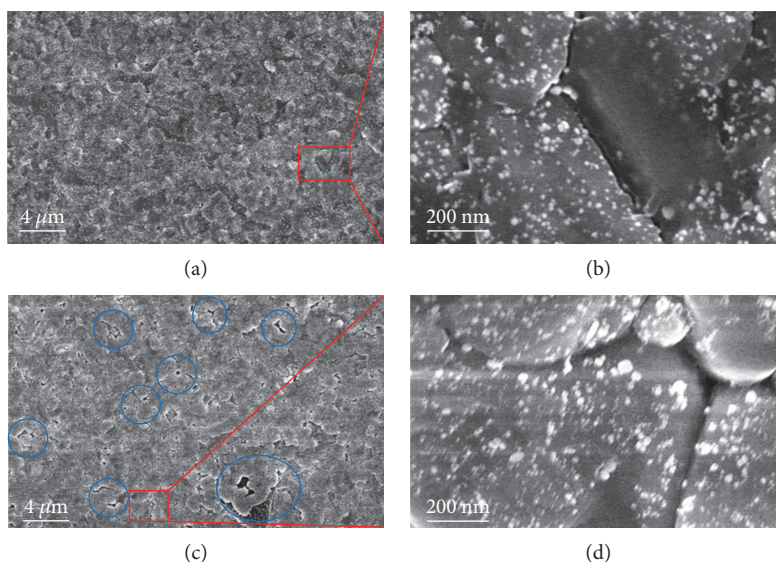


FIGURE 8: Top view SEM images of $\text{CH}_3\text{NH}_3\text{PbI}_{3-x}\text{Cl}_x$ films deposited on the c- TiO_2 layer with two different annealing programs, (a) MS slow and (c) OS direct annealing method. (b) and (d) are the enlarged images of the selected rectangular areas of (a) and (c), respectively.

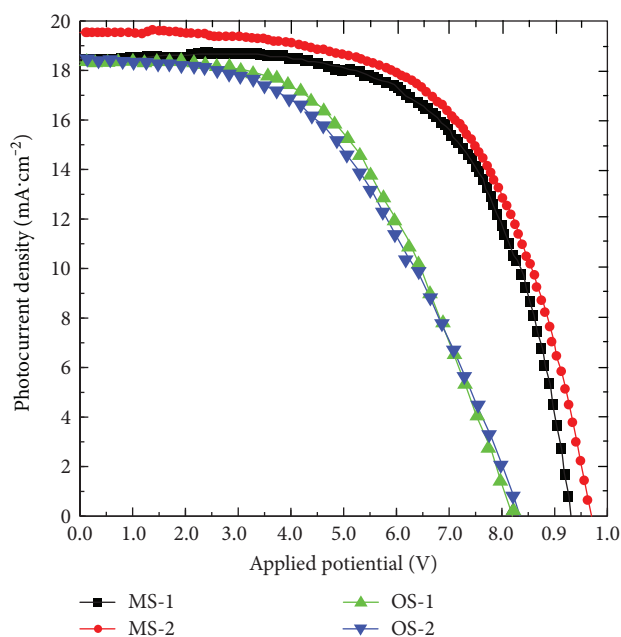


FIGURE 9: J-V characteristics of devices with $\text{CH}_3\text{NH}_3\text{PbI}_{3-x}\text{Cl}_x$ films treated by two different annealing programs.

TABLE 2: Photovoltaic performance parameters extracted from J-V curves (Figure 9).

Sample	J_{sc}/mAcm^{-2}	V_{oc}/V	FF/%	PCE/%
MS-1	18.44	0.92	0.63	11.15
MS-2	19.53	0.97	0.60	11.7
OS-1	18.34	0.82	0.52	7.94
OS-2	18.46	0.83	0.48	7.57

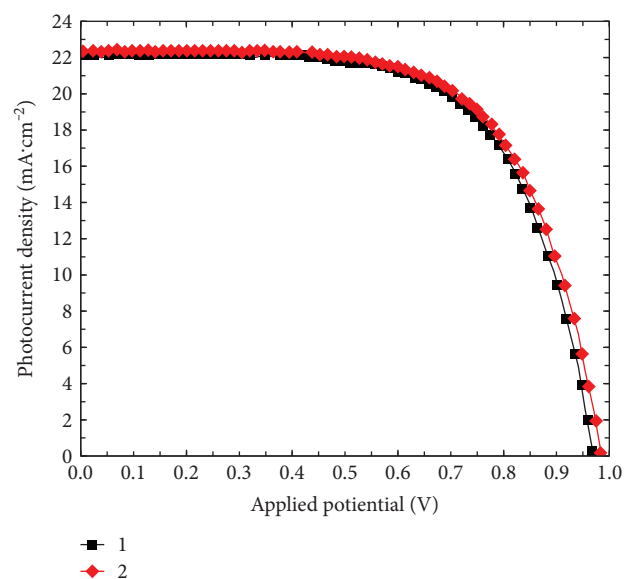


FIGURE 10: J-V curves of two devices with all optimal processes measured under standard AM 1.5G illumination ($100 \text{ mW}/\text{cm}^2$).

TABLE 3: Photovoltaic performance parameters extracted from J-V curves (Figure 10).

Sample	$J_{sc}/\text{mA}\cdot\text{cm}^{-2}$	V_{oc}/V	FF/%	PCE/%
1	22.10	0.97	0.576	14.30
2	22.33	0.985	0.652	14.64

process. Emphatically, the morphology and photovoltaic properties of perovskite films produced by two annealing programs are compared. Spin coating of 2000 rpm for 60 s

is found to be the excellent approach for controlling morphology c-TiO₂ film. For the perovskite film, MS slow annealing method is better than OS direct annealing method for the ultimate temperature of 100°C because of the difference in morphology. Compared to the device with OS method, the efficiency is increased from 7.94% to 11.7% for the MS method and to 14.64% for the all optimal processes. This combination of optimal c-TiO₂ and MS slow annealing method for low temperature is expected to help push the organic-inorganic hybrid solar cells closer to commercial feasibility.

Conflicts of Interest

The authors declare that there is no conflict of interests regarding the publication of this paper.

Acknowledgments

This work was partially supported by Project of Natural Science Foundation of China (91233201 and 61376057), Project of Natural Science Foundation of Beijing (Z160002 and 3131001), the Opened Fund of the State Key Laboratory on Integrated Optoelectronics (no. IOSKL2016KF19), Beijing Key Laboratory for Sensors of BISTU (KF20171077203), and Science & Technology Innovation Projects of Master Graduate & Bachelor Student at BISTU.

References

- [1] A. Kojima, K. Teshima, Y. Shirai, and T. Miyasaka, "Organometal halide perovskites as visible-light sensitizers for photovoltaic cells," *Journal of the American Chemical Society*, vol. 131, no. 17, pp. 6050-6051, 2009.
- [2] H.-S. Kim, C.-R. Lee, J.-H. Im et al., "Lead iodide perovskite sensitized all-solid-state submicron thin film mesoscopic solar cell with efficiency exceeding 9%," *Scientific Reports*, vol. 2, p. 591, 2012.
- [3] M. M. Lee, J. Teuscher, T. Miyasaka, T. N. Murakami, and H. J. Snaith, "Efficient hybrid solar cells based on meso-structured organometal halide perovskites," *Science*, vol. 338, no. 6107, pp. 643-647, 2012.
- [4] M. Liu, M. B. Johnston, and H. J. Snaith, "Efficient planar heterojunction perovskite solar cells by vapour deposition," *Nature*, vol. 501, no. 7467, pp. 395-398, 2013.
- [5] W. Ke, G. Fang, J. Wan et al., "Efficient hole-blocking layer-free planar halide perovskite thin-film solar cells," *Nature Communications*, vol. 6, p. 6700, 2015.
- [6] N. P. Ariyanto, H. Abdullah, J. Syarif, B. Yulianto, and S. Shaari, "Fabrication of zinc oxide-based dye-sensitized solar cell by chemical bath deposition," *Functional Materials Letters*, vol. 3, no. 4, pp. 303-307, 2011.
- [7] D. Liu and T. L. Kelly, "Perovskite solar cells with a planar heterojunction structure prepared using room-temperature solution processing techniques," *Nature Photonics*, vol. 8, no. 2, pp. 133-138, 2014.
- [8] J. Burschka, N. Pellet, S. J. Moon et al., "Sequential deposition as a route to high-performance perovskite-sensitized solar cells," *Nature*, vol. 499, no. 7458, pp. 316-319, 2013.
- [9] Z. Li, Y. Zhou, C. Bao et al., "Vertically building Zn₂SnO₄ nanowire arrays on stainless steel mesh toward fabrication of large-area, flexible dye-sensitized solar cells," *Nanoscale*, vol. 4, no. 11, pp. 3490-3494, 2012.
- [10] J. Song, E. Zheng, J. Bian et al., "Low-temperature SnO₂-based electron selective contact for efficient and stable perovskite solar cells," *Journal of Materials Chemistry A*, vol. 3, no. 20, pp. 10837-10844, 2015.
- [11] J. Y. Jeng, Y. F. Chiang, M. H. Lee et al., "CH₃NH₃PbI₃ perovskite/fullerene planar-heterojunction hybrid solar cells," *Advanced Materials*, vol. 25, no. 27, pp. 3727-3732, 2013.
- [12] D. Bi, S. J. Moon, L. Häggman et al., "Using a two-step deposition technique to prepare perovskite (CH₃NH₃PbI₃) for thin film solar cells based on ZrO₂ and TiO₂ mesostructures," *RSC Advances*, vol. 3, no. 41, pp. 18762-18766, 2013.
- [13] Y. Wu, A. Islam, X. Yang et al., "Retarding the crystallization of PbI₂ for highly reproducible planar-structured perovskite solar cells via sequential deposition," *Energy & Environmental Science*, vol. 7, no. 9, pp. 2934-2938, 2014.
- [14] Q. Chen, H. Zhou, Z. Hong et al., "Planar heterojunction perovskite solar cells via vapor-assisted solution process," *Journal of the American Chemical Society*, vol. 136, no. 2, pp. 622-625, 2013.
- [15] N. J. Jeon, J. H. Noh, W. S. Yang et al., "Compositional engineering of perovskite materials for high-performance solar cells," *Nature*, vol. 517, no. 7535, pp. 476-480, 2015.
- [16] H. Zhou, Q. Chen, G. Li et al., "Interface engineering of highly efficient perovskite solar cells," *Science*, vol. 345, no. 6196, pp. 542-546, 2014.
- [17] G. Xing, N. Mathews, S. Sun et al., "Long-range balanced electron- and hole-transport lengths in organic-inorganic CH₃NH₃PbI₃," *Science*, vol. 342, no. 6156, pp. 344-347, 2013.
- [18] C. S. Karthikeyan and M. Thelakkat, "Key aspects of individual layers in solid-state dye-sensitized solar cells and novel concepts to improve their performance," *Inorganica Chimica Acta*, vol. 361, no. 3, pp. 635-655, 2008.
- [19] P. Lellig, M. A. Niedermeier, M. Rawolle et al., "Comparative study of conventional and hybrid blocking layers for solid-state dye-sensitized solar cells," *Physical Chemistry Chemical Physics*, vol. 14, no. 5, pp. 1607-1613, 2012.
- [20] NREL chart, Rev.04-14-2017, <https://www.nrel.gov/pv/assets/images/efficiency-chart.png>.
- [21] L. Huang, Z. Hu, J. Xu, K. Zhang, J. Zhang, and Y. Zhu, "Multi-step slow annealing perovskite films for high performance planar perovskite solar cells," *Solar Energy Materials and Solar Cells*, vol. 141, pp. 377-382, 2015.
- [22] N. N. Zhang, Y. J. Guo, X. Yin, M. He, and X. P. Zou, "Spongy carbon film deposited on a separated substrate as counter electrode for perovskite-based solar cell," *Materials Letters*, vol. 182, pp. 248-252, 2016.
- [23] Z. Liu, Q. Chen, Z. Hong et al., "Low-temperature TiO_x-compact layer for planar heterojunction perovskite solar cells," *ACS Applied Materials & Interfaces*, vol. 8, no. 17, pp. 11076-11083, 2016.
- [24] J. Park and M. Lee, "Performance enhancement of dye-sensitized solar cell with a TiCl₄-treated TiO₂ compact layer," *Electronic Materials Letters*, vol. 11, no. 2, pp. 271-275, 2015.
- [25] L. Cojocar, S. Uchida, Y. Sanehira, J. Nakazaki, T. Kubo, and H. Segawa, "Surface treatment of the compact TiO₂ layer for efficient planar heterojunction perovskite solar cells," *Chemistry Letters*, vol. 44, no. 5, pp. 674-676, 2015.
- [26] A. T. Barrows, A. J. Pearson, C. K. Kwak, A. D. F. Dunbar, A. R. Buckley, and D. G. Lidzey, "Efficient planar heterojunction

- mixed-halide perovskite solar cells deposited via spray-deposition,” *Energy & Environmental Science*, vol. 7, no. 9, pp. 2944–2950, 2014.
- [27] W. J. Zeng, X. M. Liu, H. P. Wang, D. Cui, R. Xia, and Y. Min, “Mechanism study on enhanced open-circuit voltage of perovskite solar cells with vapor-induced TiO_2 , as electron-transport layer,” *Thin Solid Films*, vol. 629, pp. 11–16, 2017.
- [28] A. K. Jena, H. W. Chen, A. Kogo, Y. Sanehira, M. Ikegami, and T. Miyasaka, “The Interface between FTO and the TiO_2 compact layer can be one of the origins to hysteresis in planar heterojunction perovskite solar cells,” *ACS Applied Materials & Interfaces*, vol. 7, no. 18, pp. 9817–9823, 2015.
- [29] W. Ke, G. Fang, J. Wang et al., “Perovskite solar cell with an efficient TiO_2 compact film,” *Applied Materials & Interfaces*, vol. 6, no. 18, pp. 15959–15965, 2014.
- [30] A. Dualeh, N. Tétreault, T. Moehl, P. Gao, M. K. Nazeeruddin, and M. Grätzel, “Effect of annealing temperature on film morphology of organic-inorganic hybrid perovskite solid-state solar cells,” *Advanced Functional Materials*, vol. 24, no. 21, pp. 3250–3258, 2014.
- [31] G. E. Eperon, V. M. Burlakov, P. Docampo, A. Goriely, and H. J. Snaith, “Morphological control for high performance, solution-processed planar heterojunction perovskite solar cells,” *Advanced Functional Materials*, vol. 24, no. 1, pp. 151–157, 2014.
- [32] Z. L. Zhang, B. Q. Men, Y. F. Liu, H. P. Gao, and Y. L. Mao, “Effects of precursor solution composition on the performance and I-V hysteresis of perovskite solar cells based on $\text{CH}_3\text{NH}_3\text{PbI}_{3-x}\text{Cl}_x$,” *Nanoscale Research Letters*, vol. 12, no. 84, p. 8, 2017.
- [33] N. Kitazawa, Y. Watanabe, and Y. Nakamura, “Optical properties of $\text{CH}_3\text{NH}_3\text{PbX}_3$ (X = halogen) and their mixed-halide crystals,” *Journal of Materials Science*, vol. 37, no. 17, pp. 3585–3587, 2002.
- [34] Y.-C. Chern, Y.-C. Chen, H.-R. Wu, H. W. Zan, H. F. Meng, and S. F. Horng, “Grain structure control and greatly enhanced carrier transport by $\text{CH}_3\text{NH}_3\text{PbCl}_3$ interlayer in two-step solution processed planar perovskite solar cells,” *Organic Electronics*, vol. 38, pp. 362–369, 2016.
- [35] D. Wang, Z. Liu, Z. Zhou et al., “Reproducible one-step fabrication of compact $\text{MAPbI}_{3-x}\text{Cl}_x$ thin films derived from mixed-lead-halide precursors,” *Chemistry of Materials*, vol. 26, no. 24, pp. 7145–7150, 2014.
- [36] D. Liu, L. Wu, C. Li et al., “Controlling $\text{CH}_3\text{NH}_3\text{PbI}_{(3-x)}\text{Cl}_{(x)}$ film morphology with two-step annealing method for efficient hybrid perovskite solar cells,” *ACS Applied Materials & Interfaces*, vol. 7, no. 30, pp. 16330–16337, 2015.
- [37] Y. Yang, S. Feng, M. Li et al., “Annealing induced recrystallization in $\text{CH}_3\text{NH}_3\text{PbI}_{3-x}\text{Cl}_x$ for high performance perovskite solar cells,” *Scientific Reports*, vol. 7, no. 46724, p. 9, 2017.

Research Article

Accurate Maximum Power Point Tracking Algorithm Based on a Photovoltaic Device Model

Lhoussain El Bahir and Touria Hassboun

Laboratory of Electrical Engineering and Control Systems (LGECOS), National School of Applied Sciences, Cadi Ayyad University, Av. Abdelkrim El Khattabi B.P. 575, 40000 Marrakech, Morocco

Correspondence should be addressed to Lhoussain El Bahir; l.elbahir@uca.ma

Received 24 March 2017; Accepted 5 July 2017; Published 10 August 2017

Academic Editor: Urs Aeberhard

Copyright © 2017 Lhoussain El Bahir and Touria Hassboun. This is an open access article distributed under the Creative Commons Attribution License, which permits unrestricted use, distribution, and reproduction in any medium, provided the original work is properly cited.

An accurate method is proposed to track the maximum power point of a photovoltaic module. The method is based on the analytical value of the maximum power point voltage, determined from a mathematical model of the photovoltaic panel. The method has the advantage of accuracy without any oscillations, as with certain conventional methods. The algorithm has also the ability to track accurately the maximum power point under variable atmospheric conditions and load changes. Experimental results are presented to show the effectiveness of the method. The implementation of the method needs an online measurement of irradiance, panel temperature, and panel current and voltage.

1. Introduction

The solar energy is one of the most competitive sources of electrical energy, especially photovoltaic (PV) devices. PV panels are devices that convert solar energy into electricity in a clean way and offer an alternative solution of electric power generation in all industry sectors and domestic applications, particularly in remote areas.

The PV device performances are certainly very attractive but could be influenced by some factors, especially the relative panel orientation to solar rays, measurement equipment, power converters, load and/or grid connection, and the extraction of the maximum electric power. An overall optimization of the system should be performed to achieve the best possible performance. A variety of methods to deal with these aspects has been proposed and studied in the literature [1, 2].

The maximum power point tracking techniques (MPPT) represent one of the most studied subjects in PV systems. Since the MPP varies with the temperature and irradiation levels, these techniques are equipped by specific algorithms to extract the maximum available electric power. The determined maximum power voltage is used as a reference voltage

in the power converter loop. Many strategies to find the MPP are available in the literature for different equipment technologies, variable environmental conditions, complexity, cost, range of effectiveness, convergence speed, and accuracy tracking when irradiation and/or temperature change. An exhaustive review of different MPPT algorithms can be found in [3-6].

The P&O (Perturb and Observe) and the Incremental Conductance algorithms are the most common [7-12]. Their main advantages are the easy implementation, low computational demand, and only the measured voltage and current are required as information about the PV array. But they also have some drawbacks, like oscillations around the MPP in steady-state conditions and poor tracking under rapidly changing irradiation levels. This is due to the fact that the search for maximum power point is related to the choice of the perturbation step. The latter affects the convergence time and the amplitude of the oscillations antagonistically.

The constant voltage (CV) is also a well-known method in which the operating voltage V_{\max} is set to a fixed percentage of the open-circuit voltage V_{oc} . The main problem with this algorithm is that V_{\max} is not always at the fixed percentage of V_{oc} and the energy is wasted when

the circuit is opened to measure V_{oc} [4, 5, 13]. Instead of operating with voltage, one can operate with current to obtain the so-called short-current pulse-based MPPT which is similar to the CV method. The operating current I_{max} is then a fixed percentage of the short-circuit current I_{sc} . Many improved versions of these methods are published in the literature [9, 12].

Look-up table method and Curve-fitting-based MPPT are offline techniques [14]. In the first one, technical data and panel characteristics at different environmental conditions are stored in a memorized table. Then, measured power of the PV panel is compared with those of stored values to track MPP and operating point is shifted to the new maximum power point. Thus, the system requires a large memory capacity to store all necessary data for varying atmospheric conditions. This method is slow and not very accurate [5]. In the second method, the power-voltage characteristic of PV panels is approached by a polynomial function. The MPP voltage is deduced according to the polynomial coefficients. The operating point on the characteristics of the panel is then moved to track the MPP. This approach requires also large memory and large computation time to calculate the polynomial coefficients for different environmental conditions [5, 14].

In the so-called “beta (β) method,” the MPP is approximated using an intermediate variable β which depends on the parameters, the current, and the voltage of the PV panel [3, 5]. The variable β is continuously computed and compared with a constant reference to track MPP. This method gives fast tracking speed during varying atmospheric conditions.

Some methods are based on neural networks and fuzzy logic [3, 11, 15, 16]. The mean advantage is their ability to take into account the nonlinearities without handling nonlinear mathematical models. However, a good user experience on the PV module characteristics is needed.

In this paper, an accurate method is proposed to track the maximum power point of a photovoltaic module. The method is based on a mathematical model of the PV module to compute the theoretical value of the MPP voltage, for an online measured PV current, PV voltage, irradiance, and temperature. The method has the advantage of accuracy without any oscillations, as with some previously mentioned methods. This accuracy depends of course on the accuracy of the model. The MPPT algorithm has also the ability to track, with a fast speed, the maximum power point under variable atmospheric conditions and load changes. Simulation and experimental tests were performed to validate the method.

The rest of the paper is organized as follows. In Section 2, the mathematical model of photovoltaic panel is presented. The proposed theoretical computation of the MPP voltage is introduced in Section 3. The steps of the deduced MPPT algorithm are described in Section 4. Section 5 deals with the implementation of the proposed MPPT method, including the validation of the model, the description of the experimental platform, and finally, the presentation and discussion of the obtained results. The conclusion is given in Section 6.

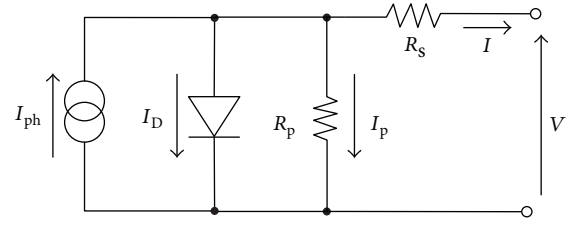


FIGURE 1: Equivalent circuit model of the ideal PV cell.

2. Mathematical Model of Photovoltaic Panel

A photovoltaic cell is an electric power generator. Under solar irradiation, it converts the absorbed photon energy into electrical energy. Depending on the load to which it is connected, the cell can behave as a current generator or a voltage generator. A PV system naturally exhibits nonlinear current-voltage (I - V) characteristic which depends upon the solar irradiation and cell temperature. The single-diode model with the equivalent circuit, as shown in Figure 1, is a simple model that is commonly used because of its practical convenience and the fact that it represents a reasonable compromise between accuracy and simplicity [17].

The circuit comprises a current source in parallel with a diode and a shunt resistor R_p , materializing the leakage current at the junction, and a resistivity grid resistor R_s . The current I_{ph} is generated by the incident light and is directly proportional to the sun irradiation, I_0 is the reverse saturation or leakage current of the diode, and I_D is the Shockley diode current. Based on the circuit of Figure 1, the mathematical model of a photovoltaic cell can be defined in accordance with

$$\begin{aligned} I &= I_{ph} - I_D - I_p \quad \text{with } I_D = I_0(e^{V/aV_t} - 1), \\ I_p &= \frac{V + R_s I}{R_p}, \end{aligned} \quad (1)$$

where $V_t = kT/q$ is the junction thermal voltage, q is the electron charge, k is the Boltzmann constant, T is the temperature of the p - n junction, and a is the diode ideality constant.

The relationship between I and V is given by

$$I = I_{ph} - I_0 \left(e^{(V+R_s I)/aV_t} - 1 \right) - \frac{V + R_s I}{R_p}. \quad (2)$$

The current I_{ph} describes the spectrum of the photovoltaic cell and depends on climatic conditions such as ambient temperature and irradiation G as follows:

$$I_{ph} = \frac{G}{G_r} [I_{scr} - k_i(T - T_r)], \quad (3)$$

where T_r is the reference temperature, I_{scr} is the cell's short-circuit current at T_r , k_i is the temperature coefficient of the short circuit, and G_r is the nominal irradiation.

The diode saturation current I_0 depending on temperature may be expressed by

$$I_0 = I_{or} \left(\frac{T}{T_r} \right)^3 e^{qE_g/Ak((1/T_r)-(1/T))}, \quad (4)$$

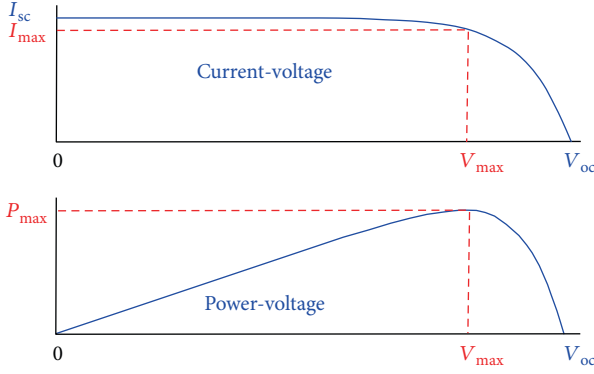


FIGURE 2: Current-voltage (I - V) and power-voltage (P - V) characteristics of a PV module.

where I_{or} is the nominal saturation current and E_g is the band gap energy.

Practical PV array is composed of several interconnected cells. The configuration of the PV array model requires the knowledge of the physical parameters of the panel, which are always provided with reference to the nominal conditions or at standard test conditions of temperature and solar irradiation. The most important parameters widely used for describing the cell electrical performance are the open-circuit voltage V_{oc} , the short-circuit current I_{scr} , the voltage at the maximum power point (MPP) (V_{max}), the current at the MPP (I_{max}), and the maximum experimental peak output power (P_{max}). The rest of parameters could be deduced from the mathematical model equations and the PV technology.

The model of a PV panel with n_p cells in parallel and n_s cells in series can be represented by (6) [17].

Let

$$\begin{aligned} R_{st} &= \frac{n_s}{n_p} R_s, \\ R_{pt} &= \frac{n_s}{n_p} R_p, \\ \xi &= 1 + \frac{R_{st}}{R_{pt}}, \\ \beta &= \frac{1}{V_t a n_s}, \\ h &= (I_{ph} + I_0) n_p. \end{aligned} \quad (5)$$

Then, (1) can be written as

$$\xi I = h - I_0 n_p e^{\beta(V+R_{st}I)} - \frac{V}{R_{pt}}. \quad (6)$$

3. Theoretical Computation of the MPP Voltage

As the PV power is given by $P = IV$, (6) can be rewritten as

$$\xi P = hV - I_0 n_p V e^{\beta(V+R_{st}P/V)} - \frac{V^2}{R_{pt}}. \quad (7)$$

The so known current-voltage (I - V) and power-voltage (P - V) characteristics are represented in Figure 2, for a given temperature T and a given irradiance G .

The maximum power P_{max} of the PV module is obtained for the voltage V_{max} and the current I_{max} . Due to the non-linearity nature of (7), the determination of the analytical expression of the maximum power voltage V_{max} is not obvious by using the standard derivative computation. In the literature, a numerical approach is often used to solve this equation. In this paper, we showed that, by determining the analytical equation of the tangent at each point of the power-voltage (P - V) curve, one can deduce that V_{max} is given by

$$V_{max} = \frac{\beta h (R_{st} - R_{GL}) + \xi - (R_{GL}/R_{pt})}{\beta ((R_{st}/R_{GL}) - 1) (\xi + (R_{GL}/R_{pt}))}, \quad (8)$$

where R_{GL} represents the global load, seen by the PV panel (Figure 3).

Indeed, consider (6) and suppose that we move from a point (I_n, V_n) , for a sampling index n , of the I - V curve to a closely neighboring point (I_{n+1}, V_{n+1}) , indexed by $n+1$, as illustrated in Figure 4, in such way that

$$\begin{aligned} I_{n+1} &= I_n - i, \\ V_{n+1} &= V_n + v, \end{aligned} \quad (9)$$

where i is a very small variation of the current ($i \rightarrow 0$) and v is the corresponding very small variation of the voltage ($v \rightarrow 0$).

From (6), one can write for both points:

$$\begin{aligned} \xi I_n &= h - I_0 n_p e^{\beta(V_n + R_{st} I_n)} - \frac{V_n}{R_{pt}}, \\ \xi I_{n+1} &= h - I_0 n_p e^{\beta(V_{n+1} + R_{st} I_{n+1})} - \frac{V_{n+1}}{R_{pt}}. \end{aligned} \quad (10)$$

By taking into account (9) in the second equation of (10), we have

$$\xi I_n - \xi i = h - I_0 n_p e^{\beta(V_n + R_{st} I_n + v - R_{st} i)} - \frac{V_n + v}{R_{pt}}, \quad (11)$$

and then

$$\xi I_n - \xi i = h - I_0 n_p e^{\beta(V_n + R_{st} I_n)} e^{\beta(v - R_{st} i)} - \frac{V_n + v}{R_{pt}}. \quad (12)$$

Since $i \rightarrow 0$ and $v \rightarrow 0$ as assumed before, we can consider that $\beta(v - R_{st} i) \rightarrow 0$ and then make the following approximation:

$$e^{\beta(v - R_{st} i)} \approx 1 + \beta(v - R_{st} i). \quad (13)$$

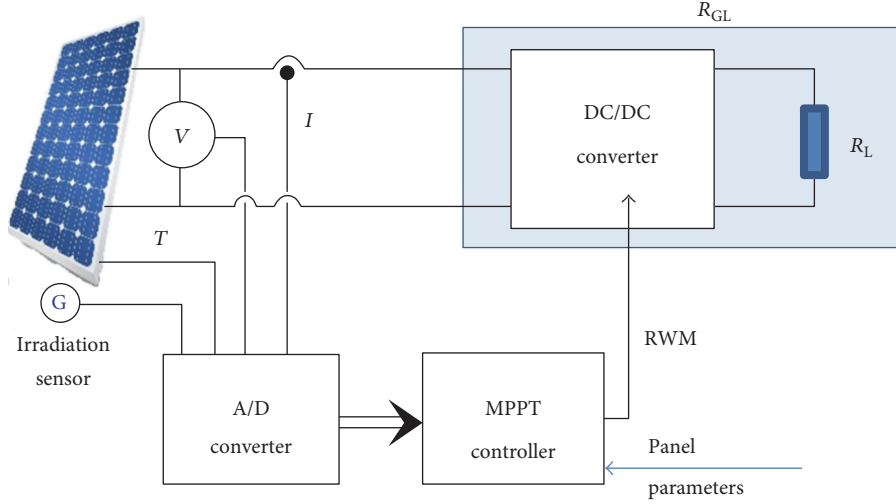


FIGURE 3: PV system with MPPT controller.

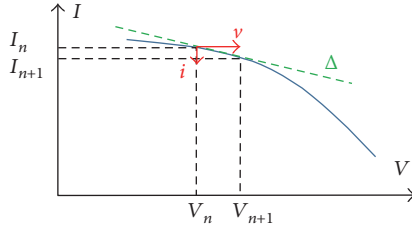
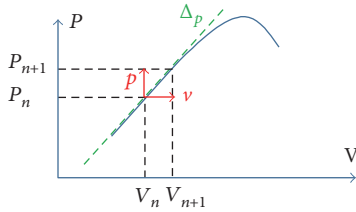
FIGURE 4: I - V curve section.

FIGURE 5: A power-voltage curve section.

Equation (12) can then be approximated as

$$\begin{aligned} \xi I_n - \xi i &= h - I_0 n_p e^{\beta(V_n + R_{st} I_n)} [1 + \beta(v - R_{st} i)] - \frac{V_n + v}{R_{pt}}, \\ \xi I_n - \xi i &= h - I_0 n_p e^{\beta(V_n + R_{st} I_n)} - \frac{V_n}{R_{pt}} \\ &\quad - I_0 n_p e^{\beta(V_n + R_{st} I_n)} \beta(v - R_{st} i) - \frac{v}{R_{pt}}. \end{aligned} \quad (14)$$

Eliminating ξI_n and its equivalent expression leads to

$$\left(\xi + I_0 n_p e^{\beta(V_n + R_{st} I_n)} \beta R_{st} \right) i = \left(I_0 n_p e^{\beta(V_n + R_{st} I_n)} \beta + \frac{1}{R_{pt}} \right) v, \quad (15)$$

and then

$$i = \frac{I_0 n_p e^{\beta(V_n + R_{st} I_n)} \beta + (1/R_{pt})}{\xi + I_0 n_p e^{\beta(V_n + R_{st} I_n)} \beta R_{st}} v. \quad (16)$$

According to (10), $I_0 n_p e^{\beta(V_n + R_{st} I_n)} = -\xi I_n - (V_n/R_{pt}) + h$. This allows us to write (16) as

$$i = \frac{(h - \xi I_n - (V_n/R_{pt})) \beta + (1/R_{pt})}{\xi + (h - \xi I_n - (V_n/R_{pt})) \beta R_{st}} v. \quad (17)$$

This expression seems better, numerically speaking, than (16) which contains an exponential term.

Equation (17) or (16) can be interpreted as the tangent (Δ) to the I - V curve at the point (I_n, V_n) , Figure 4.

Moving from the point (I_n, V_n) to the point (I_{n+1}, V_{n+1}) on the I - V characteristic means also that the power moves from the point (P_n, V_n) to the point (P_{n+1}, V_{n+1}) (Figure 5) so that

$$P_{n+1} = P_n + p, \quad (18)$$

where p is the power variation corresponding to the voltage variation v .

Equation (16) can be written as

$$\begin{aligned} V_{n+1} I_{n+1} &= V_n I_n + p \Rightarrow (V_n + v)(I_n - i) \\ &= V_n I_n + p \Rightarrow v I_n - v i - V_n i = p. \end{aligned} \quad (19)$$

We can consider that iv could be neglected in (19) as $i \rightarrow 0$ and $v \rightarrow 0$. So,

$$p \simeq v I_n - V_n i. \quad (20)$$

Equations (20) and (17) lead to

$$p = \left[I_n - V_n \left(\frac{(h - \xi I_n - (V_n/R_{pt})) \beta + (1/R_{pt})}{\xi + (h - \xi I_n - (V_n/R_{pt})) \beta R_{st}} \right) \right] v, \quad (21)$$

which can be interpreted as the tangent (Δ_p) to the power curve at the point (P_n, V_n) (Figure 5). We can deduce that

when $P_n = P_{\max}$ and $V_n = V_{\max}$, the tangent (Δ_p) becomes horizontal and then $p = 0$, which means that

$$I_{\max} - V_{\max} \left(\frac{\beta h - \beta \xi I_{\max} - (\beta V_{\max}/R_{pt}) + (1/R_{pt})}{\xi + \beta R_{st} h - \beta R_{st} \xi I_{\max} - (\beta R_{st} V_{\max}/R_{pt})} \right) = 0. \quad (22)$$

As $I_{\max} = V_{\max}/R_{GL}$, (22) can easily be rearranged to lead to the result of (8).

One can finally notice that approximations (13) and (20) do not affect the analytical nature of the solution, since i and v are assumed infinitely small.

4. Proposed MPPT Algorithm

In PV systems, the MPPT controller is aimed at computing V_{\max} as a reference voltage and translating it into a PWM command signal to act on the DC/DC converter and adjust the PV voltage to the computed reference voltage value under varying load and weather conditions. The proposed algorithm is based on V_{\max} computed according to (8) and implemented using the following steps at every sampling time:

- (i) measure I , V , G , and T ;
- (ii) compute $R_{GL} = V/I$;
- (iii) compute $h = (I_{ph} + I_0)n_p$;
- (iv) compute V_{\max} with (8);
- (v) compute $e = V - V_{\max}$ and use it as a PI controller input, for example, to generate the command signal which is translated into PWM form to control the DC/DC converter (Figure 3).

By analyzing the steps of this algorithm, the reference voltage V_{\max} is calculated using algebraic formula (7), once the radiation and temperature are measured. This lets us to think that the convergence of the PV voltage towards V_{\max} will not present any oscillations around the latter. Moreover, the convergence time will be mainly linked to the performance of the used controller to eliminate the error between these two voltages. During our tests, we opted for a PI controller for its simplicity. As mentioned before, the accuracy of V_{\max} is limited by the accuracy of the used model, from which formula (8) was deduced. On the other hand, from (8), one can expect that for any variation of irradiation and/or temperature, an appropriate V_{\max} should be generated. Thus, the MPPT algorithm will be able to adapt to climatic conditions. The calculation time will not be considered as an influence factor, since the algorithm does not require any data storage nor a heavy data processing.

5. Implementation of the Method

As mentioned previously, the accuracy of the method is based on the accuracy of the PV model. The mathematical

TABLE 1: SR-20 PV device specifications (A.M.1.5, 1 kW/m², 25°C).

Voltage at MPP	$V_{\max} = 17.2$ V
Current at MPP	$I_{\max} = 1.17$ A
Short-circuit current	$I_{scr} = 1.28$ A
Open circuit voltage	$V_{oc} = 21.6$ V
Maximum power	$P_{\max} = 20$ W
Ideality factor	$A = 1.9$
Charge of 1 electron	$q = 1.6e^{-19}$ C
Boltzmann constant	$k = 1.380658e^{-23}$ J/K
Band gap energy	$E_g = 1.12$ eV
Reverse saturation current at T_r	$I_{or} = 5.98e^{-6}$ A
Short-circuit current generated at T_r	$I_{scr} = 1.28$ A
Temperature coefficient of short-circuit current	$k_i = 512.10e^{-6}$ A/K
Number of cells connected in series	$n_s = 36$
Number of cells connected in parallel	$n_p = 1$
Internal series resistance of a cell	$R_s = 0.004$ Ω
Internal parallel resistance of a cell	$R_p = 1000$ Ω

model of the PV device should then be validated. The PV device we have used is an SR-20 with the specifications in Table 1.

5.1. PV Model Validation. According to the nonlinearity nature of the algebraic equations (6) and (7), we have used the well-known Newton-Raphson numerical method and Matlab software to implement the model. The simulated I - V and P - V characteristics at nominal conditions are shown in Figure 6.

The result shows that the model is able to reproduce the values of the key parameters of the SR-20 PV device, under nominal conditions, such as V_{oc} , I_{scr} , V_{\max} , I_{\max} , and P_{\max} . The model was also validated offline with actual data measured during cloudy periods. The measured irradiance, temperature, and voltage of the panel were stored in a data file to be used as model inputs. The validation test consisted of comparing the measured current with the current provided by the model combined with Newton-Raphson numerical method. The results are shown in the first part of Figure 7. The corresponding measured irradiance, voltage, and temperature are shown in the second, third, and fourth part of Figure 7, respectively.

We can observe that the cloudy periods allowed us to cover a large irradiation interval, between about 200 W/m² and more than 800 W/m². Under this condition, the current provided by the model followed accurately the measured current. The model could then be considered as valid and robust to determine V_{\max} with (8).

5.2. Experimental Setup. The schematic representation of the experimental platform is given in Figure 8. The proposed study has been implemented using a dSpace 1104 board which works with Matlab/Simulink software. It consists of a PV module SR-20 connected to a resistive variable load. The LEM LA55-P current sensor, the LEM LV20-P voltage

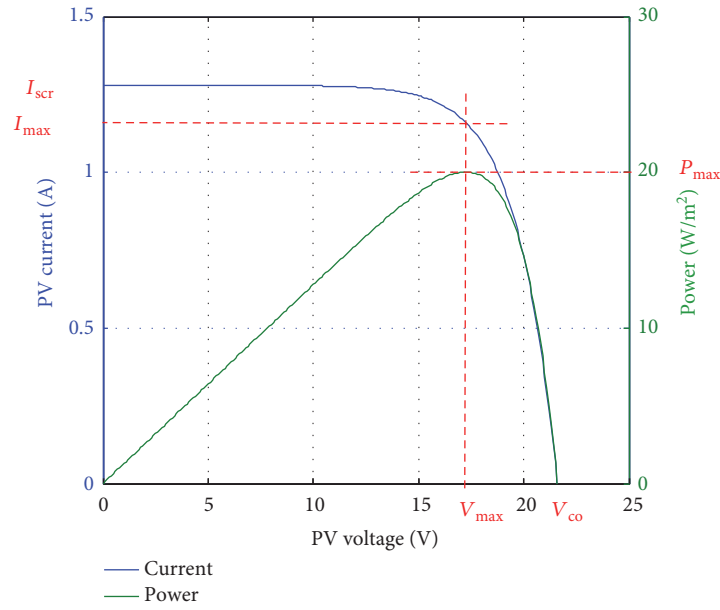


FIGURE 6: Simulated I - V and P - V characteristics of PV device at 1000 W/m^2 , $T = 25^\circ\text{C}$.

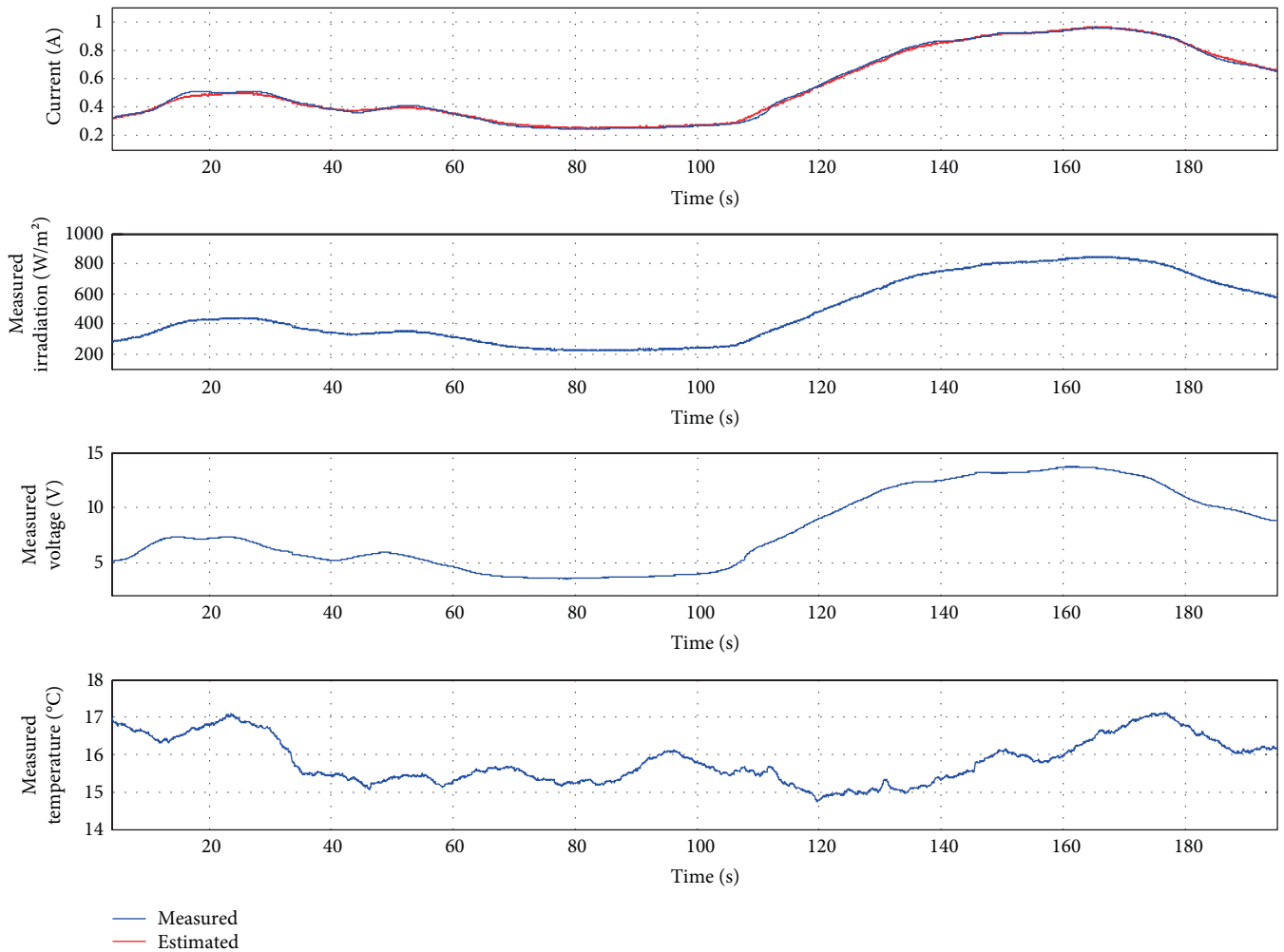


FIGURE 7: Offline validation of the model under natural conditions.

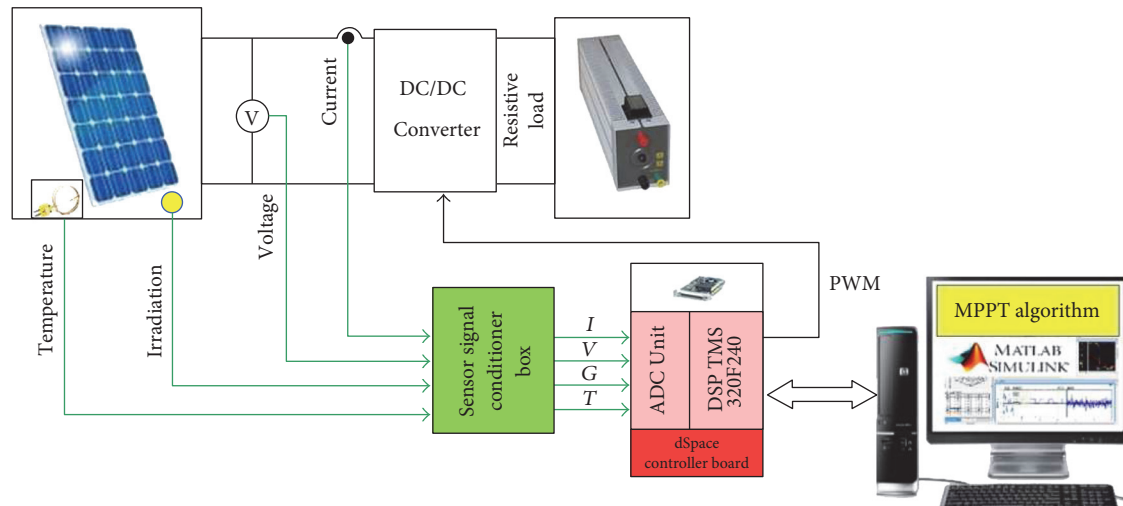


FIGURE 8: Schematic representation of the experimental platform.

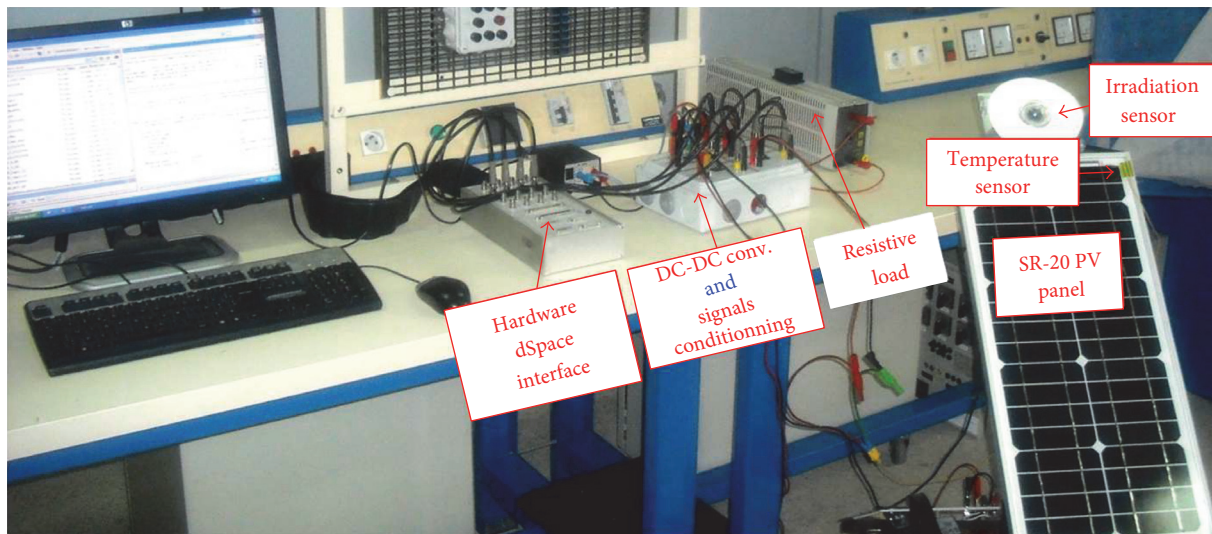


FIGURE 9: Photograph of the experimental setup.

sensor, and the thermocouple temperature sensor (K) are used to measure the current, the voltage, and the temperature of PV module, respectively. All measured signals are conditioned and transformed in the voltage range 0 to ± 10 volts and sent to the dSpace Controller Board. The latter includes an analog-digital converter (ADC), a digital-analog converter (DAC), and a processing system. The dSpace works on Matlab/Simulink platform which is common engineering software. The dSpace boards are associated with Control Desk software, which makes the data acquisition and real-time analysis easy. The dSpace Real-Time Interface (RTI) is based on the Matlab Real-Time Workshop (RTW) to create real-time codes.

The MPPT algorithm is based on a C-S function code which allows a real-time compilation via a Simulink box. The real-time code is loaded on the dSpace board. A real-time handling of data becomes then easily accessible via

the Control Desk software. During the experimental validation, the noisy measured signals are eliminated using a low-pass filter. Figure 9 is a photograph of the designed experimental platform.

5.3. Experimental Results and Discussion. Experimental tests were carried out during alternating sunny and cloudy periods, in Marrakech on June 10, 2016, from 11h30 to 18h30. The PV panel we have used was fixed on a mechanical solar tracker. The same tests could also be done with a fixed panel. Figure 10 shows the measured irradiance and temperature. The cloudy periods were observed at the end of the day.

Very large and abrupt irradiation changes, caused by the cloudy periods, gave rise to a high irradiation variation up to almost 700 W/m^2 . Which is a favourable condition to test the robustness of the algorithm.

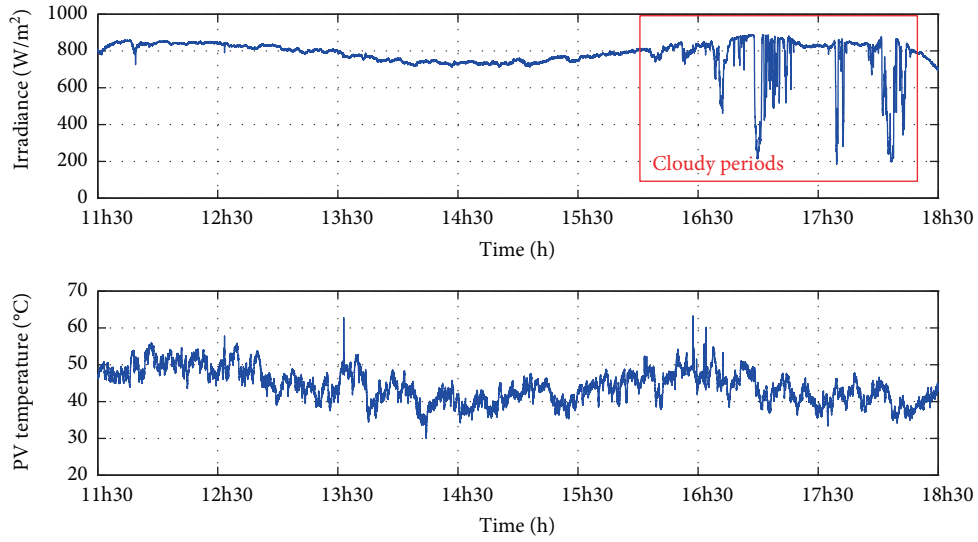


FIGURE 10: Measured irradiance and temperature in Marrakech on June 10, 2016, from 11h30 to 18h30.

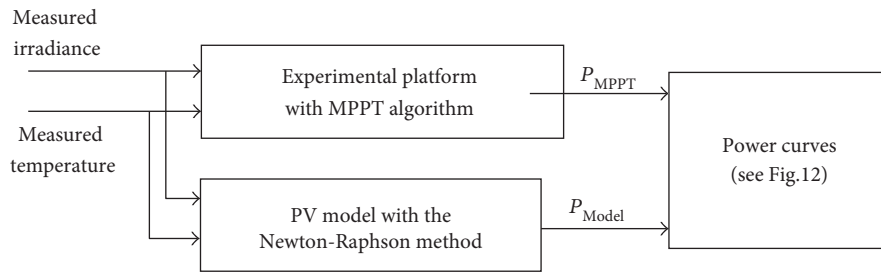


FIGURE 11: Comparison technique of the actual power with the expected one.

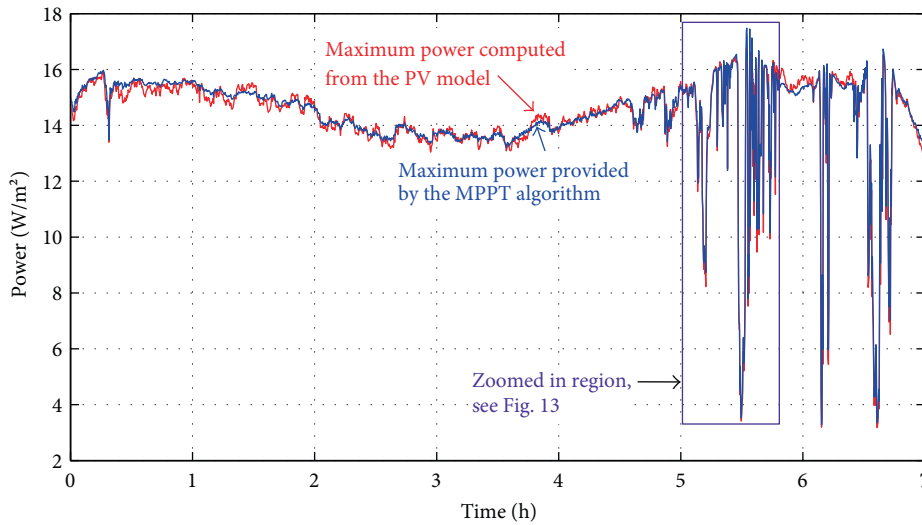


FIGURE 12: Results of the actual power, given by MPPT algorithm, and the power computed using the PV model.

As stipulated in subsection 5.1, the used PV model, combined with the numerical Newton-Raphson method, was able to reproduce with accuracy the behaviour of the PV panel.

The potential maximum power computed from this model was then taken as a reference value. The comparison of the maximum power provided by the proposed MPPT algorithm

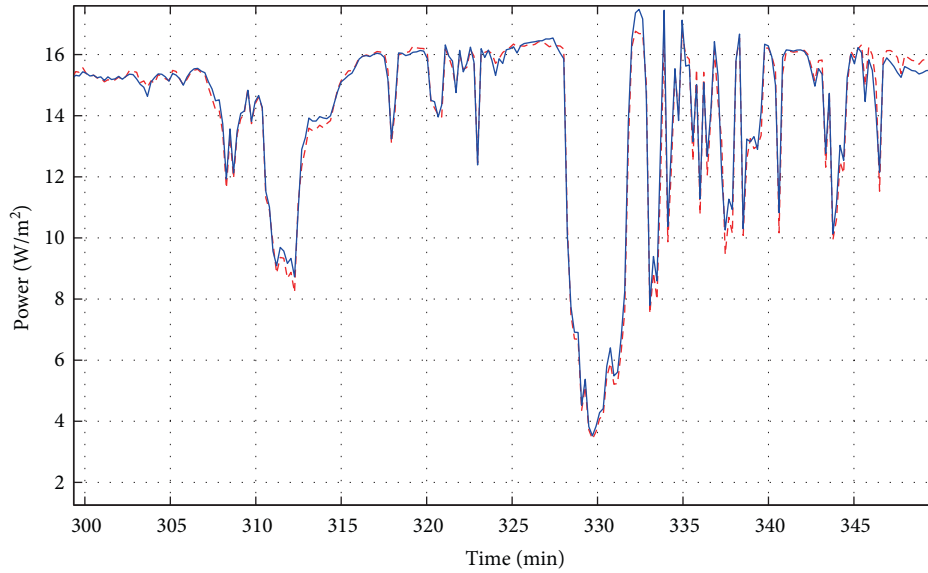


FIGURE 13: Zoom in of the framed part region in Figure 12.

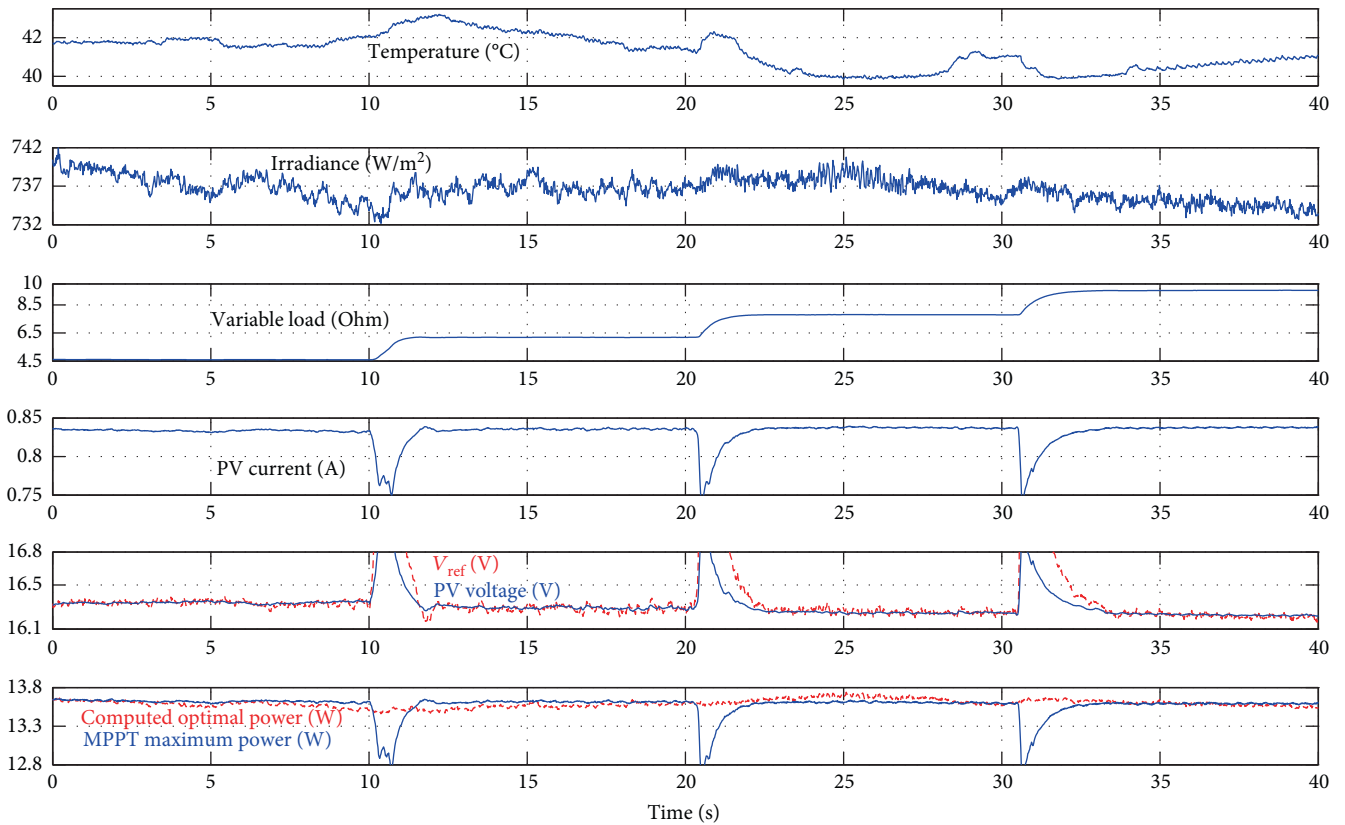


FIGURE 14: MPPT with a resistive variable load.

with this reference value, according to the diagram of Figure 11, is illustrated in Figure 12.

To closely examine the ability of the method to follow the irradiation fluctuations, the framed part in the cloudy period region of Figure 12 is zoomed in Figure 13.

As can be observed, the proposed MPPT algorithm remains fast and robust in extreme changes of irradiation, especially with the abrupt decrease down to 200 W/m^2 .

Since the performance of a PV generator is influenced by the load to which it is connected, it is interesting to test

if the MPPT algorithm is able to maintain the power at its maximum value in spite of load variations. To do so, we have varied the resistive load according to the profile shown in the third part of Figure 14, within a time interval in which the irradiation was relatively constant.

In the last part of Figure 14, the power has indeed been maintained at its maximum value after every short transient (about 3 s) due to abrupt load changes and then the PV current. The observed insignificant accuracy errors are due to PV model accuracy and the acquisition system including cables.

6. Conclusion

The effectiveness of the proposed method has been tested in practice with an experimental platform under realistic conditions, such as cloudy periods and a variable resistive load. The obtained results respond to all expectations formulated in the introduction and in the sections where the principle of the method was introduced.

The MPPT algorithm managed to follow rapidly the variations of the optimum power under a variable resistive load and in the case of abrupt and very significant changes of irradiation. The observed insignificant accuracy errors are due to PV model parameters' tuning and the acquisition system including cables. The last kinds of errors could be eliminated by designing an MPPT controller based on a printed circuit board with a specific DC/DC converter and a microcontroller as a calculator.

However, in addition to current and voltage measurements, the PV temperature and irradiance measurements are also needed. The PV model, on which the method is based, must also be accurate. To reduce instrumentation and maintenance costs, a software estimator of the solar irradiation that we developed in our previous publication could be used [18]. Other implications and limitations should be reported. Indeed, our method has not been tested particularly in the case of large PV areas and PV arrays under partial shading and under certain types of cloud cover. This could be an extension of our future works on this subject.

Conflicts of Interest

The authors declare that they have no conflicts of interest.

References

- [1] N. A. Kelly and T. L. Gibson, "Improved photovoltaic energy output for cloudy conditions with a solar tracking system," *Solar Energy*, vol. 83, no. 11, pp. 2092–2102, 2009.
- [2] A. Zegaoui, M. Aillerie, P. Petit, J. P. Sawicki, J. P. Charles, and A. W. Belarbi, "Dynamic behaviour of PV generator trackers under irradiation and temperature changes," *Solar Energy*, vol. 85, no. 11, pp. 2953–2964, 2011.
- [3] M. A. Eltawil and Z. Zhao, "MPPT techniques for photovoltaic applications," *Renewable and Sustainable Energy Reviews*, vol. 25, pp. 793–813, 2013.
- [4] D. P. Hohm and M. E. Ropp, "Comparative study of maximum power point tracking algorithms," *Progress in Photovoltaics: Research and Applications*, vol. 11, no. 1, pp. 47–62, 2003.
- [5] P. Bhatnagar and R. K. Nema, "Maximum power point tracking control techniques: state-of-the-art in photovoltaic applications," *Renewable and Sustainable Energy Reviews*, vol. 23, pp. 224–241, 2013.
- [6] Z. Salam, J. Ahmed, and B. S. Merugu, "The application of soft computing methods for MPPT of PV system: a technological and status review," *Applied Energy*, vol. 107, pp. 135–148, 2013.
- [7] N. Femia, G. Petrone, G. Spagnuolo, and M. Vitelli, "Optimization of perturb and observe maximum power point tracking method," *IEEE Transactions on Power Electronics*, vol. 20, no. 4, pp. 963–973, 2005.
- [8] F. Liu, S. Duan, F. Liu, B. Liu, and Y. Kang, "A variable step size INC MPPT method for PV systems," *IEEE Transactions on Industrial Electronics*, vol. 55, no. 7, pp. 2622–2628, 2008.
- [9] N. Femia, G. Petrone, G. Spagnuolo, and M. Vitelli, "A technique for improving P&O MPPT performances of double-stage grid-connected photovoltaic systems," *IEEE Transactions on Industrial Electronics*, vol. 56, no. 11, pp. 4473–4482, 2009.
- [10] K. S. Tey and S. Mekhilef, "ScienceDirect modified incremental conductance MPPT algorithm to mitigate inaccurate responses under fast-changing solar irradiation level," *Solar Energy*, vol. 101, pp. 333–342, 2014.
- [11] N. S. D'Souza, L. A. C. Lopes, and X. Liu, "Comparative study of variable size perturbation and observation maximum power point trackers for PV systems," *Electric Power Systems Research*, vol. 80, no. 3, pp. 296–305, 2010.
- [12] Q. Mei, S. Member, M. Shan et al., "A novel improved variable step-size method for PV systems," vol. 58, no. 6, pp. 2427–2434, 2011.
- [13] K. K. Kumar, R. Bhaskar, and H. Koti, "Implementation of MPPT algorithm for solar photovoltaic cell by comparing short-circuit method and incremental conductance method," *Procedia Technology*, vol. 12, pp. 705–715, 2014.
- [14] T. ESRAM and P. L. Chapman, "Comparison of photovoltaic array maximum power point tracking techniques," vol. 22, no. 2, pp. 439–449, 2007.
- [15] F. Chekired, C. Larbes, D. Rekioua, and F. Haddad, "Implementation of a MPPT fuzzy controller for photovoltaic systems on FPGA circuit," *Energy Procedia*, vol. 6, pp. 541–549, 2011.
- [16] O. Guenounou, B. Dahhou, and F. Chabour, "Adaptive fuzzy controller based MPPT for photovoltaic systems," *Energy Conversion and Management*, vol. 78, pp. 843–850, 2014.
- [17] M. G. Villalva, J. R. Gazoli, and E. R. Filho, "Comprehensive approach to modeling and simulation of photovoltaic arrays," *IEEE Transactions on Power Electronics*, vol. 24, no. 5, pp. 1198–1208, 2009.
- [18] T. Hassboun, L. E. Bahir, Y. Aite Driss, and M. E. Adnani, "Solar irradiation estimator based on a self-calibrated reference solar cell," *Turkish Journal of Electrical Engineering and Computer Sciences*, vol. 24, pp. 4885–4899, 2016.

Research Article

Tandem Solar Cells Based on Cu_2O and c-Si Subcells in Parallel Configuration: Numerical Simulation

Mihai Răzvan Mitroi,¹ Valerică Ninulescu,¹ and Laurențiu Fara^{1,2}

¹University POLITEHNICA of Bucharest, 313 Splaiul Independentei, 060042 Bucharest, Romania

²Academy of Romanian Scientists, 54 Splaiul Independentei, 050094 Bucharest, Romania

Correspondence should be addressed to Valerică Ninulescu; ninulescu.valerica@gmail.com

Received 24 April 2017; Revised 16 June 2017; Accepted 6 July 2017; Published 8 August 2017

Academic Editor: Christin David

Copyright © 2017 Mihai Răzvan Mitroi et al. This is an open access article distributed under the Creative Commons Attribution License, which permits unrestricted use, distribution, and reproduction in any medium, provided the original work is properly cited.

A tandem solar cell consisting of a bottom c-Si high-efficiency subcell and a top low-cost Cu_2O subcell in parallel configuration is evaluated for the first time by a use of an electrical model. A numerical simulation based on the single-diode model of the solar cell is performed. The numerical method determines both the model parameters and the parameters of the subcells and tandem from the maximization of output power. The simulations indicate a theoretical limit value of the tandem power conversion efficiency of 31.23% at 298 K. The influence of temperature on the maximum output power is analyzed. This tandem configuration allows a great potential for the development of a new generation of low-cost high-efficiency solar cells.

1. Introduction

Recently, tandem solar cells made up of various materials such as silicon (monocrystalline, polycrystalline, and amorphous) [1–3], perovskite [4–6], polymer [7, 8], dye-sensitized solar cells [9], and quantum dot solar cells [10] have been theoretically or experimentally studied. However, tandems with a high efficiency at low cost have still not been realized. The silicon-based tandem heterojunction solar cells made up of a high-efficiency crystalline silicon (c-Si) bottom subcell and a low-cost upper subcell are a promising candidate for both reducing the fabrication costs and increasing the efficiency above the silicon single-junction record of 25.6% [11]. The band gap of the top subcell is required to be higher than the band gap of silicon (1.1 eV) in order to absorb the photons of higher energy, thus yielding two complementary absorbing subcells. Generally, the bottom subcell generates a higher current and has a lower open-circuit voltage than the top subcell.

The cuprous oxide (Cu_2O) solar cell represents one of the best choices as top subcell. This semiconducting metal oxide has a band gap of 2.1 eV, a high optical

absorption, is nontoxic, and has the potential of a low manufacturing cost [12]. The theoretical limit of the power conversion efficiency for a Cu_2O solar cell is approximately 20% [13, 14] under the solar radiation spectrum AM 1.5G. However, the highest conversion efficiency of 81% achieved experimentally for a solar cell made up of zinc oxide (ZnO) and Cu_2O based on thermally oxidized copper sheets [15] suggests the potential of further increase of the conversion efficiency.

In this paper, a comprehensive numerical simulation of the performance parameters of a tandem solar cell based on c-Si and Cu_2O subcells in parallel configuration is presented. The ideal working conditions for tandem are defined. The single-diode model for solar cells is used [16]. The parameters of the subcells and tandem are calculated from the maximum condition of the output power. The values of the main parameters, that is, the short-circuit current density (J_{sc}), the open-circuit voltage (V_{oc}), the fill factor (FF), and the power conversion efficiency (η), are calculated and discussed. The value of the maximum power conversion efficiency of this configuration type is estimated. The influence of temperature (T) on the performance of the tandem is analyzed.

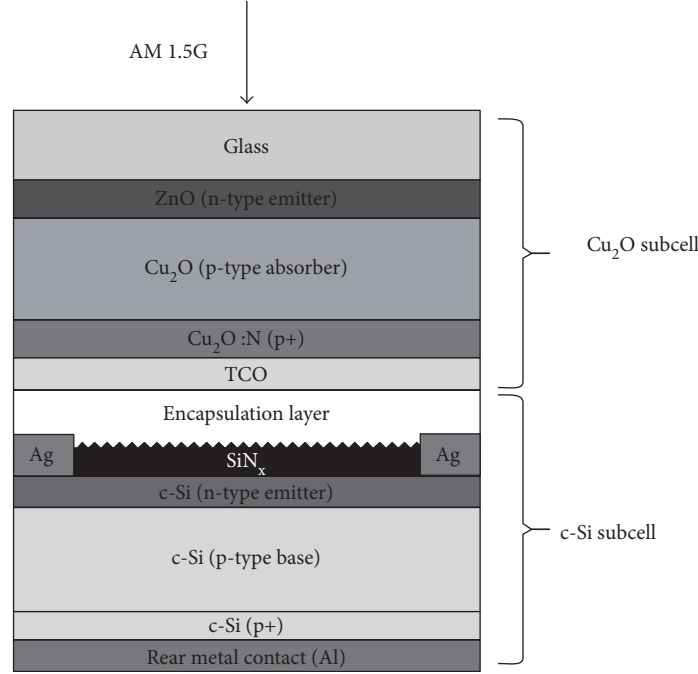


FIGURE 1: Schematic configuration design of a tandem solar cell based on Cu_2O and c-Si subcells.

All the programs used for the simulations are written in Mathcad environment.

2. Theoretical Model

A tandem solar cell based on a bottom c-Si subcell and a top Cu_2O subcell as active layers of p-type materials is investigated. For the Cu_2O subcell, a wide range of possible n-type materials, including ZnO, ZnS, TiO_2 , CdS, and Ga_2O_3 [13–15] can be used. There are two possibilities of electrical connection for the two subcells, namely, series and parallel. The parallel connection is more advantageous [17] since it does not require current matching between the subcells and allows independent optimization of the subcells. A four-terminal device has the subcells electrically decoupled and independently controllable that can be connected in parallel, ensuring a maximum output power at all times [18]. The tandem efficiency is estimated to reach values above 30% [1, 2, 6, 19]. A possible four-terminal configuration is presented in Figure 1 [20].

The following ideal conditions of the solar cell operation—including illumination conditions, subcell materials, radiation absorption processes, and carrier generation processes in subcells—are considered:

- (1) the solar radiation spectrum AM 1.5G [21];
- (2) no optical losses due to nonactive layers (glass, n-type materials, encapsulation layer, etc.);
- (3) the carrier-injection efficiency $\eta_{\text{inj}} = 1$ for each subcell;
- (4) no resistive and recombination losses, $R_s = 0$, for each subcell;

- (5) the standard temperature $T^* = 298$ K.

2.1. Optical Model. In the conditions above, the photoelectron generation rate determined by the solar radiation incident on the surface of the active layer is

$$G_{\text{inj}}(L) = \int_{\lambda_1}^{\lambda_2} \alpha(\lambda) \phi(\lambda) \exp[-\alpha(\lambda)L] d\lambda, \quad (1)$$

where L is the thickness of the active layer (Cu_2O or c-Si), λ is the wavelength of incident radiation, the integration limits λ_1 and λ_2 are imposed by the absorption characteristics of the active layer through the absorption coefficient $\alpha(\lambda)$, and $\phi(\lambda)$ is the spectral incident photon flux density. The photoelectrons are then collected without any losses.

Note that there is a range of wavelengths in which both Cu_2O and c-Si absorb radiation. The incident radiation on the top surface of the Cu_2O layer is the entire AM 1.5G solar spectrum; at the top of the c-Si layer, the spectral irradiance of the AM 1.5G solar spectrum is diminished due to the partial absorption of Cu_2O layer. These lead to the possibility of optimization in choosing the thickness of the two layers so that the output power of tandem cell is at maximum.

2.2. Electrical Model. The current density J through each subcell, in the single-diode model [16], is

$$J = J_L - J_0 \left[\exp\left(\frac{V + R_s J}{\gamma V_{\text{th}}}\right) - 1 \right] - \frac{V + R_s J}{R_{\text{sh}}}, \quad (2)$$

where J_L is the light-generated current density, J_0 is the reverse saturation current density of the diode, V is the

output voltage, γ is the ideality factor, R_s is the series resistance, R_{sh} is the shunt resistance, and $V_{th} = k_B T/q$ is the thermal voltage, where k_B and q denote the Boltzmann constant and elementary electric charge, respectively. In the conditions above, (2) becomes

$$J_{ideal} = J_L - J_0 \left[\exp\left(\frac{V}{\gamma V_{th}}\right) - 1 \right] - \frac{V}{R_{sh}}. \quad (3)$$

In the approximation of a negligible diffusion of carriers and assuming a uniform field across the active layer (subcell materials are without any defects and impurities), the light-generated current density is [22]

$$J_L = qG_{inj}(L)\mu\tau \frac{V_{bi} - V}{L} \left\{ 1 - \exp\left[-\frac{L^2}{\mu\tau(V_{bi} - V)}\right] \right\}, \quad (4)$$

where V_{bi} is the built-in voltage [23] and the product $\mu\tau$ is given by the relation

$$\mu\tau = \mu_p\tau_p + \mu_n\tau_n, \quad (5)$$

where μ_p , μ_n and τ_p , τ_n are the hole and electron mobilities and lifetimes, respectively.

By use of (3) and (4), the output power density of the solar cell is

$$P = \left\{ qG_{inj}(L)\mu\tau \frac{V_{bi} - V}{L} \left[1 - \exp\left(-\frac{L^2}{\mu\tau(V_{bi} - V)}\right) \right] - J_0 \left[\exp\left(\frac{V}{\gamma V_{th}}\right) - 1 \right] - \frac{V}{R_{sh}} \right\} V. \quad (6)$$

One can observe that, at a given temperature, P depends on seven parameters: L , J_0 , V , R_{sh} , γ , $\mu\tau$, and V_{bi} .

In the following, the two subcells will be considered electrically connected in parallel. In the steady state, the current densities and voltages obey the relations

$$J_{tandem} = J_{top} + J_{bottom} \quad (7)$$

and

$$V_{tandem} = V_{top} = V_{bottom}. \quad (8)$$

2.3. The Influence of Temperature on Tandem Cell Performance. The solar cells for usual applications are used at temperatures ranging from -15°C to 100°C . Many studies have pointed out that the performance of solar cells degrades as temperature increases [24–28]. The variation of R_{sh} with temperature slightly affects the efficiency of a solar cell [27, 28]. We analyze the variation with temperature of parameters V_{th} and J_0 .

The thermal voltage dependence on temperature is

$$V_{th}(T) = \frac{k_B T}{q} = V_{th}^* \frac{T}{T^*}, \quad (9)$$

where V_{th}^* is the thermal voltage for the standard temperature.

The dependence on temperature of the reverse bias saturation current density J_0 is [25]

TABLE 1: Single-diode model parameter values of the Cu_2O and c-Si ideal cells.

Cell	R_{sh} ($\Omega \text{ cm}^2$)	γ	J_0 (pA/cm^2)	$\mu\tau$ (cm^2/V)	V_{bi} (V)
Cu_2O	5000	3.00	1.0	$5.00 \cdot 10^{-5}$	1.91
c-Si	6500	1.68	2.3	$1.55 \cdot 10^{-2}$	1.16

TABLE 2: Cell parameters calculated for the values from Table 1.

Cell	J_{sc} (mA/cm^2)	V_{oc} (V)	FF (%)	η (%)
Cu_2O	13.38	1.835	78.51	19.29
c-Si	37.76	1.014	81.70	31.29

$$J_0(T) = J_0^* \left(\frac{T}{T^*}\right)^3 \exp\left[\frac{E_g(T)}{k_B} \left(\frac{1}{T^*} - \frac{1}{T}\right)\right], \quad (10)$$

where $J_0^* = J_0|_{T=T^*}$ and $E_g(T)$ is the band gap energy of the semiconductor (the active layer) which depends on temperature by the relationship [26]

$$E_g(T) = E_g(0) - \frac{\alpha T^2}{T + \beta}, \quad (11)$$

where $E_g(0)$ is the band gap value at $T \approx 0 \text{ K}$, and α and β are constants.

3. Results and Discussion

The operation of a tandem solar cell with a Cu_2O top subcell and a c-Si bottom subcell is simulated using the presented theoretical model. The performance of the tandem is obtained by numerical simulations in the conditions stated in Section 2. The solar radiation spectrum AM 1.5G has values between the wavelength limits 280 nm and 4000 nm and a flux power density of 1000 W/m^2 . The active layers of c-Si and Cu_2O have the absorption wavelength range ([280 nm, 1450 nm] [29] and [280 nm, 640 nm] [30], resp.).

The parameters R_{sh} , γ , J_0 , $\mu\tau$, and V_{bi} of the single-diode model are material constants that depend on materials and the manufacturing of cells. Therefore, the calculated parameters of the c-Si and Cu_2O cells remain unchanged in the tandem configuration. These parameters can be calculated by different methods, such as fitting methods [31, 32], Lambert-W function [33], and asymptotic approximation [34] by use of J - V experimental data.

The method used in this paper was previously applied to the study of solar cells containing a heterojunction with Cu_2O [14]. The method consists in the maximization of the output power density (7) which leads to the parameter values of the theoretical model. The obtained values, separately for the Cu_2O and c-Si cells, are presented in Table 1. The cell voltages are 1.61 V and 0.88 V, respectively, and the thickness of the active layers is $11.94 \mu\text{m}$ and $115.00 \mu\text{m}$, respectively. The cell parameters calculated based on the values of Table 1 are shown in Table 2. The results indicate a maximum power conversion efficiency of 19.29% for the Cu_2O cell of $11.94 \mu\text{m}$ active layer thickness and 31.29% for the c-Si cell of $115.00 \mu\text{m}$ active layer thickness. The maximum

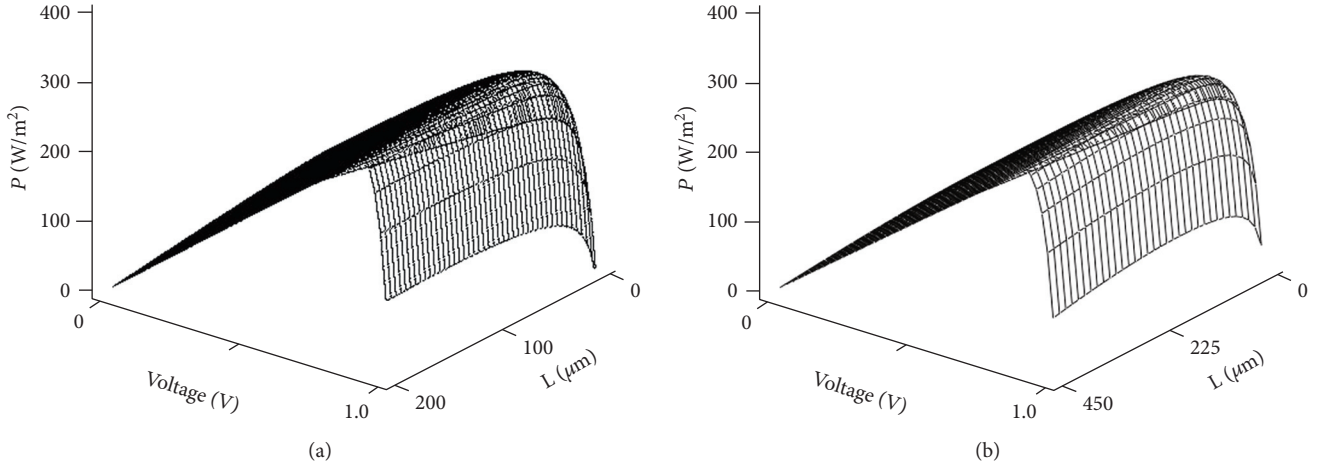


FIGURE 2: The output power density of a tandem cell versus voltage and the total thickness of the active layers for two ratios of subcell thickness: (a) $L_{\text{Cu}_2\text{O}}/L_{\text{c-Si}} = 1/40$ and (b) $L_{\text{Cu}_2\text{O}}/L_{\text{c-Si}} = 1/100$.

TABLE 3: The parameter values of the Cu_2O and c-Si subcells and the tandem in the case of maximum output power density of the tandem cell.

Cell	L (μm)	J_{sc} (mA/cm^2)	V_{oc} (V)	FF (%)	η (%)
Cu_2O top subcell	0.64	10.19	—	—	8.78
c-Si bottom subcell	60.62	27.34	—	—	22.45
Tandem cell	—	37.53	1.015	82.02	31.23

values of the power conversion efficiency are in good agreement with the data reported in literature, $\sim 20\%$ for the Cu_2O cell [13, 14] and 32.9% [35], 29.8% [36], or 33.5% [5] for the c-Si cell.

The dependence of the tandem output power density, (6) where J_{ideal} is J_{tandem} , on the voltage and the total thickness of the active layers (Cu_2O and c-Si layers) is analyzed. The results for two ratios of the thicknesses of the active layers, $L_{\text{Cu}_2\text{O}}/L_{\text{c-Si}} = 1/40$ and $L_{\text{Cu}_2\text{O}}/L_{\text{c-Si}} = 1/100$, are shown in Figure 2. They show a maximum of the tandem output power density. The output power density of tandem as a function of voltage, and the thickness of the two active layers $L_{\text{Cu}_2\text{O}}$ and $L_{\text{c-Si}}$ has been maximized. The calculated parameters for the two subcells and tandem are presented in Table 3. The obtained maximum output power density is $312.3 \text{ W}/\text{m}^2$ for 0.88 V tandem voltage, $0.64 \mu\text{m}$ Cu_2O layer thickness, and $60.62 \mu\text{m}$ c-Si thickness. Therefore, the maximum power conversion efficiency is 31.23% . It can be noticed that in case of tandem, the thickness of the subcells is significantly reduced compared to the case of separate cells (see Table 2). In case of the c-Si and Cu_2O layer thicknesses obtained above, the J - V curves for the two subcells, as well as for the tandem cell, are presented in Figure 3. The open-circuit voltage of the tandem cell (see Table 3) is located between the V_{oc} values of separate subcells (see Table 2), practically being equal to that of the separate c-Si subcell. There is a limitation in the voltage for tandem operation, but this drawback is compensated by the advantages of

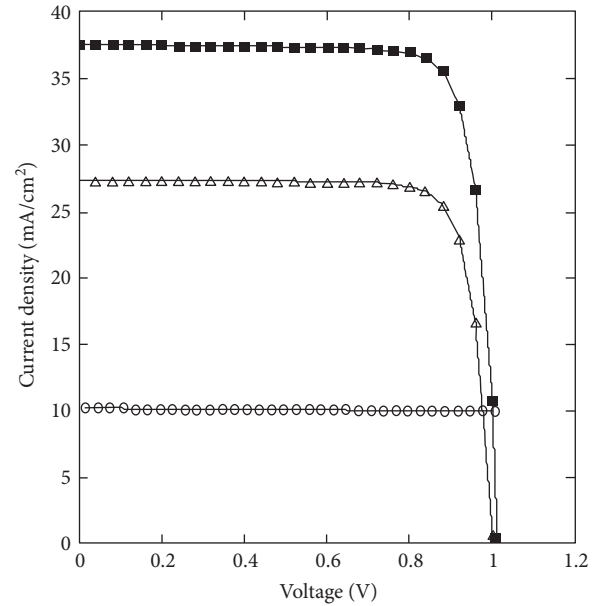


FIGURE 3: Current density versus voltage for the two subcells in tandem and tandem cell, for the thicknesses $0.64 \mu\text{m}$ and $60.62 \mu\text{m}$ of the Cu_2O layer and the c-Si layer, respectively: $J_{\text{Cu}_2\text{O}}$ (\circ), $J_{\text{c-Si}}$ (Δ), and J_{tandem} (\blacksquare).

parallel connection [18]. These results are consistent with theoretical or experimental values reported in literature for other types of tandem cells [5, 7, 8, 37].

Figure 4 shows the dependence of the maximum output power density on temperature for the thickness of active layers from Table 3 and for the following parameter values of (11): $E_{g,\text{Cu}_2\text{O}}(0) = 2.173 \text{ eV}$, $\alpha_{\text{Cu}_2\text{O}} = 4.8 \cdot 10^{-4} \text{ eV}/\text{K}$, $\beta_{\text{Cu}_2\text{O}} = 275 \text{ K}$ [38], $E_{g,\text{c-Si}}(0) = 1.1557 \text{ eV}$, $\alpha_{\text{c-Si}} = 7.021 \cdot 10^{-4} \text{ eV}/\text{K}$, and $\beta_{\text{c-Si}} = 1108 \text{ K}$ [26]. A decrease of the maximum output power density with increasing temperature is observed. This decrease is due to the temperature dependence of the reverse bias saturation current density (10). The drop

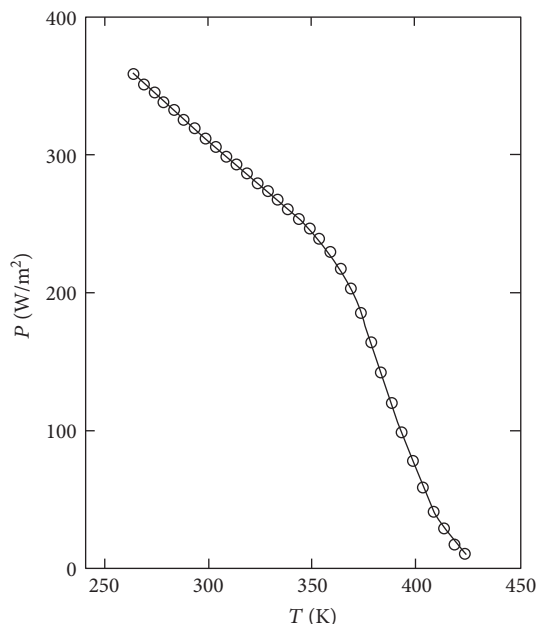


FIGURE 4: The maximum output power density of the tandem cell versus temperature, for the thicknesses $0.64\ \mu\text{m}$ and $60.62\ \mu\text{m}$ of Cu_2O layer and c-Si layer, respectively.

of the output power density is 20.90% for a temperature increase from 298 K to 348 K. This result indicates that the temperature is a major factor in decreasing the tandem solar cell performance.

4. Summary and Concluding Remarks

The paper presents a comprehensive numerical simulation of performance optimization of the tandem solar cells using c-Si and Cu_2O subcells. A numerical simulation based on the single-diode model of the solar cell is performed. The numerical method determines both the model parameters and the parameters of the subcells and tandem.

The thickness of active layers c-Si and Cu_2O in tandem cell is obtained from the maximization of output power. The tandem power conversion efficiency has a maximum of 31.23% for a $0.64\ \mu\text{m}$ Cu_2O layer thickness and $60.62\ \mu\text{m}$ c-Si layer thickness. These thicknesses are significantly reduced compared to the case of separate cells, and the efficiency represents the theoretical limit at 298 K. A realistic model of the tandem will include optical losses for each layer of the tandem as well as a smaller than unity injection efficiency in the active layers. Therefore, a lower value of the tandem efficiency is expected. The numerical simulation shows that temperature is a factor in decreasing tandem cell performance; therefore, temperature should be taken into account in tandem design.

The results of this paper give indications for the design and performance optimization of real tandem solar cells using Cu_2O and c-Si subcells.

An approach of the solar cell tandem using experimental data will be the subject of future research.

Conflicts of Interest

The authors declare that there is no conflict of interest regarding the publication of this paper.

Acknowledgments

This work was supported by (1) the project MultiscaleSolar MP1406, 2015–2019, supported by the European Commission through COST program (the article processing charges), and (2) the project SOLHET, 2016–2019, M-ERA.Net program, supported by the Research Council of Norway (RCN) and the Romanian Executive Agency for Higher Education, Research, Development and Innovation Funding (UEFISCDI).

References

- [1] T. P. White, N. N. Lal, and K. R. Catchpole, "Tandem solar cells based on high-efficiency c-Si bottom cells: top cell requirements for >30% efficiency," *IEEE Journal of Photovoltaics*, vol. 4, no. 1, pp. 208–214, 2014.
- [2] C. Ulbrich, C. Zahren, A. Gerber et al., "Matching of silicon thin-film tandem solar cells for maximum power output," *International Journal of Photoenergy*, vol. 2013, Article ID 314097, 7 pages, 2013.
- [3] M. Taguchi, A. Yano, S. Tohoda et al., "24.7% record efficiency HIT solar cell on thin silicon wafer," *IEEE Journal of Photovoltaics*, vol. 4, pp. 96–99, 2014.
- [4] P. Löper, S.-J. Moon, S. M. d. Nicolas et al., "Organic-inorganic halide perovskite/crystalline silicon four-terminal tandem solar cells," *Physical Chemistry Chemical Physics*, vol. 17, p. 1619, 2015.
- [5] H. M. Futscher and B. Ehrler, "Efficiency limit of perovskite/Si tandem solar cells," *ACS Energy Letters*, vol. 1, no. 4, pp. 863–868, 2016.
- [6] R. Asadpour, R. V. K. Chavali, M. R. Khan, and M. A. Alam, "Bifacial Si heterojunction-perovskite organic-inorganic tandem to produce highly efficient ($\eta T^* \sim 33\%$) solar cell," *Applied Physics Letters*, vol. 106, article 243902, 2015.
- [7] A. Hadipour, B. d. Boer, and P. W. M. Blom, "Device operation of organic tandem solar cells," *Organic Electronics*, vol. 9, pp. 617–624, 2008.
- [8] L. Yang, H. Zhou, S. C. Price, and W. You, "Parallel-like bulk heterojunction polymer solar cells," *Journal of the American Chemical Society*, vol. 134, pp. 5432–5435, 2012.
- [9] A. K. Baranwal, T. Shiki, Y. Ogomi, S. S. Pandey, T. Ma, and S. Hayase, "Tandem dye-sensitized solar cells with a back-contact bottom electrode without a transparent conductive layer," *RSC Advances*, vol. 4, pp. 47735–47742, 2014.
- [10] S. Diao, X. Zhang, Z. Shao, K. Ding, J. Jie, and X. Zhang, "12.35% efficient graphene quantum dots/silicon heterojunction solar cells using graphene transparent electrode," *Nano Energy*, vol. 31, pp. 359–366, 2017.
- [11] K. Masuko, M. Shigematsu, T. Hashiguchi et al., "Achievement of more than 25% conversion efficiency with crystalline silicon heterojunction solar cell," *IEEE Journal of Photovoltaics*, vol. 4, pp. 1433–1435, 2014.
- [12] B. K. Meyer, A. Polity, D. Reppin et al., "The physics of copper oxide (Cu_2O)," *Chapter 6: Semiconductors and Semimetals*, vol. 88, pp. 201–226, 2013.

- [13] Y. Takiguchi and S. Miyajima, "Device simulation of cuprous oxide heterojunction solar cells," *Japanese Journal of Applied Physics*, vol. 54, no. 11, article 112303, 2015.
- [14] M. R. Mitroi, V. Ninulescu, and L. Fara, "Performance optimization of solar cells based on heterojunctions with Cu_2O -numerical analysis," *Journal of Energy Engineering*, pp. 1943–7897, 2017.
- [15] T. Minami, Y. Nishi, and T. Miyata, "Efficiency enhancement using a $\text{Zn}_{1-x}\text{Ge}_x\text{-O}$ thin film as an n-type window layer in Cu_2O -based heterojunction solar cells," *Applied Physics Express*, vol. 9, article 052301, 2016.
- [16] K. Ishibashi, Y. Kimura, and M. Niwano, "An extensively valid and stable method for derivation of all parameters of a solar cell from a single current-voltage characteristic," *Journal of Applied Physics*, vol. 103, article 094507, 2008.
- [17] Y. Hamakawa, Ed., *Thin-Film Solar Cells: Next Generation Photovoltaics and Its Applications*, Berlin, Springer, 2004.
- [18] S. Reynolds and V. Smirnov, "Modelling performance of two- and four-terminal thin-film silicon tandem solar cells under varying spectral conditions," *Energy Procedia*, vol. 84, pp. 251–260, 2015.
- [19] R. E. Brandt, M. Young, H. H. Park et al., "Band offsets of n-type electron-selective contacts on cuprous oxide (Cu_2O) for photovoltaics," *Applied Physics Letters*, vol. 105, no. 26, article 263901, 2014.
- [20] Ø. Nordseth, R. Kumar, K. Bergum et al., "Optical analysis of a $\text{ZnO}/\text{Cu}_2\text{O}$ subcell in a silicon-based tandem heterojunction solar cell," *Green and Sustainable Chemistry*, vol. 7, pp. 57–69, 2017.
- [21] ASTM G173-03, "Reference spectra derived from SMARTS v. 2.9.2," 2012, March, 2017, <http://rredc.nrel.gov/solar/spectra/am1.5/ASTMG173/ASTMG173.html>.
- [22] T. Aernouts, *Organic Bulk Heterojunction Solar Cells: From Single Cell towards Fully Flexible Photovoltaic Module*, [Ph.D. Thesis], Departement Natuurkunde, Faculteit Wetenschappen, Katholieke Universiteit Leuven, Belgium, 2006, March 2017, <https://lirias.kuleuven.be/bitstream/1979/402/5/PhD>.
- [23] X. Chao, Y. Ruo-He, and G. Kui-Wei, "Photovoltage analysis of a heterojunction solar cell," *Chinese Physics B*, vol. 20, no. 5, article 057302, 2011.
- [24] M. Abderrezek, M. Fathi, S. Mekhilef, and F. Djahli, "Effect of temperature on the GaInP/GaAs tandem solar cell performances," *International Journal of Renewable and Sustainable Energy*, vol. 5, no. 2, pp. 629–634, 2015.
- [25] P. Singh and N. M. Ravindra, "Temperature dependence of solar cell performance—an analysis," *Solar Energy Materials and Solar Cells*, vol. 101, pp. 36–45, 2012.
- [26] Y. P. Varshni, "Temperature dependence of the energy gap in semiconductors," *Physica*, vol. 34, pp. 149–154, 1967.
- [27] F. Attivissimo, A. D. Nisio, M. Savino, and M. Spadavecchia, "Uncertainty analysis in photovoltaic cell parameter estimation," *IEEE Transactions on Instrumentation and Measurement*, vol. 61, no. 5, pp. 1334–1342, 2012.
- [28] P. Singh, S. N. Singh, and M. LalM. Husain, "Temperature dependence of I - V characteristics and performance parameters of silicon solar cell," *Solar Energy Materials and Solar Cells*, vol. 92, pp. 1611–1616, 2008.
- [29] M. A. Green, "Self-consistent optical parameters of intrinsic silicon at 300K including temperature coefficients," *Solar Energy Materials and Solar Cells*, vol. 92, no. 11, pp. 1305–1310, 2008.
- [30] C. Malerba, F. Biccari, C. L. A. Ricardo, M. D'Incau, P. Scardi, and A. Mittiga, "Absorption coefficient of bulk and thin film Cu_2O ," *Solar Energy Materials and Solar Cells*, vol. 95, no. 10, pp. 2848–2854, 2011.
- [31] M. R. Mitroi, V. Iancu, L. Fara, and M. L. Ciurea, "Numerical analysis of J - V characteristics of a polymer solar cell," *Progress in Photovoltaics: Research and Applications*, vol. 19, no. 3, pp. 253–377, 2011.
- [32] R. S. AbdelHady, "Detecting the parameters of solar cells using efficient curve fitting techniques," *International Journal of Engineering Research and Technology*, vol. 7, no. 3, pp. 185–199, 2014.
- [33] J. Cubas, S. Pindado, and C. d. Manuel, "Explicit expressions for solar panel equivalent circuit parameters based on analytical formulation and the Lambert W -function," *Energies*, vol. 7, pp. 4098–4115, 2014.
- [34] A. Bărar, D. Mănăilă-Maximean, O. Dănilă, and M. Vlădescu, "Parameter extraction of an organic solar cell using asymptotic estimation and Lambert W function," in *Proceedings SPIE 10010, Advanced Topics in Optoelectronics, Microelectronics, and Nanotechnologies VIII*, Article ID 1001034, 2016.
- [35] R. Matson, R. Bird, and K. Emery, "Terrestrial solar spectra, solar simulation and solar cell efficiency measurement," Tech. Rept. SERI/TR-612-964: DE82002082, U.S. Department of Energy, ON, 1981.
- [36] T. Tiedje, E. Yablonovitch, G. D. Cody, and B. G. Brooks, "Limiting efficiency of silicon solar cells," *IEEE Transactions on Electron Devices*, vol. ED-31, no. 5, 1984.
- [37] D. Zhanga, W. Soppea, and R. E. I. Schroppa, "Design of 4-terminal solar modules combining thin-film wide-bandgap top cells and c-Si bottom cells," *Energy Procedia*, vol. 77, pp. 500–507, 2015.
- [38] F. Biccari, *Defects and Doping in Cu_2O* , [Ph.D. Thesis], Università di Roma, Italia, 2009, March 2017, http://www.phys.uniroma1.it/fisica/sites/default/files/DOTT_FISICA/MENU/03DOTTORANDI/TesiFin22/Biccari.pdf.

Research Article

Modeling and Modulation of NNPC Four-Level Inverter for Solar Photovoltaic Power Plant

Xiaoqiang Guo,¹ Xuehui Wang,¹ Ran He,¹ and Mehdi Narimani²

¹Department of Electrical Engineering, Yanshan University, Qinhuangdao, China

²Department of Electrical and Computer Engineering, McMaster University, Hamilton, ON, Canada

Correspondence should be addressed to Xiaoqiang Guo; yeduming@163.com

Received 17 January 2017; Accepted 8 May 2017; Published 30 July 2017

Academic Editor: Matthias Auf der Maur

Copyright © 2017 Xiaoqiang Guo et al. This is an open access article distributed under the Creative Commons Attribution License, which permits unrestricted use, distribution, and reproduction in any medium, provided the original work is properly cited.

Photovoltaic (PV) power plant is an attractive way of utilizing the solar energy. For high-power PV power plant, the multilevel inverter is of potential interest. In contrast to the neutral-point clamped (NPC) or flying capacitor (FC) multilevel inverter, the nested neutral point clamped (NNPC) four-level inverter has better features for solar photovoltaic power plant. In practical applications, the common mode voltage reduction of the NNPC four-level is one of the important issues. In order to solve the problem, a new modulation strategy is proposed to minimize the common mode voltage. Compared with the conventional solution, our proposal can reduce the common mode voltage to 1/18 of the DC bus voltage. Moreover, it has the capability to balance the capacitor voltages. Finally, we carried out time-domain simulations to test the performance of the NNPC four-level inverter.

1. Introduction

In recent years, the grid-connected wind and PV power systems have attracted considerable interests around the world [1–4]. Many industrialized nations have installed significant solar power capacity into their electrical grids, providing an alternative to conventional energy sources. While an increasing number of less developed nations have turned to solar to reduce dependence on expensive imported fuels. Different from most building-mounted and other domestic solar power applications which are mainly for the low-voltage local users [5, 6], the high voltage is necessary to integrate the solar photovoltaic power plant into utility. In this case, the multilevel inverters are of potential interest for PV plants [7–11]. In practice, however, there are leakage currents and EMC issues in high-power photovoltaic plants [12]. The leakage currents and electromagnetic interferences have potential safety problems [13, 14]. Therefore, it must be eliminated before connecting them into grid. For this aim, the solutions based on the interesting topologies and modulation strategies have been developed in recent years. Typically, there are three classical topologies of the multilevel inverters such as the flying capacitor (FC) topology, cascade H-bridge

topology, and neutral point clamped (NPC) topology [15–18]. Compared with the conventional two-level inverter, the multilevel inverter has unique features such as reduced voltage stress, less dv/dt and high waveforms. In contrast to the existing topologies, a novel nested neutral point clamped (NNPC) inverter is proposed in [19], it is of great interest for medium-voltage power conversion, especially for solar PV plant applications. In practice, however, the common mode voltage may arise, resulting in the leakage current. In order to solve the problem, a new modulation strategy is proposed to minimize the common mode voltage. Compared with the conventional solution, our proposal can reduce the common mode voltage to 1/18 of the DC bus voltage. Meanwhile, it has the capacitor balancing capability. Finally, the time-domain performance tests are carried out. The results verify the effectiveness of the proposed solution.

2. Analysis of Four-Level NNPC Inverter

The schematic diagram of the novel four-level NNPC inverter is illustrated in Figure 1, where each phase includes 6 switches, 2 diodes, and 2 flying capacitors, which has fewer number of components and complexity than four-level NPC

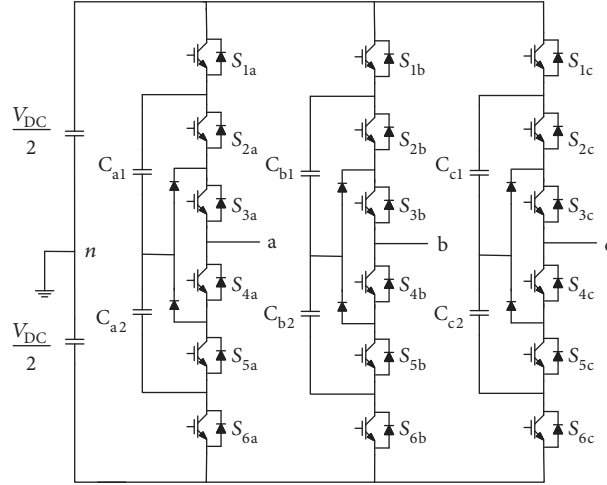


FIGURE 1: Schematic diagram of the four-level NNPC inverter.

TABLE 1: States, switching states, and flying capacitors voltage of four-level NNPC inverter.

Level		S_{1a}	S_{2a}	S_{3a}	S_{4a}	S_{5a}	S_{6a}	V_{Ca1}	V_{Ca2}	V_{an}
3		1	1	1	0	0	0	—	—	$V_{DC}/2$
2	2A	1	0	1	1	0	0	$C(i_a > 0)$ $D(i_a < 0)$	—	$V_{DC}/6$
	2B	0	1	1	0	0	1	$D(i_a > 0)$ $C(i_a < 0)$	$D(i_a > 0)$ $C(i_a < 0)$	
1	1A	1	0	0	1	1	0	$C(i_a > 0)$ $D(i_a < 0)$	$C(i_a > 0)$ $D(i_a < 0)$	$-V_{DC}/6$
	1B	0	0	1	1	0	1	—	$D(i_a > 0)$ $C(i_a < 0)$	
0		0	0	0	1	1	1	—	—	$-V_{DC}/2$

C: charging; D: discharging.

or FC inverter. Take phase A for example, there are six operation states of a phase, as shown in Table 1.

When the switch turns on, it corresponds to the state “1” in Table 1, while when the switch turns off, it corresponds to the state “0.” The four levels of phase voltage are labeled as 3, 2, 1, and 0, which correspond to the topology of $V_{DC}/2$, $V_{DC}/6$, $-V_{DC}/6$, and $-V_{DC}/2$. Different from the conventional four-level NPC inverter, there are two kinds of redundant states on “1” and “2” levels of NNPC topology. “1” level corresponds to 1A and 1B, while “2” level corresponds to the 2A and 2B in Table 1. It should be noted that the flying capacitor is used in the NNPC inverter. So the capacitor voltage balancing should be considered. The impact of switching states on the capacitor voltage is shown in Table 1.

As shown in Figure 2, only the flying capacitor C_{a1} is charged or discharged during the state “2A,” remaining the flying capacitor C_{a2} unaffected, while both the flying capacitors C_{a1} and C_{a2} will be charged or discharged during the state “2B.” It is worth noting that if the current direction is different, the capacitor charging or discharging is also different. Take the state “2A” for example, when the current $i_a > 0$, the capacitor C_{a1} is charged, and while the current $i_a < 0$, the

capacitor C_{a1} discharged. The details regarding the capacitor voltage balancing will be presented in the following section.

3. Common Mode Voltage of Four-Level NNPC Inverter

The common mode voltage is one of the important issues for power converters [20]. The common mode voltage of the NNPC inverter can be expressed as (1), where v_{cm} is the common voltage, and v_{an} , v_{bn} , and v_{cn} represent the three-phase voltages, respectively.

$$v_{cm} = \frac{v_{an} + v_{bn} + v_{cn}}{3}. \quad (1)$$

There are 4 switching states in each phase. So there are 64 switching states for NNPC inverter. The relationship between the common mode voltage and switching state is shown in Table 2. Taking “000” in Table 2 for example, it is indicated that the a phase output is 0 level, the b phase output is 0 level, and the c phase output is 0 level.

From Table 2, it can be observed that there are 10 kinds of values, including $\pm V_{DC}/2$, $\pm 7V_{DC}/18$, $\pm 5V_{DC}/18$, $\pm V_{DC}/6$,

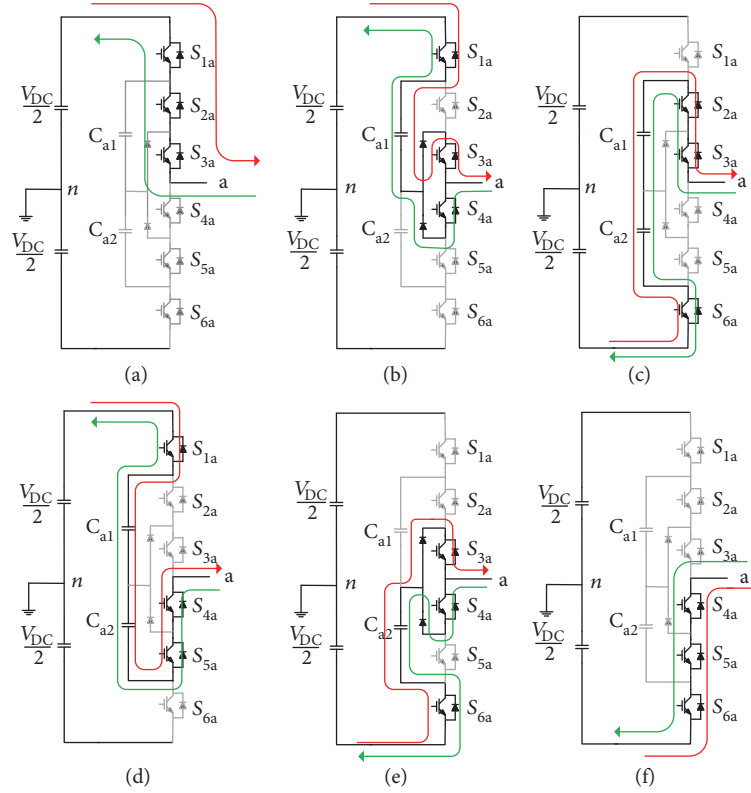


FIGURE 2: Six switching states of NNPC inverter: (a) switching state 3; (b) switching state 2A; (c) switching state 2B; (d) switching state 1A; (e) switching state 1B; and (f) switching state 0.

TABLE 2: Switching states and common mode voltage of four-level NNPC inverter.

Common mode voltage	Switch states
$-V_{DC}/2$	000
$-7 V_{DC}/18$	001, 010, 100
$-5 V_{DC}/18$	002, 011, 020, 101, 110, 200
$-V_{DC}/6$	003, 021, 012, 030, 102, 111, 120, 201, 210, 300
$-V_{DC}/18$	013, 022, 031, 103, 112, 121, 130, 202, 211, 220, 301, 310
$V_{DC}/18$	023, 032, 113, 122, 131, 203, 212, 221, 230, 302, 311, 320
$V_{DC}/6$	033, 123, 132, 213, 222, 231, 303, 312, 321, 330
$5 V_{DC}/18$	133, 223, 232, 313, 322, 331,
$7 V_{DC}/18$	233, 323, 332
$V_{DC}/2$	333

and $\pm V_{DC}/18$ regarding the common mode voltage of the NNPC inverter. Obviously, the common mode voltage would be very high if all switching states are involved. In order to reduce the common mode voltage, two groups of switching states can be utilized. In this way, the common mode voltage can be reduced to 1/18 of the DC bus voltage. The space vector diagram is as shown in Figure 3.

4. Proposed Modulation Strategy

As discussed above, the common mode voltage can be significantly reduced to $\pm V_{DC}/18$ by selecting the specified vectors and switching states. In order to achieve the objective, a new modulation strategy is proposed in this paper. Firstly, the desired level arrangement is generated by the modulation strategy. Secondly, select the redundant state to balance the flying capacitor voltage.

As shown in Figure 3, the vectors of the selected 24 switching states are similar to those of three-level vectors. If the outermost four-level vectors (e.g., 130 and 230) are not considered, the other four-level vectors are associated with the three-level vectors. Taking the sector of A1 as an example, the three-level vector of 000 in Figure 3(a) (redundant vectors 111 and 222) corresponds to the virtual vector (red cross presents the virtual vector) in Figure 3(b), while the three-level vector of 211 (redundant vectors 100) corresponds to the four-level vector of 211. Other relationship can also be derived, as shown in Table 3.

For the virtual vector, it can be achieved by vector synthesis. Taking the virtual vector of sector A1 for example, it can be synthesized through (1) vectors 221 and 310, (2) vectors 220 and 311, and (3) vectors 320 and 211. The vector synthesis diagram is shown in Figure 4.

Based on the above analysis, a novel modulation method is proposed in this paper. Firstly, comparing two triangle waves with sine wave, the three-level vectors can be

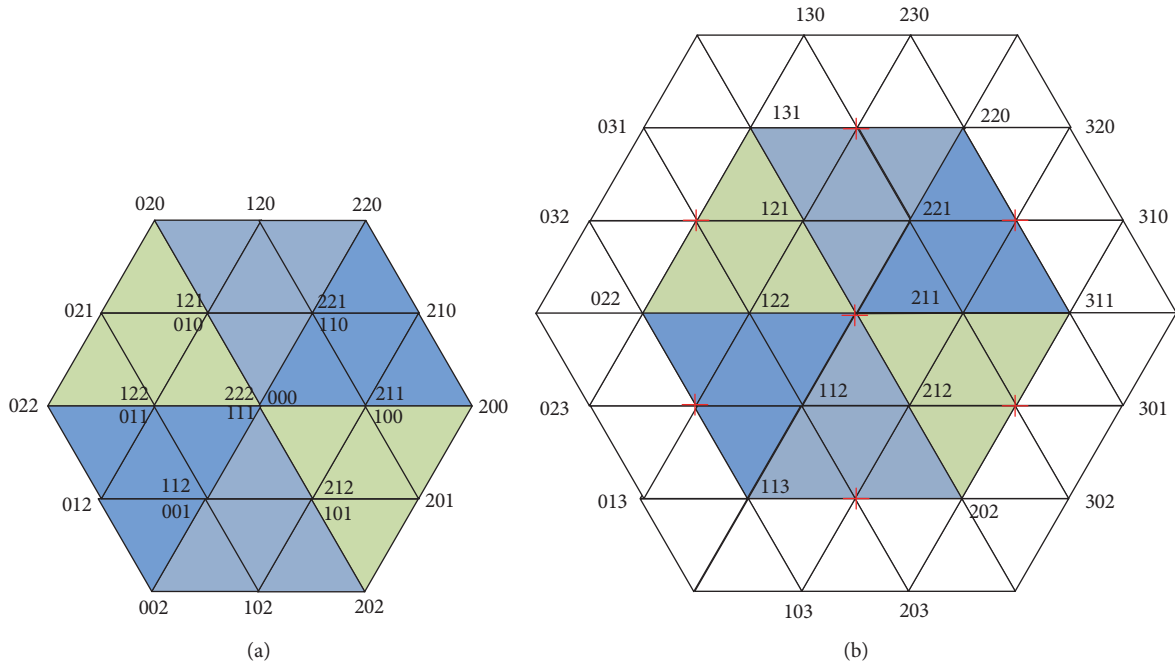


FIGURE 3: Space vector diagram (a) three-level inverter and (b) four-level inverter $v_{cm} = \pm V_{DC}/18$.

TABLE 3: Relationship between three-level inverter voltage vector and four-level inverter voltage vector.

Three-level vector	Four-level vector
211, 100	211
200	311
210	Virtual vector
221, 110	221
220	220
120	Virtual vector
121, 010	121
020	131
021	Virtual vector
122, 011	122
022	022
012	Virtual vector
112, 001	112
002	113
102	Virtual vector
212, 101	212
201	Virtual vector
202	202
000, 111, 222	Virtual vector

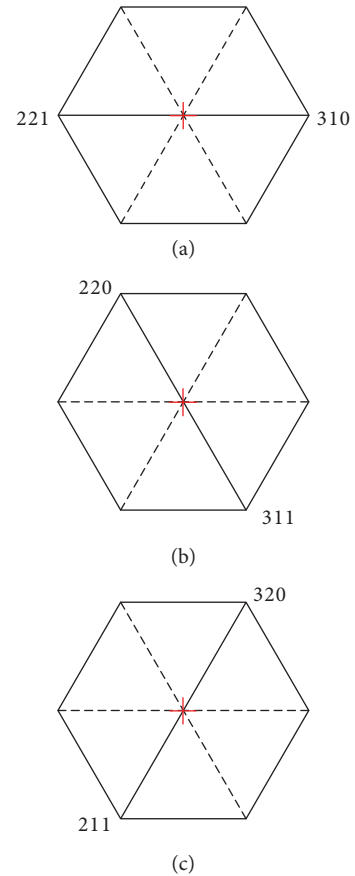


FIGURE 4: Virtual vector synthesis diagram.

generated, as shown in Table 3. With the logical transformation, these vectors can be linked to the four-level vectors. The synthesis method is shown in Table 4.

For the selection of the carrier modulation, the in-phase disposition (IPD) modulation is used due to the following advantages.

TABLE 4: Relationship between virtual and synthesis vectors.

Virtual vector	Synthetic vector
210	Sector A1 ∩ B1 221 and 310
210	Sector A1 ∩ B2 211 and 320
120	Sector A2 ∩ B2 121 and 230
120	Sector A2 ∩ B3 221 and 130
021	Sector A3 ∩ B3 122 and 031
021	Sector A3 ∩ B4 121 and 032
012	Sector A4 ∩ B4 112 and 023
012	Sector A4 ∩ B5 122 and 013
102	Sector A5 ∩ B5 212 and 103
102	Sector A5 ∩ B6 112 and 203
201	Sector A6 ∩ B6 211 and 302
201	Sector A6 ∩ B1 212 and 301

- (1) In IPD modulation, voltage vector complies with the “near three vector principle,” that is, there no longer exists jumping of the two levels on the corresponding four-level vector.
- (2) In the A1 sector, for example, in a switching period of IPD modulation, the vector 210 (i.e., three-level vector corresponding to the four-level virtual vector) has the same effect time in the first half and the second half switching periods. Therefore, it is easy to realize the vector synthesis in Table 4 (in the first $T_s/2$ with a synthetic vector, after $T_s/2$ with another synthetic vector).

As discussed above, the desired level can be generated by means of carrier modulation and logical transformation. Note that there are redundant states about “1” or “2” level (see Table 1) of the NNPC inverter. The capacitor voltage balance can be achieved with the redundant states. Taking one phase as an example, the variation of the flying capacitor voltage is defined as (2), where V_{ci} is the flying capacitor voltage, $i = 1, 2$. The capacitor voltage can be balanced if ΔV_{ci} is close to 0.

$$\Delta V_{ci} = V_{ci} - \frac{V_{DC}}{3} \quad (2)$$

The capacitor voltage balancing mechanism is shown in Table 5. The balance of the capacitor C_1 can be achieved only by selecting the redundancy state of “2” level, while the balance of the capacitor C_2 can be achieved by selecting the redundancy state of “1” level.

The control block diagram is shown in Figure 5. In this way, the output four-level voltage can be achieved. Meanwhile the common mode voltage can be significantly reduced to $\pm V_{DC}/18$. Aside from that, the capacitor voltage balancing can be achieved.

5. Simulation Results

In order to verify the effectiveness of the proposed solution, the time-domain simulations are carried out in MATLAB/

TABLE 5: Mechanism of capacitor voltage balancing.

Level	ΔV_{Ci}	Phase current i_a	Redundancy state
2	$\Delta V_{C1} < 0$	< 0	2B
		≥ 0	2A
	$\Delta V_{C1} \geq 0$	< 0	2A
		≥ 0	2B
1	$\Delta V_{C2} < 0$	< 0	1B
		≥ 0	1A
	$\Delta V_{C2} \geq 0$	< 0	1A
		≥ 0	1B

Simulink. The type of simulation model we use is a real circuit with power switches, instead of a transfer function or mathematical description model. The simulation parameters are listed in Table 6.

The simulation results are shown as follows. From Figures 6 and 7, it can be observed that the flying capacitor voltages can be well balanced around 2200 V ($V_{DC}/3$), and the ripple is less than 7.5% of the rated voltage. The output phase voltage is four-level waveform, while the line voltage is seven-level waveform. On the other hand, the common mode voltage of the conventional solution is as high as $\pm 5V_{DC}/18$, while the common mode voltage of the proposed solution is significantly reduced to $\pm V_{DC}/18$.

In order to verify the dynamic performance of the proposed solution, the simulations are carried out with a step change from half to full loads at 0.1 s. As shown in Figure 8, it can be seen that the current increases from half to full loads, and the waveform quality of current is kept well all the time. Note that the fluctuation of capacitor voltage after heavy loading increases, but it is still less than 7.5% of the rated voltage. So the system has a good dynamic performance. At the same time, the common mode voltage, before and after the load step, remains around $\pm V_{DC}/18$.

In order to further verify the effectiveness of the capacitor voltage balancing scheme, the balancing control is enabled, then disabled, and finally enabled, as shown in Figure 9.

From Figure 9, it can be observed that when the balancing control is disabled, the capacitor voltage tends to diverge. Meanwhile, the common mode voltage is negatively impacted with higher amplitude; that is, the capacitor voltage balancing has an impact on common mode voltage. After the balancing control is recovered at $t = 0.1\text{ s}$, common mode voltage and capacitor voltage can be quickly restored to normal operation state, which verifies the effectiveness of the proposed solution.

6. Conclusion

This paper has presented the modeling and analysis of a novel four-level NNPC inverter for PV power plant applications. It is concluded that the proposed solution can significantly reduce the common mode voltage to $V_{DC}/18$. Also, it can

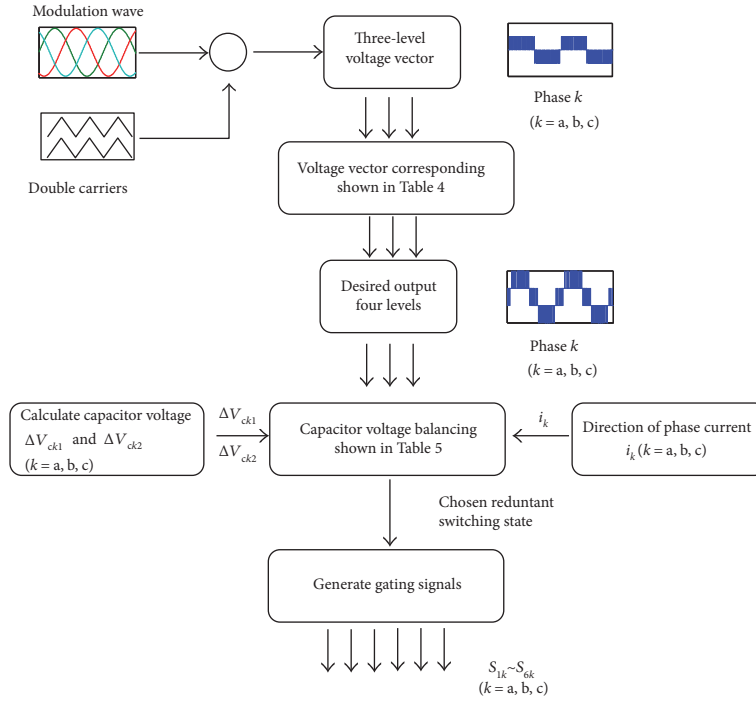


FIGURE 5: The controller diagram of the four-level NNPC inverter.

TABLE 6: Simulation parameters.

Parameters	Value
DC voltage	6.6 kV
Output frequency	60 Hz
Output inductor	5 mH
Output resistor	7.5 Ω
Flying capacitor	2200 μF
Modulation index	0.95

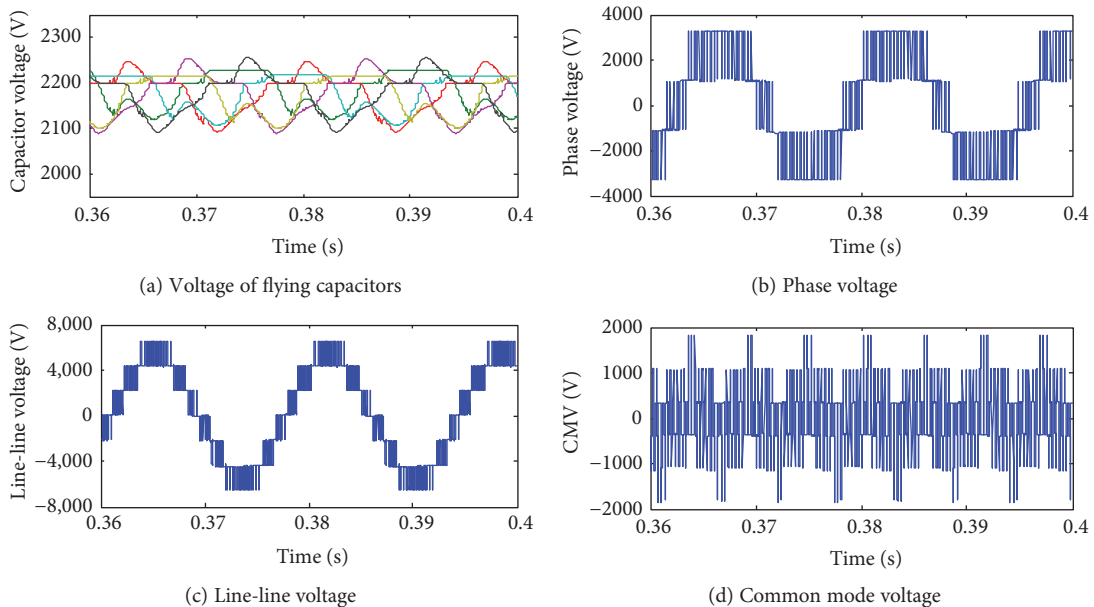


FIGURE 6: Simulation results (conventional solution).

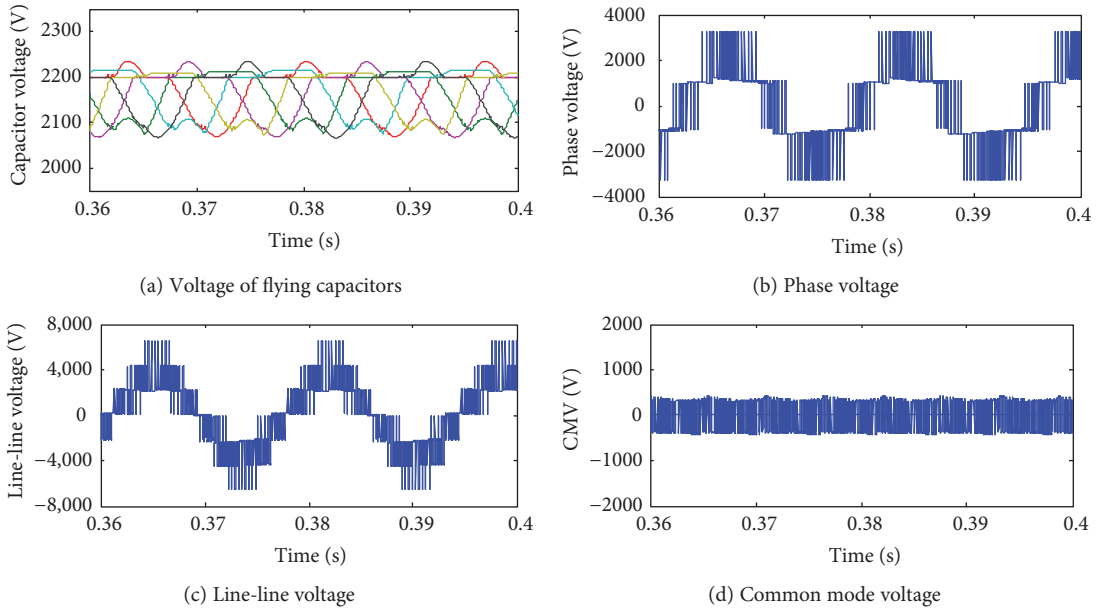


FIGURE 7: Simulation results (proposed solution).

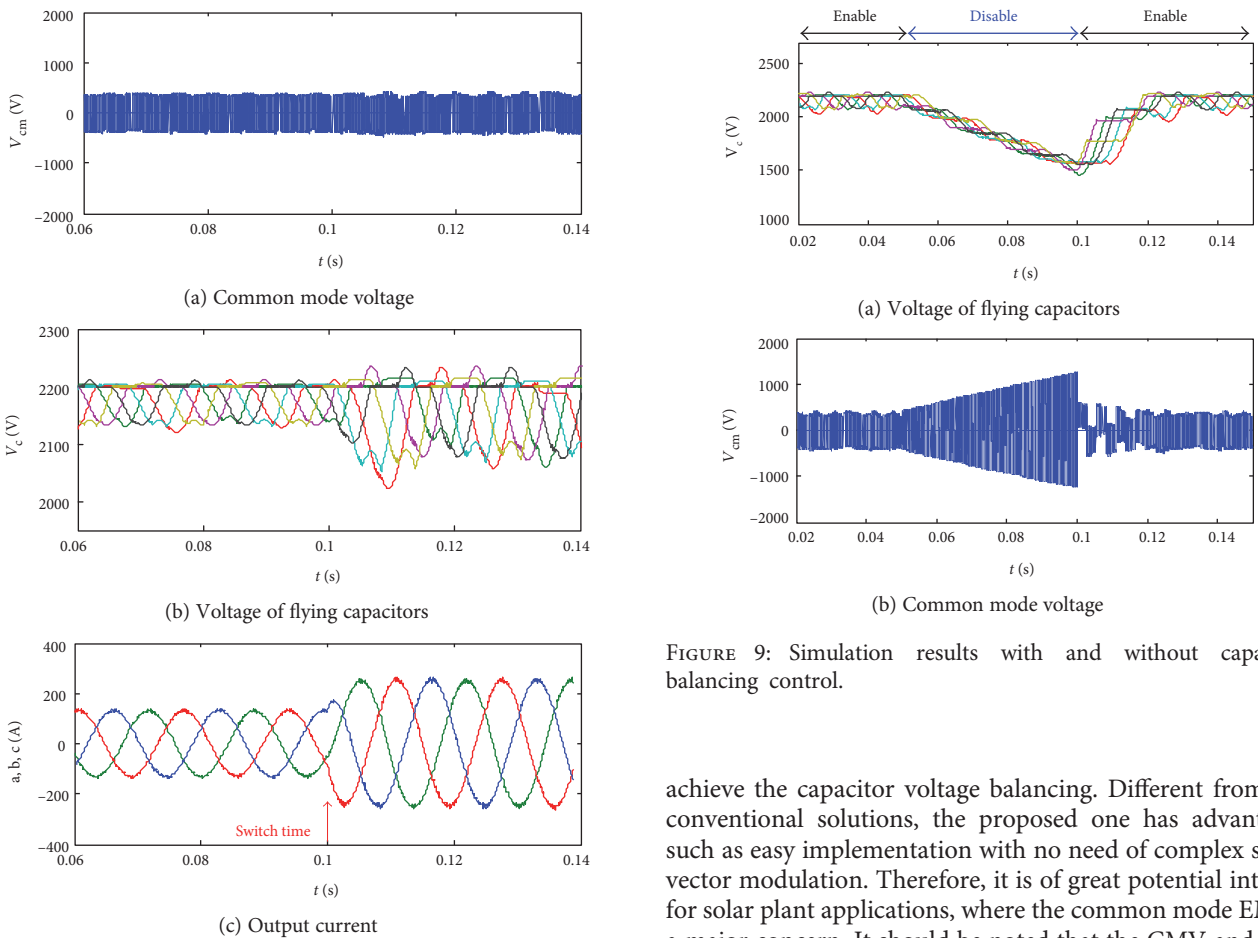


FIGURE 8: Simulation results from half to full load.

FIGURE 9: Simulation results with and without capacitor balancing control.

achieve the capacitor voltage balancing. Different from the conventional solutions, the proposed one has advantages such as easy implementation with no need of complex space vector modulation. Therefore, it is of great potential interest for solar plant applications, where the common mode EMI is a major concern. It should be noted that the CMV and EMI reductions of the four-level NNPC inverter are focused for PV power plant. Other issues such as grid synchronization, control, and protection [21–26] are beyond the scope of the paper.

Conflicts of Interest

The authors declare that there is no conflict of interests regarding publication of this paper.

Acknowledgments

This work was supported by the Science Foundation for Hundred Excellent Innovation Talents Support Program of Hebei Province (SLRC2017059) and Science Foundation for Returned Scholars of Hebei Province (CL201622).

References

- [1] J. Hu, L. Sun, X. Yuan, S. Wang, and Y. Chi, "Modeling of type 3 wind turbine with df/dt inertia control for system frequency response study," *IEEE Transactions on Power Systems*, 2016.
- [2] J. Hu, S. Wang, W. Tang, and X. Xiong, "Full-capacity wind turbine with inertial support by optimizing phase-locked loop," *IET Renewable Power Generation*, vol. 11, no. 1, pp. 44–53, 2017.
- [3] D. Zhang, Y. Wang, J. Hu, S. Ma, Q. He, and Q. Guo, "Impacts of PLL on the DFIG-based WTG's electromechanical response under transient conditions: analysis and modeling," *CSEE Journal of Power and Energy Systems*, vol. 2, no. 2, pp. 30–39, 2016.
- [4] X. Guo, "A novel CH5 inverter for single-phase transformerless photovoltaic system applications," *IEEE Transactions on Circuits and Systems II: Express Briefs*, 2017.
- [5] W. Li, G. Yunjie, H. Luo, W. Cui, X. He, and C. Xia, "Topology review and derivation methodology of single-phase transformerless photovoltaic inverters for leakage current suppression," *IEEE Transactions on Industrial Electronics*, vol. 62, no. 7, pp. 4537–4551, 2015.
- [6] X. Guo, "Three phase CH7 inverter with a new space vector modulation to reduce leakage current for transformerless photovoltaic systems," *IEEE Journal of Emerging and Selected Topics in Power Electronics*, vol. 5, no. 2, pp. 708–712, 2017.
- [7] S. Kouro, M. Malinowski, K. Gopakumar et al., "Recent advances and industrial applications of multilevel converters," *IEEE Transactions on Industrial Electronics*, vol. 57, no. 8, pp. 2553–2579, 2010.
- [8] H. Nademi, A. Das, R. Burgos, and L. E. Norum, "A new circuit performance of modular multilevel inverter suitable for photovoltaic conversion plants," *IEEE Journal of Emerging and Selected Topics in Power Electronics*, vol. 4, no. 2, pp. 393–404, 2016.
- [9] S. Essakiappan, H. Krishnamoorthy, P. Enjeti, R. S. Balog, and S. Ahmed, "Multilevel medium-frequency link inverter for utility scale photovoltaic integration," *IEEE Transactions on Power Electronics*, vol. 30, no. 7, pp. 3674–3684, 2015.
- [10] M. Hamzeh, A. Ghazanfari, H. Mokhtari, and H. Karimi, "Integrating hybrid power source into an islanded MV microgrid using CHB multilevel inverter under unbalanced and nonlinear load conditions," *IEEE Transactions on Energy Conversion*, vol. 28, no. 3, pp. 643–651, 2013.
- [11] L. Liu, H. Li, Y. Xue, and W. Liu, "Decoupled active and reactive power control for large-scale grid-connected photovoltaic systems using cascaded modular multi-level converters," *IEEE Transactions on Power Electronics*, vol. 30, no. 1, pp. 176–187, 2015.
- [12] R. Araneo, S. Lammens, M. Grossi, and S. Bertone, "EMC issues in high power grid-connected photovoltaic plants," *IEEE Transactions on Electromagnetic Compatibility*, vol. 51, no. 3, pp. 639–648, 2009.
- [13] X. Guo, B. We, T. Zhu et al., "Leakage current suppression of three phase flying capacitor PV inverter with new carrier modulation and logic function," *IEEE Transactions on Power Electronics*, 2017.
- [14] X. Guo, R. He, J. Jian, Z. Lu, X. Sun, and Z. Lu, "Leakage current elimination of four-leg inverter for transformerless three-phase PV systems," *IEEE Transactions on Power Electronics*, vol. 31, no. 3, pp. 1841–1846, 2016.
- [15] X. Guo and X. Jia, "Hardware-based cascaded topology and modulation strategy with leakage current reduction for transformerless PV systems," *IEEE Transactions on Industrial Electronics*, vol. 62, no. 12, pp. 7823–7832, 2016.
- [16] C. Hu, X. Yu, D. Holmes et al., "An improved virtual space vector modulation scheme for three-level active neutral-point-clamped inverter," *IEEE Transactions on Power Electronics*, vol. 32, no. 10, pp. 7419–7434, 2017.
- [17] Z. Shao, X. Zhang, F. Wang, R. Cao, and H. Ni, "Analysis and control of neutral-point voltage for transformerless three-level PV inverter in LVRT operation," *IEEE Transactions on Power Electronics*, vol. 32, no. 3, pp. 2347–2359, 2017.
- [18] H. Geng, S. Li, C. Zhang, G. Yang, and L. Dong, "Hybrid communication topology and protocol for distributed-controlled cascaded H-bridge multilevel STATCOM," *IEEE Transactions on Industry Application*, vol. 53, no. 1, pp. 576–584, 2017.
- [19] M. Narimani, B. Wu, Z. Cheng, and N. Zargari, "A new nested neutral point clamped (NNPC) converter for medium-voltage (MV) power conversion," *IEEE Transactions on Power Electronics*, vol. 29, no. 12, pp. 6375–6382, 2014.
- [20] X. Guo, D. Xu, and B. Wu, "Common-mode voltage mitigation for back-to-back current-source converter with optimal space-vector modulation," *IEEE Transactions on Power Electronics*, vol. 31, no. 1, pp. 688–697, 2016.
- [21] X. Guo, W. Wu, and Z. Chen, "Multiple-complex coefficient-filter-based phase-locked loop and synchronization technique for three-phase grid interfaced converters in distributed utility networks," *IEEE Transactions on Industrial Electronics*, vol. 58, no. 4, pp. 1194–1204, 2011.
- [22] Z. Shuai, Y. Hu, Y. Peng, T. Chunming, and Z. J. Shen, "Dynamic stability analysis of synchronverter-dominated microgrid based on bifurcation theory," *IEEE Transactions on Industrial Electronics*, 2017.
- [23] Z. Shuai, W. Huang, C. Shen, G. Jun, and Z. John Shen, "Characteristics and restraining method of fast transient inrush fault currents in synchronverters," *IEEE Transactions on Industrial Electronics*, 2017.
- [24] X. Guo, W. Liu, and Z. Lu, "Flexible power regulation and current-limited control of grid-connected inverter under unbalanced grid voltage faults," *IEEE Transactions on Industrial Electronics*, 2017.
- [25] X. Guo, W. Liu, X. Zhang, X. Sun, Z. Lu, and J. M. Guerrero, "Flexible control strategy for grid-connected inverter under unbalanced grid faults without PLL," *IEEE Transactions on Power Electronics*, vol. 30, no. 4, pp. 1773–1778, 2015.
- [26] L. Chen and S. Mei, "An integrated control and protection system for photovoltaic microgrids," *CSEE Journal of Power and Energy Systems*, vol. 1, no. 1, pp. 36–42, 2015.

Research Article

Modulation above Pump Beam Energy in Photorefectance

D. Fuertes Marrón

Instituto de Energía Solar, ETSIT, Universidad Politécnica de Madrid, Avda. Complutense 30, 28040 Madrid, Spain

Correspondence should be addressed to D. Fuertes Marrón; dfuertes@ies.upm.es

Received 19 May 2017; Accepted 27 June 2017; Published 9 July 2017

Academic Editor: Christin David

Copyright © 2017 D. Fuertes Marrón. This is an open access article distributed under the Creative Commons Attribution License, which permits unrestricted use, distribution, and reproduction in any medium, provided the original work is properly cited.

Photorefectance is used for the characterisation of semiconductor samples, usually by sweeping the monochromatized probe beam within the energy range comprised between the highest value set up by the pump beam and the lowest absorption threshold of the sample. There is, however, no fundamental upper limit for the probe beam other than the limited spectral content of the source and the responsivity of the detector. As long as the modulation mechanism behind photorefectance does affect the complete electronic structure of the material under study, sweeping the probe beam towards higher energies from that of the pump source is equally effective in order to probe high-energy critical points. This fact, up to now largely overseen, is shown experimentally in this work. E_1 and $E_0 + \Delta_0$ critical points of bulk GaAs are unambiguously resolved using pump light of lower energy. This type of *upstream* modulation may widen further applications of the technique.

1. Introduction

Photorefectance (PR) is a pump and probe spectroscopy well known in the characterisation of semiconductor materials and devices [1, 2]. It relies on the diffusion of charge carriers photogenerated with the pump beam and the subsequent screening of electric fields already present in the sample at space-charge regions, typically located at interfaces and free surfaces. The dielectric constant of the specimen and thus its reflectance R are slightly perturbed upon the field modulation. Such small changes in reflectance, ΔR , are detected using phase-sensitive techniques with a probe light beam swept in wavelength and typically expressed as relative $\Delta R/R$ ratios. The technique contributed significantly to the present understanding of the electronic structure of most typical semiconductors [3] and has found continuity as a valuable characterisation tool of novel materials, like dilute nitrides [4], low-dimensional structures [5, 6], and their potential applications [7]. The detection stage in PR largely relies on the rejection of any pump light scattered upon interaction with the sample that may eventually end up at the detector. Scattered pump light is typically the main source of background noise, together with sample luminescence, in the resulting spectra [8], as it enters right at the chopping frequency tracked by phase-sensitive detection. The use of

long-pass filters (LPF) right in front of the detector is commonplace in order to avoid such spurious scattering. PR proceeds thereof by sweeping the monochromatized probe beam toward lower energies from the uppermost value set by the filter edge, recording changes in reflectance of the probe upon the action of the pump beam. Implicitly, the highest energy accessible to the experiment is therefore set by the optical edge of the LPF, normally chosen a few hundreds of meV below the nominal photon energy of the pump source. This small offset accounts for both the line broadening of the source (particularly if LEDs are used) as well as the finite width of the filter optical edge.

In contrast to this sort of standard PR, the so called “first derivative” modulation spectroscopies [9], like piezoreflectance (PzR) or thermoreflectance (TR), do not appear bounded at high energies as a result of the perturbing action. In the case of piezoreflectance [10], stress-strain cycles are imposed on the sample, usually by means of a piezoelectric actuator attached to the sample, whereas in thermoreflectance [11], the sample is subjected to thermal cycles induced, for example, by a Peltier element. The same applies to electroreflectance (ER), making use of an externally applied modulated electric field on the sample [12]. Even when each modulation mechanism is executed at a reference frequency thereby used for detection, the detection itself is in principle

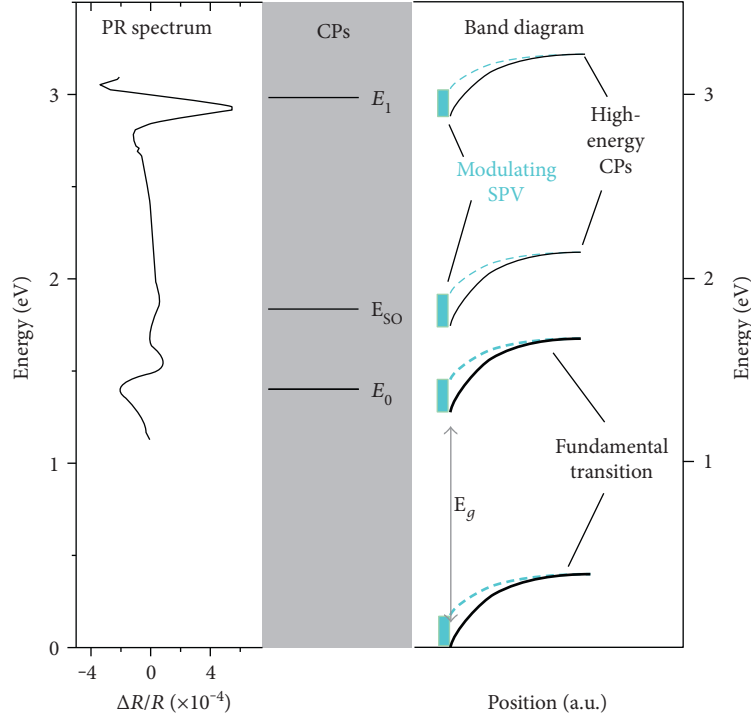


FIGURE 1: Schematic representation of critical points (CPs) E_0 , $E_0 + \Delta_0$ (indicated as E_{SO}), and E_1 of GaAs represented in ascending energy on the same energy axis of a typical experimental PR spectrum (left). The band diagram picture (right) illustrates the modulation mechanism at CPs, namely, periodic SPV generation, upon illumination with a chopped pump beam of energy slightly above E_g , inducing transitions at the fundamental gap. Notice that, although the $E_0 + \Delta_0$ transition involves a valence state below the valence band edge (reference at zero energy), the corresponding energy is greater than the fundamental gap E_g .

not constrained to a certain photon energy range of the probe beam. The only practical limitations are imposed by the spectral content of the source and the responsivity of the detector employed. The reason is that the perturbation used as modulation agent, independently of its origin, does affect the entire electronic structure of the sample under test. PR is not different from PzR, TR, or ER in that respect. The generation of photovoltage upon pump illumination of a semiconductor, on which PR is based, is better illustrated as a change in band bending at those regions in the sample sustaining space charge (SCR), typically free surfaces or interfaces, as schematically shown in Figure 1. Even when photogeneration of free carriers upon appropriate illumination may just involve the first interband transitions allowed between occupied and empty states, the entire electronic structure of the material is thereby affected, as long as the modulation of the electric field associated to the SCR is active. It is thus expected that electronic transitions at energies higher than those directly accessible with the pump beam be equally subject to the modulating action and consequently not PR-silent, as schematically shown in Figure 1. In other words, *upstream* modulation using probe photon energies higher than that of the pump beam should be equally accessible as in *downstream* PR using LPF, should the photon energy of the pump beam be sufficient in order to develop a measurable photovoltage. The latter can actually happen at the fundamental absorption edge of the sample or via defect states at subband-gap energies. In what follows, we show evidence of the

modulation of high-energy critical points showing up in PR spectra of GaAs when using pump light of lower energy.

2. Methods

For this purpose, we have used a Si-doped GaAs wafer (AXT, $n = 1 \times 10^{18} \text{ cm}^{-3}$). The reason is that *n*-type-doped GaAs exhibits intense and broad signatures in PR at room temperature, particularly in the range of E_1 transitions, that are typically better resolved than in intrinsic material. PR was measured using the light beam of a quartz-tungsten-halogen lamp (operated at 150 W) as probe of intensity $I_0(\lambda)$. The light is passed through a monochromator (1/8 m Cornerstone-Newport) and focused with optical lenses on the sample. Light directly reflected with intensity $I_0(\lambda)R(\lambda)$ is focused on a solid-state Si-detector. The current signal is transformed into a dc-voltage and preamplified (Keithley). The pump beam from a laser source is mechanically chopped at 777 Hz and superimposed onto the light spot of the probe on the sample, providing the periodic modulation. Three laser sources have been used as pump in the experiments, the 325 nm line of a 15 mW He-Cd laser, the line at 632.8 nm of a 30 mW He-Ne laser, and a solid-state laser diode operating at 814 nm. The signal recorded at the detector contains therefore two components: the dc average signal $I_0(\lambda)R(\lambda)$ and the ac modulated contribution $I_0(\lambda)\Delta R(\lambda)$, where $\Delta R(\lambda)$ is the modified reflectance resulting from the modulated perturbation. The complete signal feeds a lock-

in amplifier (Stanford Instruments), which tracks the ac signal at the chopping frequency. The relative change in reflectance is obtained thereof by normalizing the ac signal with respect to the dc component, with typical values in the range of 10^{-3} to 10^{-6} .

3. Results

Figure 2 shows recorded spectra as a function of wavelength between 400 and 1100 nm under different pump beams and pass filters. Long-pass filters (LPF) and short-pass filters (SPF) are indicated in the figure together with the nominal edge. The upper panel shows three measurements performed under 325 nm pump and different filter combinations: (i) LPF 395 nm, (ii) LPF 395 nm and LPF 665 nm, and (iii) LPF 395 nm and SPF 600 nm. LPF 395 nm prevents scattered laser light entering in the detector. Additional LPF 665 nm and SPF 600 nm further restrict the accessible wavelength range towards higher or lower wavelengths from their nominal edge, respectively. Three PR signatures are readily observed in the figure, corresponding to E_0 , $E_0 + \Delta_0$, and E_1 transitions, as shown previously in Figure 1. Such interband transitions are well documented: E_0 corresponds to the lowest direct gap at the Γ point of the Brillouin zone between Γ_8 valence- and Γ_6 -conduction-band states; $E_0 + \Delta_0$ corresponds to the split-off valence band Γ_7 due to spin-orbit coupling, connecting to the same Γ_6 -conduction-band state; finally, E_1 is the next critical point in order of ascending energy and takes place along the Λ direction from the center of the Brillouin zone [13]. The filter edges can be identified in the spectra with the declining signals deviating from the LPF 395 nm spectrum. Perfect overlapping over the respective wavelength ranges with the measurement using just LPF 395 is observed, confirming the absence of eventual second-order harmonics in the spectra.

The medium panel shows spectra obtained under 632.8 nm pump illumination. The short wavelength spectrum was obtained with SPF 600 nm, whereas the long wavelength one was obtained with LPF 665 nm. The nominal wavelength of the laser is indicated by the dotted line. As it can be observed, the spectra collected under 632.8 nm pump keep track of E_0 and E_1 signatures ($E_0 + \Delta_0$ is affected by the filter edges), very much like the 325 nm pump does, even when E_1 is not directly accessible now under 632.8 nm illumination. Instead, upstream modulation of high-energy critical points results from absorption involving lower energy transitions E_0 and $E_0 + \Delta_0$. The modified built-in potential and the associated field, due to photogenerated carrier screening at SCR, is the modulating mechanism affecting the entire electronic structure, including all high-energy critical points. They can be probed thereof in a similar fashion as low-energy critical points in downstream modulation. Finally, the lower panel of Figure 2 shows a PR spectrum obtained under 814 nm pump illumination using SPF 800 nm. The dotted line indicates the wavelength of the pump beam. Again, high-energy critical points E_1 and E_{SO} are readily probed when pumped with light of lower energy.

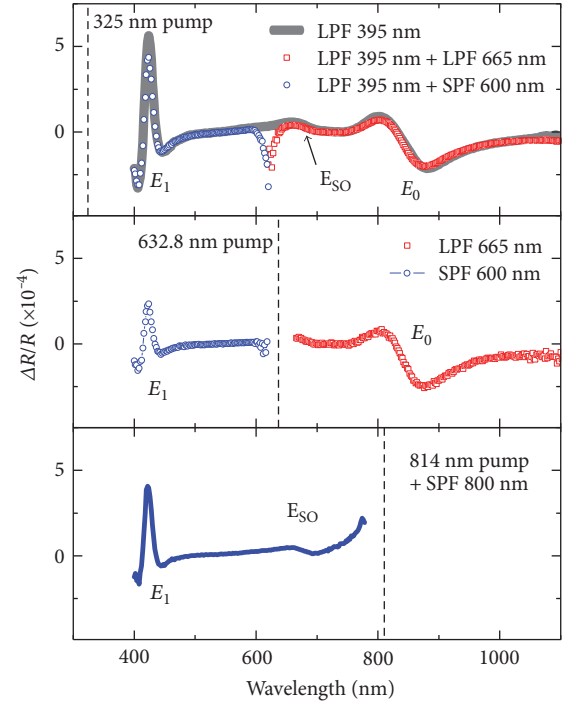


FIGURE 2: PR spectra of *n*-GaAs wafer obtained under different pump beam energies and pass filters. Dotted lines indicate the nominal wavelength of the pump beams. Critical points E_0 , $E_0 + \Delta_0$ (labeled as E_{SO}), and E_1 are also indicated. (Upper panel) using 325 nm pump with LPF 395 nm and additional LPF 665 nm or SPF 600 nm. (Middle panel) using 632.8 nm pump with LPF 665 nm or SPF 600 nm. (Lower panel) using 814 nm pump and SPF 800 nm.

4. Discussion

Upstream photoreflectance is better understood when considering the character of modulation spectroscopies as absorption-based techniques. As such, and contrarily to the case of luminescence, PR also probes unoccupied states which are accessible to the energy range of the photons in the probe beam. However, it is not necessary that the pump generating the periodic perturbation be absorbed in a process involving that particular transition to be probed in the experiment. This result has been recently reported in GaSb [14] and previously in subbandgap PR on GaAs [15]. The latter case illustrates the fact that upstream modulation can also be activated via optically active defect states in the bandgap. As a matter of fact, the upstream energy range in PR has largely been overseen in the past, as evidenced by the absence of related literature, with just a few exceptions mentioned. Even in such cases, results have oftentimes been presented in relation to certain specificities of the samples, rather than as an expected output.

5. Conclusion

In summary, it has been shown that the information range accessible to PR can be extended to energies above that of the pump beam. Its practical implementation is simple, either replacing LPF with SPF or alternatively using notch or narrow-band filters around the wavelength of the pump

beam. Probing upstream is a direct consequence of the absorption-based nature of the technique and the intrinsic modulation mechanism involved, based on photovoltage generation upon the action of the pump beam affecting the entire electronic structure of the material under test. Accounting for this fact, apparently not much explored yet, may widen the current applicability of the technique.

Conflicts of Interest

The author declares that there is no conflict of interest regarding the publication of this paper.

Acknowledgments

This work has been carried out within the COST-action MP1406-Multiscale in Modelling and Validation for Solar Photovoltaics, supported by the European Commission. Financial support from the Ministry of Economy and Competitiveness (TEC2015-64189-C3-1-R) and from the Comunidad de Madrid (S2013/MAE-2780) is acknowledged.

References

- [1] M. Cardona, *Modulation Spectroscopy*, Academic Press, New York and London, 1969.
- [2] F. H. Pollak, "Study of semiconductor surfaces and interfaces using electromodulation," *Surface and Interface Analysis*, vol. 31, p. 938, 2001.
- [3] D. E. Aspnes, *Handbook on Semiconductors Vol. 2*, T. S. Moss, Ed., North-Holland Publishing Co., Amsterdam, 1980.
- [4] W. Walukiewicz, W. Shan, K. M. Yu et al., "Interaction of localized electronic states with the conduction band: band anticrossing in II-VI semiconductor ternaries," *Physical Review Letters*, vol. 85, p. 1552, 2000.
- [5] O. J. Glembocki, B. V. Shanabrook, N. Bottka, W. T. Beard, and J. Comas, "Photoreflectance characterization of interband transitions in GaAs/AlGaAs multiple quantum wells and modulation-doped heterojunctions," *Applied Physics Letters*, vol. 46, p. 970, 1985.
- [6] J. Misiewicz, P. Sitarek, G. Sek, and R. Kudrawiec, "Semiconductor heterostructures and device structures investigated by photoreflectance spectroscopy," *Materials Science*, vol. 21, p. 263, 2003.
- [7] D. Fuertes Marrón, E. Cánovas, I. Artacho et al., "Application of photoreflectance to advanced multilayer structures for photovoltaics," *Materials Science and Engineering B*, vol. 178, p. 599, 2013.
- [8] F. H. Pollak, *Handbook on Semiconductors Vol. 2*, T. S. Moss, Ed., Elsevier, Amsterdam, 1994.
- [9] D. E. Aspnes, "Third-derivative modulation spectroscopy with low-field electroreflectance," *Surface Science*, vol. 37, p. 418, 1973.
- [10] W. E. Engeler, H. Fritzsche, M. Garfinkel, and J. J. Tiemann, "High-sensitivity piezoreflectivity," *Physical Review Letters*, vol. 14, p. 1069, 1965.
- [11] B. Batz, "Reflectance modulation at a Germanium surface," *Solid State Communications*, vol. 4, p. 241, 1966.
- [12] B. O. Seraphin and R. B. Hess, "Franz-Keldysh effect above the fundamental edge in Germanium," *Physical Review Letters*, vol. 14, p. 138, 1965.
- [13] P. Lautenschlager, M. Garriga, S. Logothetidis, and M. Cardona, "Interband critical points of GaAs and their temperature dependence," *Physical Review B*, vol. 35, p. 9174, 1987.
- [14] H. J. Jo, M. G. So, J. S. Kim, and S. J. Lee, "Optical properties of GaSb measured using photoluminescence and photoreflectance spectroscopy," *Journal of the Korean Physical Society*, vol. 69, p. 826, 2016.
- [15] H. Bhimnathwala and J. M. Borrego, "Surface characterization of LEC Si-GaAs using photoreflectance with sub-bandgap excitation," *Solid-State Electronics*, vol. 35, p. 1503, 1992.